Fermilab

FERMILAB-THESIS-1997-57

MEASUREMENT OF THE PROTON-ANTIPROTON TOTAL CROSS SECTION AT CENTER OF MASS ENERGY OF 1800 GEV

A Dissertation

Presented to the Graduate School

of Cornell University

in Partial Fulfillment of the Requirements for the Degree of

Doctor of Philosophy

by

Carlos Avila

May 1997

MEASUREMENT OF
THE PROTON-ANTIPROTON TOTAL CROSS SECTION
AT CENTER OF MASS ENERGY OF 1800 GEV

Carlos Avila, Ph.D.

Cornell University 1997

We have made a new measurement of the $P\overline{P}$ total cross section at $\sqrt{s}$=1800 GeV, using a luminosity independent method for the analysis. The value obtained is $\sigma_T = 69.82 \pm 2.44$ mb. Also we obtained the values of $\sigma_{el} = 14.93 \pm 1.03$ mb and $\sigma_{in} = 54.88 \pm 1.43$ mb for the total elastic and total inelastic cross sections respectively. To perform our measurement we used scintillation counters to detect inelastic events, and 4 scintillating fiber detectors installed inside the Tevatron vacuum to detect elastic events; the elastic detectors were read out with image intensifiers and ccds.

BIOGRAPHICAL SKETCH

The author was born in Ibague, Colombia to Emilio and Graciela Avila on August 8, 1965. He attended La universidad de Los Andes in Bogota, Colombia where he obtained a Bachelor degree in Electrical Engineering in March of 1988. He joined the E710 Collaboration at Fermilab in July of 1988 where he worked on his Physics Bachelor thesis under the guidance of Roy Rubinstein and Shekhar Shukla ("Measurement of the Nuclear Slope Parameter for Proton-Antiproton at CMS energy = 1800 GeV", Phys. Lett. B 234 (1990) 158.). He obtained the Bachelor degree in Physics from Universidad de Los Andes in Bogota, Colombia in February 1989. He worked with the E710 collaboration until July of 1990 where he also participated in the analysis of the Proton-Antiproton total cross section at CMS energy=1800 GeV (Phys. Rev. Lett. 63 (1989) 2784. and Phys. Lett. B 243 (1990) 158.) and the analysis of ρ, the ratio of the real to the imaginary part of the forward scattering amplitude for proton-antiproton interactions at CMS energy = 1800 GeV (Phys. Rev. Lett. 68 (1992) 2433.). In August of 1990 he went to the University of Massachusetts at Amherst to pursue his graduate studies in Physics, he obtained the degree of Master of Science in May 1992. At the university of Massachussets he was a Research Assistant working with Professors Michael Kreisler and Edward Hartouni on Experiment E690 at Fermilab. In August 1992 he went to Cornell university to pursue his PhD degree. He joined the E811

Collaboration at Fermilab in May of 1993. Under the guidance of professor Jay Orear he participated in the research and development of the Scintillating fiber detector (Nucl. Instr. Meth. A 360 (1995) 80.) and on the analysis of the E811 measurement of the Proton-Antiproton total cross section at CMS energy=1800 GeV for his doctoral dissertation.

To my parents

To my brother and sisters

To the memory of my brother Jairo

ACKNOWLEDGEMENTS

I express my gratitude to everyone who participated at the different stages of experiment E811. The combined efforts of all of us made possible the successful completion of the experiment.

Ricardo De Salvo, Cinthia DaVia, Rosy Mondardini and Mark Lundin, were the CERN collaboration on E811 in its early stage. They contributed with the design and testing of the prototype of the scintillating fiber detector. Working during a short period of time at CERN with Rosy, Ricardo and Mark gave me the chance to learn the details and tests they had performed with the prototype detector. I really appreciate their hospitality and their patience teaching me about their work.

I worked very closely at Fermilab with Dave Eartly, Frank Turkot, Hans Jostlein and Win Baker to get the final detector configuration fully tested and working. I feel fortunate to have the chance to work with each of them because all the discussions about tests, debugging problems and ideas of how to implement things, taught me different ways of approaching a problem and solving it.
I want to thank Hans and Win because they were very supportive throughout my stay at Fermilab.

Jay Orear, the spokesman of the E811 experiment and my advisor, I appreciate his concern about my training as a student and all his support throughout my stay at Cornell. So many discussions we had about every aspect of the experiment were very useful to keep making progress continuously.

Roy Rubinstein was involved in the fast Logic of the experiment and in the data analysis, he was my advisor at Fermilab during the analysis. I want to thank him for the important role he has played in my education. He gave me the chance to get my first exposure to High Energy Physics at Fermilab before deciding to go to graduate school. Both Roy and Jay were my main support during the data analysis, all their ideas and explanations and their patience correcting the drafts of this document are very much appreciated.

Cedric Guss was in charge of the Data Acquisition and involved in the early stage of the data analysis. I thank him for all the many hours he put in on his commitment.

I also thank Shekhar Shukla for being accessible for consulting about many details of the analysis.

The support giving by the Physics, Computing , Accelerator and Research Departments at Fermilab was very crucial for getting the experiment running. The Physics Department contributed with technical support for the detector development, position controls, alignment, mapping, final installation etc. There are many names to mention. I thank Sten Hansen and Richard Bingham who were in charge

of the readout of the position sensors of the elastic detectors. I thank Greg Sellberg who always offered his help and his tools when needed; he was involved in the mapping of the scintillating fibers. I thank Ken Gray and Jack Upton who provided technical help during preparation of different pieces of the system and later on during installation in the Tevatron. I also thank all the techs from the electrical and electronics group of the Physics Department who were always willing to help with a quick response. I thank Jorge Montes from Lab D who was involved with the measurements needed for the alignment of the detectors.

The Computing Division contributed in the development of the data acquisition. In particular I thank the involvement of Margherita Vittone and Ruth Pordes.

The Accelerator Division contributed with the vacuum installation, detector position controls and by achieving the beam conditions we needed for taking our data. Stan Pruss was our accelerator expert and in charge of the heavy beam scraping which allowed us to get our detectors very close to the beam. Craig McClure was in charge of the remote control system to move the detectors from the accelerator control room. Norman Gelfand provided to us the lattice parameters for our interaction point. I thank the vacuum techs and the main control room operators for their fast response to our requests.

The Research Division provided to us the video data acquisition system (VDAS). I want to thank specifically Al Bambaugh and Kelly Knickerbocker for building and testing the VDAS systems for us and later on for their availability when problems were present.

Thanks to all the other physicists, technicians and engineers that were involved and I am not mentioning here.

The support giving by my family was really essential. They were my main incentive to pursue my education. I thank my little sister Albita for being my main moral support; the internet helped us to keep in touch on a daily basis.

There are many other names to mention who were relevant during my life as a graduate student: Mike Kreisler and Ed Hartouni, my former advisors from University of Massachusetts. Rasheed Joshi and Dave Coletta my classmates and close friends. Monica Bertani, Michela Spagnoli, Ivano Veronesi, Stefano Zuchelli, Giorgio Giacomelli, Norman Amos, Sasan Sadr, Dimitrios Dimitroyannis who were collaborators in the E710 experiment who helped me during my first visit to Fermilab. I thank my very close friends, classmates and co-workers, Juan Carlos Sanabria and Luis Montes. I want to say thanks to all the many other friends I don't mention here who helped me at work or in my personal life.

Finally I want to acknowledge the support given to me by Karl Berkelman director of the Laboratory of Nuclear Studies and the office of the Vice-President of Research at Cornell University.

This research project was carried out thanks to the support given by the U.S. Department of Energy, a grant from the U.S. National Science Foundation, the INFN Eloisatron project, the LAA group at CERN and Fermi National Accelerator Laboratory.

TABLE OF CONTENTS

LIST OF FIGURES

LIST OF TABLES

CHAPTER 1

Introduction

1.1 Kinematic Variables

$P\overline{P}$ elastic scattering ($P\overline{P} \rightarrow P\overline{P}$) is described in terms of the Mandelstam variables (Lorentz invariant kinematic variables). If p_{Pin} and $p_{\overline{P}in}$ are the incident 4-momenta and p_{Pout} and $p_{\overline{P}out}$ are the final 4-momenta, the Mandelstam variables are defined as

$$s = (p_{Pin} + p_{\overline{P}in})^2 = (p_{Pout} + p_{\overline{P}out})^2 \quad (1.1)$$

$$t = (p_{Pin} - p_{Pout})^2 = (p_{\overline{P}in} - p_{\overline{P}out})^2 \quad (1.2)$$

$$u = (p_{Pin} - p_{\overline{P}out})^2 = (p_{\overline{P}in} - p_{Pout})^2 \quad (1.3)$$

Where s is the CMS energy squared and t is the four-momentum transferred squared. If we define p as the momentum in the CMS system, θ the scattering angle in the CMS system, m_p the mass of the proton and E the energy in the laboratory system ($E^2 = p_{lab}^2 + m_p^2$) we can write s,t and u as follows

$$s = 4(p^2 + m_p^2) = 2m_p(m_p + E) \quad (1.4)$$

$$t = -2p^2(1 - cos(\theta)) \quad (1.5)$$

$$u = -2p^2(1 + cos(\theta)) \quad (1.6)$$

$$s + t + u = 4m_p^2 \tag{1.7}$$

Since we are interested in very high energies and very small scattering angles, we can make the following approximations:

$$s \approx 4p^2 \tag{1.8}$$

$$t \approx -p^2\theta^2 \tag{1.9}$$

1.2 The Differential Elastic Cross Section

If we denote with f the scattering amplitude in the CMS system, the differential cross section will be:

$$\frac{d\sigma}{dt} = \frac{\pi}{p^2}\frac{d\sigma}{d\Omega_{CMS}} = \frac{\pi}{p^2}|f|^2 \tag{1.10}$$

The scattering amplitude for proton-antiproton elastic scattering is composed of two parts:

- The electromagnetic or coulomb amplitude (f_c).
- The hadronic or nuclear amplitude (f_n)

The coulomb amplitude is obtained from the Rutherford formula:

$$f_c = \pm\frac{2p\alpha G^2(t)}{4\pi|t|} \tag{1.11}$$

where "+" sign is for $P\overline{P}$ interactions and "-" sign is for PP interactions. α is the fine structure constant ($\alpha \approx \frac{1.0}{137.037}$). G(t) is the proton electromagnetic form factor; generally approximated as

$$G(t) = \left(1 + \frac{|t|}{0.71}\right)^{-2} \tag{1.12}$$

From experimental observations it has been established that for values of $|t| < 0.1$ $(GeV/c)^2$ the nuclear scattering amplitude can be parametrized as

$$f_n = \frac{p\sigma_T(\rho + i)\exp(\frac{-B|t|}{2})}{4\pi} \tag{1.13}$$

The total cross section is related to the imaginary part of the nuclear scattering amplitude through the optical theorem:

$$\sigma_T = \frac{4\pi}{p}\Im m\left\{f_n(t=0)\right\} \tag{1.14}$$

ρ is the ratio of the real to the imaginary part of the nuclear scattering amplitude at $|t|$=0 :

$$\rho = \left.\frac{\Re e\left(f_n(t)\right)}{\Im m\left(f_n(t)\right)}\right|_{t=0} \tag{1.15}$$

B is the nuclear slope parameter. The differential cross section for $P\overline{P}$ and PP interactions can be written as

$$\frac{d\sigma}{dt} = \frac{\pi}{p^2}\left|f_n + f_c e^{\pm i\alpha\phi(t)}\right|^2 \tag{1.16}$$

$\alpha\phi(t)$ is the difference in phase between coulomb and nuclear scattering amplitudes. $\phi(t)$ can be written as (see reference [27]) :

$$\phi(t) = ln\left(\frac{0.08}{|t|}\right) - 0.577 \tag{1.17}$$

Another calculation of $\phi(t)$ can be found in reference [28], however for small values of $|t|$ that calculation agrees with the one given in equation 1.17. Substituting equations 1.11 and 1.13 into 1.16 (here we have written $\hbar$ and c explicitly)

$$\frac{d\sigma}{dt} = \frac{4\pi(\hbar c)^2\alpha^2 G^4(t)}{|t|^2} \pm \frac{\alpha(\rho \mp \alpha\phi)\sigma_T G^2(t)}{|t|}\exp(\frac{-B|t|}{2}) + \frac{(1+\rho^2)\sigma_T^2}{16\pi(\hbar c)^2}\exp(-B|t|) \tag{1.18}$$

where "+" is for $P\overline{P}$ interactions and "-" is for PP interactions. Equation 1.18 contains three parameters: σ_T, B and ρ which are the fundamental parameters of high energy elastic scattering. A plot of $\frac{d\sigma}{dt}$ is shown in Figure 1.1, where the values of B=17.0 $(GeV/c)^{-2}$, σ_T = 75 mb and ρ=0.15 were used. The value of $|t|$ where the region of maximal nuclear-coulomb interference occurs corresponds to the one where $f_c = f_n$ $(G(t)^2 \approx 1.0)$:

$$|t|_{interf} \approx \frac{8\pi\alpha}{\sigma_T} \approx \frac{0.0714}{\sigma_T} \tag{1.19}$$

At very low values of $|t|$ $(|t| \ll |t|_{interf})$ coulomb scattering dominates and at very large values of $|t|$ $(|t| \gg |t|_{interf})$ $P\overline{P}$ interactions are produced mainly by nuclear scattering.

For Tevatron energies ($\sqrt{s}$ = 1800 GeV) the maximum nuclear-coulomb interference occurs at $|t|_{interf} \approx 0.00095$ (taking σ_T = 75 mb) which corresponds to scattering angles of $\theta_{interf} \approx 34$ μ rad.

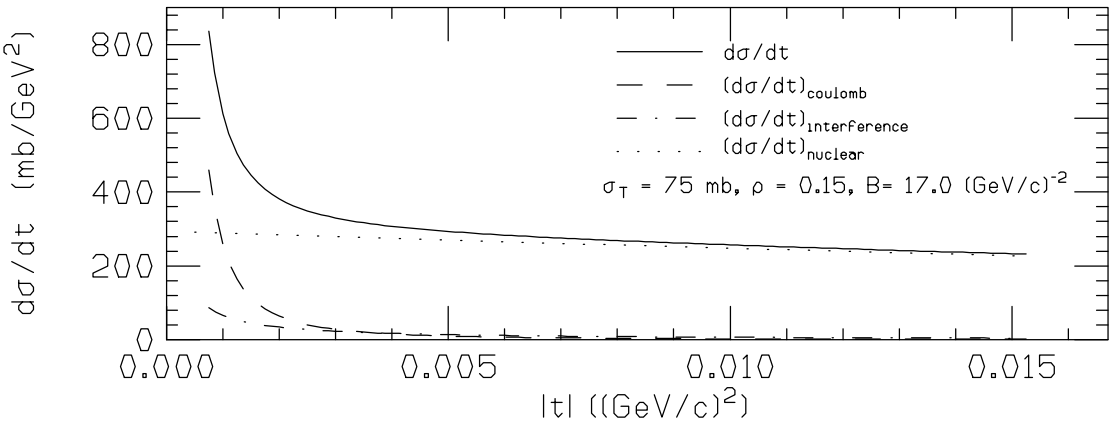

Figure 1.1: Plot of $\frac{d\sigma}{dt}$ for $P\overline{P}$ elastic scattering as defined in equation 1.18, using the values of B=17.0 $(GeV/c)^{-2}$, σ_T = 75 mb and ρ=0.15.

1.3 The Total Cross Section

The processes that contribute to the total cross section for $P\overline{P}$ interactions can be categorized as follows:

$$\sigma_T = \sigma_{el} + \sigma_{in} = \sigma_{el} + \sigma_{sd_P} + \sigma_{sd_{\overline{P}}} + \sigma_{dd} + \sigma_{nd} \tag{1.20}$$

The diffraction dissociation events correspond to excitation of the diffracted particle into high mass states that just after their creation decay into other particles. The nondiffractive events correspond to a central collision where particles are produced at all angles.

- σ_{el} is the forward elastic cross section.
- σ_{sd_P} is the single diffractive cross section when the incoming proton fragments :

$$P + \overline{P} \rightarrow \overline{P} + X \tag{1.21}$$

- $\sigma_{sd_{\overline{P}}}$ is the single diffractive cross section when the incoming antiproton fragments :

$$P + \overline{P} \rightarrow P + X \tag{1.22}$$

- σ_{dd} is the double diffractive cross section. Both proton and antiproton fragment:

$$P + \overline{P} \rightarrow X_1 + X_2 \tag{1.23}$$

- σ_{nd} is the nondiffractive part of the inelastic cross section.

The forward elastic cross section is obtained by integrating over t the differential cross section due to nuclear scattering:

$$\sigma_{el} = \int_0^\infty \left(\frac{d\sigma_n}{dt} \right) dt \tag{1.24}$$

$\frac{d\sigma_n}{dt}$ is the third term of equation 1.18:

$$\sigma_{el} = \frac{1}{B}\frac{(1+\rho^2)\sigma_T^2}{16\pi(\hbar c)^2} \tag{1.25}$$

Experimental observation shows that single diffractive and double diffractive events produce low multiplicity events with particles produced in the very forward and very backward region in the CMS system. The non-diffractive events correspond to the major contribution to the inelastic cross section and secondaries for these events are produced at all angles and with higher multiplicity. The differential cross section for single diffractive dissociation is usually parametrized as

$$\frac{d\sigma}{dtdM_X^2} = A\frac{e^{-b|t|}}{(M_X^2)^{\alpha}} \tag{1.26}$$

where M_X is the mass for the system X. The total single diffractive cross section is obtained by integrating Equation 1.26 over t and M_X.

The differential cross section for double diffractive dissociation can be written as

$$\frac{d\sigma_{DD}^2}{dM_1^2 dM_2^2} = \frac{k}{\sigma_{el}}\frac{d\sigma_1}{dM_1^2}\frac{d\sigma_2}{dM_2^2} \tag{1.27}$$

where $k = \frac{r^2}{2r-1}$ and $r = \frac{b_{sd}}{B_{el}}$.

1.4 Asymptotic Theorems

There is not, as yet, a fundamental theory that can explain the experimental observations on elastic scattering and total cross sections. The data are interpreted in terms of different phenomenological models.

Some theorems which describe the behavior of the $P\overline{P}$ and PP scattering in the limit $s \to \infty$ have been derived based on the properties of analyticity, unitarity and crossing of the scattering amplitudes. Here we just summarize them. Proofs

for the theorems can be found in more specialized articles (see for example [29], [35], [37]).

1.4.1 Froissart Bound

The Froissart bound ([31]) is an upper limit for the total cross section when $s \to \infty$:

$$\sigma_T \leq \frac{\pi}{m_\pi^2}\left(ln\left(\frac{s}{s_0}\right)\right)^2 \approx (60mb)\left(ln\left(\frac{s}{s_0}\right)\right)^2 \tag{1.28}$$

where m_π is the mass of the pion and s_0 is an unknown scale factor.

1.4.2 The Pomeranchuk Theorem

The Pomeranchuk theorem ([32]) was important before any experiment took data at $\sqrt{s}$ energies higher than 20 GeV. At that time it was believed that the cross section was going to become constant with energy. That theorem states that if one of the cross sections (the PP and $P\overline{P}$) becomes constant as $s \to \infty$ and if ρ grows less rapidly than $ln(s)$, then the difference of the two total cross sections goes to 0 as $s \to \infty$. However there is no indication as yet that the two cross sections are leveling off, therefore this theorem is not applicable.

1.4.3 The Eden-Kinoshita Theorem

The Eden-Kinoshita theorem ([33]) is a modification of the Pomeranchuk theorem. It states that if one of the cross sections grows as $\left(ln(\frac{s}{s_0})\right)^\gamma$ then the difference $\Delta\sigma = \left[\sigma(P\overline{P}) - \sigma(PP)\right]$ cannot grow faster than $\left(ln(\frac{s}{s_0})\right)^{\frac{\gamma}{2}}$ and therefore $\frac{\sigma_T(P\overline{P})}{\sigma_T(PP)} \to 1$ when $s \to \infty$.

1.4.4 The Cornille-Martin Theorem

This theorem is an extension of the Pomeranchuk theorem to the differential elastic cross sections. It states that ([34]) :

$$\frac{\frac{d\sigma}{dt}(P\overline{P})}{\frac{d\sigma}{dt}(PP)} \rightarrow 1 \text{ when } s \rightarrow \infty \tag{1.29}$$

This relation holds even though the difference of the cross sections may not go to 0. One consequence of this theorem is that

$$\frac{B(P\overline{P})}{B(PP)} \rightarrow \text{ 1 if s} \rightarrow \infty \tag{1.30}$$

There is a corollary about the ratio of ρ values ([35]) :

$$\left(\frac{\rho(P\overline{P})}{\rho(PP)}\right)^2 \rightarrow \text{ 1 as s} \rightarrow \infty \tag{1.31}$$

1.4.5 Other Theorems

From dispersion relations it can be shown that at very high energies there is a relation between ρ and σ_T (see [30]):

$$\rho(s) \approx \frac{\pi}{2\sigma_T}\frac{d\sigma_T}{dln(s)} \tag{1.32}$$

There is also a theorem about the difference of the total cross sections that says that if above some energy the signs of the real and imaginary parts of the scattering amplitude remain the same, then the difference in the PP and $P\overline{P}$ cross sections vanishes asymptotically (see [39]).

1.5 Experimental Observations

There is not a theory, as yet, of strong interactions that can be used to explain PP or $P\overline{P}$ elastic scattering. We summarize here the experimental work done up to date to understand PP and $P\overline{P}$ elastic scattering at high energies.

1.5.1 Nuclear Slope Parameter - B

According to the experiments performed before 1971 B($P\overline{P}$) was larger than B(PP). The value of B(PP) was seen to increase with $\sqrt{s}$, while the value of B($P\overline{P}$) was increasing slower with energy than B(PP). The data obtained at $\sqrt{s}$ = 5 GeV and $\sqrt{s}$=62 GeV showed that B(PP) is increasing from 9.5 $(GeV/c)^{-2}$ to 13.0 $(GeV/c)^{-2}$, the same data showed that B($P\overline{P}$) was increasing at a slower rate than B(PP).

The most recent experiments (E710 [14], and CDF [9]) have found that B($P\overline{P}$) continues increasing by about 4.0 $(GeV/c)^{-2}$ from $\sqrt{s}$=53 GeV to $\sqrt{s}$=1800 GeV.

Figure 1.2 shows the existent data for B(PP) and B($P\overline{P}$), where it is noted that B(PP) and B($P\overline{P}$) seem to be converging to the same value at high energies, satisfying the corollaries proposed by Block and Cahn (reference [35]) as a consequence of the Cornille-Martin theorem.

1.5.2 The Differential Cross Section

Figure 1.3 corresponds to the $P\overline{P}$ data taken by UA4 experiment ([17]) at $\sqrt{s}$=546 GeV. Figure 1.4 shows data from UA4 and E710 experiments ([16], [10]). Two important features are observed:

1. Two slope parameters are fit within different ranges of $|t|$. The value of slope measured using the range $0.02 < |t| < 0.15$ differs in about ΔB=1.6 $(GeV/c)^{-2}$ with respect to the value in the range $0.15 < |t| < 0.3$. Then, if we want to include the full range of $|t|$ $(0.02 < |t| < 0.3)$ and measure only one slope we cannot use just the function $e^{-B|t|}$, a better χ^2 can be gotten using a function $e^{-B|t|+C|t|^2}$. The value of C is known as the curvature

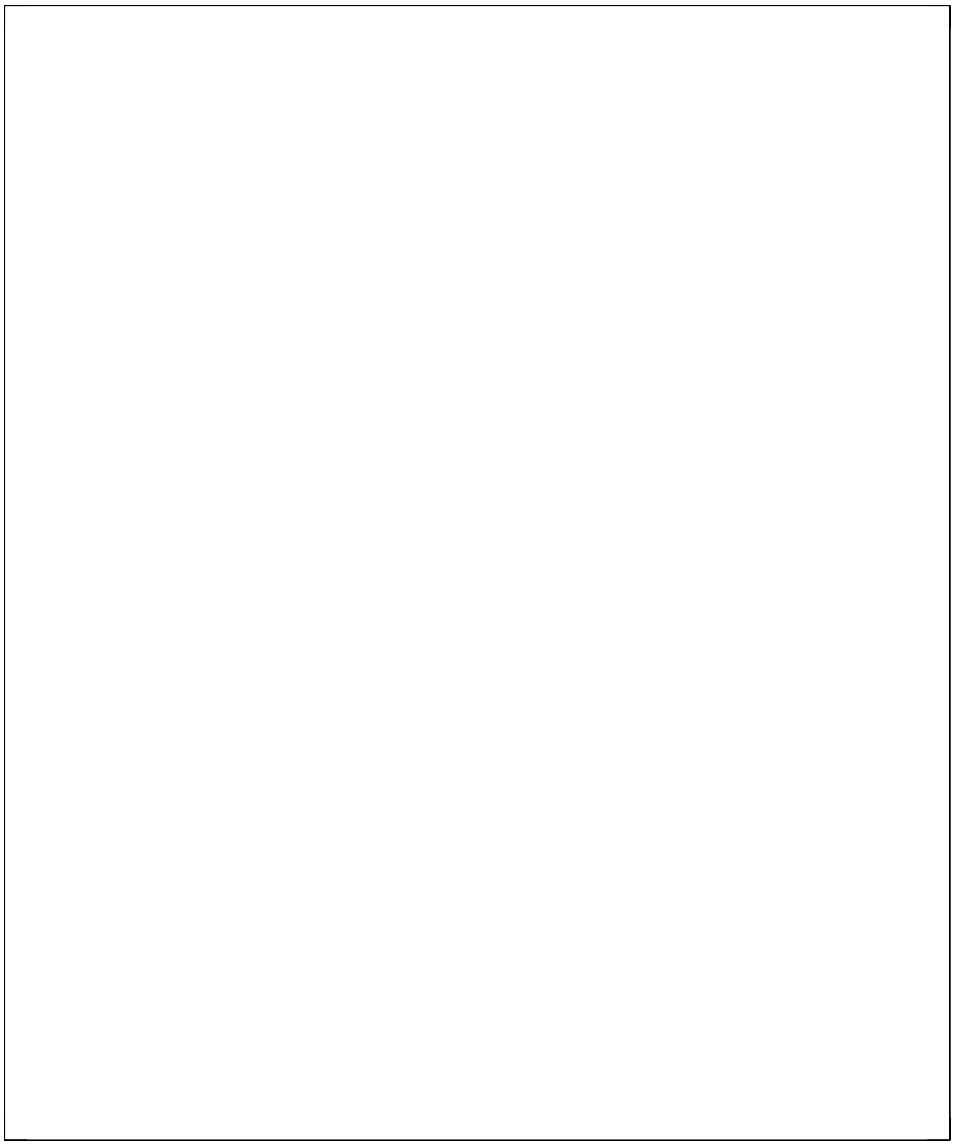

Figure 1.2: Comparison B(PP) and B($P\overline{P}$) at different energies. The upper curve is $P\overline{P}$ data and the lower curve is PP data.

parameter or in other words, we may say that the slope parameter is not a constant in t but rather a function that depends on t and the energy. The same behavior was observed at lower energies by fixed target experiments (ref [19]) and at the ISR (ref. [18]) and if we fit C to that data we find a positive value. For higher energies it is expected that C parameter becomes negative since it is expected that the differential cross section will approach the pattern of diffraction of light. Data from E710 experiment is consistent with a curvature parameter equals to 0 (ref [10]).

2. There is a minimum (a dip) in $\frac{d\sigma}{dt}$ distribution. It has been observed that this minimum tends to be located at lower values of $|t|$ and loose depth when the energy is increased. For $P\overline{P}$ at $\sqrt{s}$=23 GeV the dip was observed to be located at $|t|$=1.45 $(GeV/c)^2$, at $\sqrt{s}$= 53 GeV it is at $|t|$= 1.25 $(GeV/c)^2$, at $\sqrt{s}$ = 546 GeV it happens at $|t|$=0.8 $(GeV/c)^2$. At $\sqrt{s}$ =1800 GeV the E710 data is consisted with an expected dip at $|t|$=0.6 (see figure 1.4b)).

1.5.3 The Total Cross Section

The first experiments that measured the total cross section observed that $\sigma_T(P\overline{P})$ was bigger than $\sigma_T(PP)$, but it was decreasing for higher values of $\sqrt{s}$ and approaching the value of $\sigma_T(PP)$. Due to these experimental observations it was assumed that the total cross sections $\sigma_T(PP)$ and $\sigma_T(P\overline{P})$ would be identical at high energies and that they would be close to a constant value of 40 mb. The data taken in the early 1970's at the CERN ISR ([11]) in the energy range 10 $< \sqrt{s} \leq$ 62 GeV found that the PP cross section was not constant but instead it was rising with energy from about 40 mb at at $\sqrt{s}$=5 GeV to 43.5 mb at $\sqrt{s}$=62 GeV. Measurements of the $\sigma_T(P\overline{P})$ showed that $\sigma_T(P\overline{P})$ was decreasing from 50

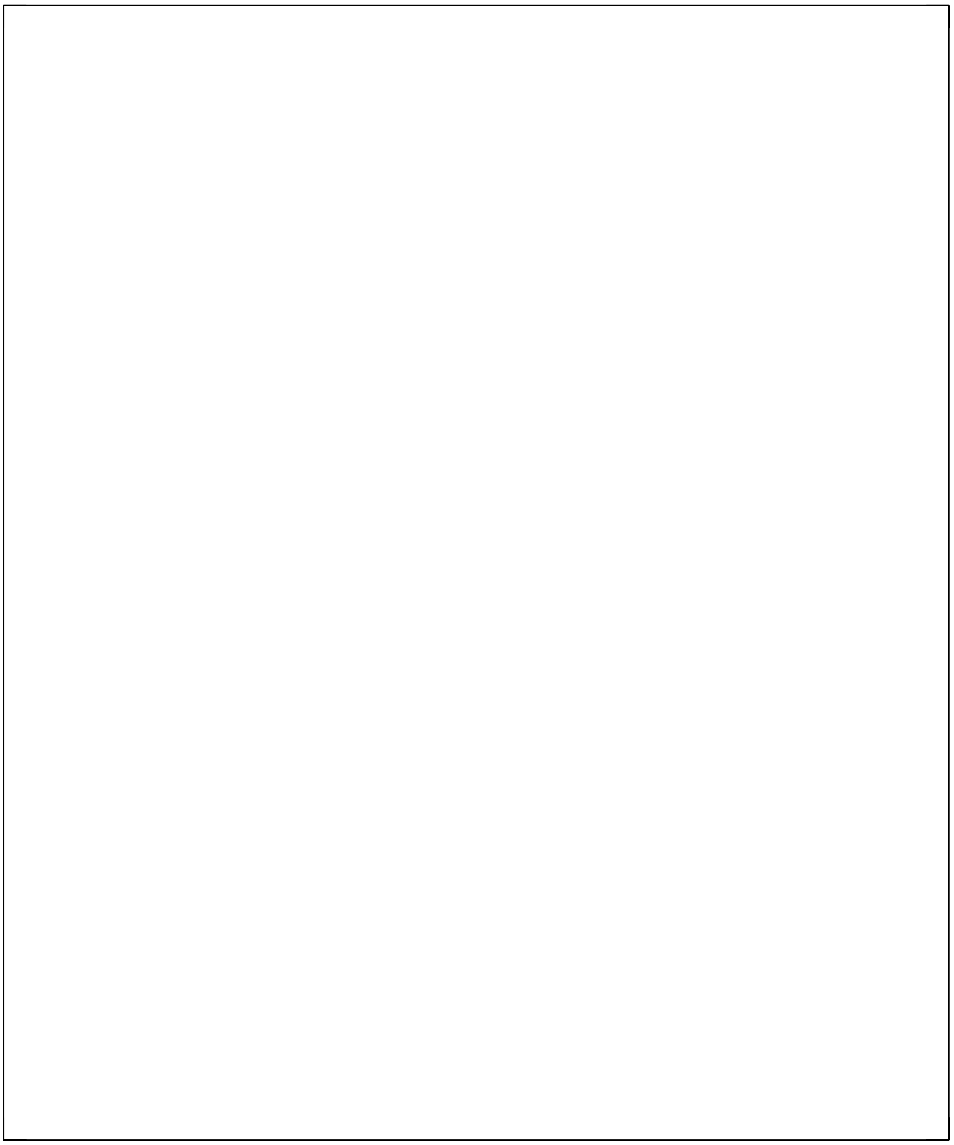

Figure 1.3: Slope parameters measured by UA4 experiment at $\sqrt{s}$=546 GeV (Ref. [16]).

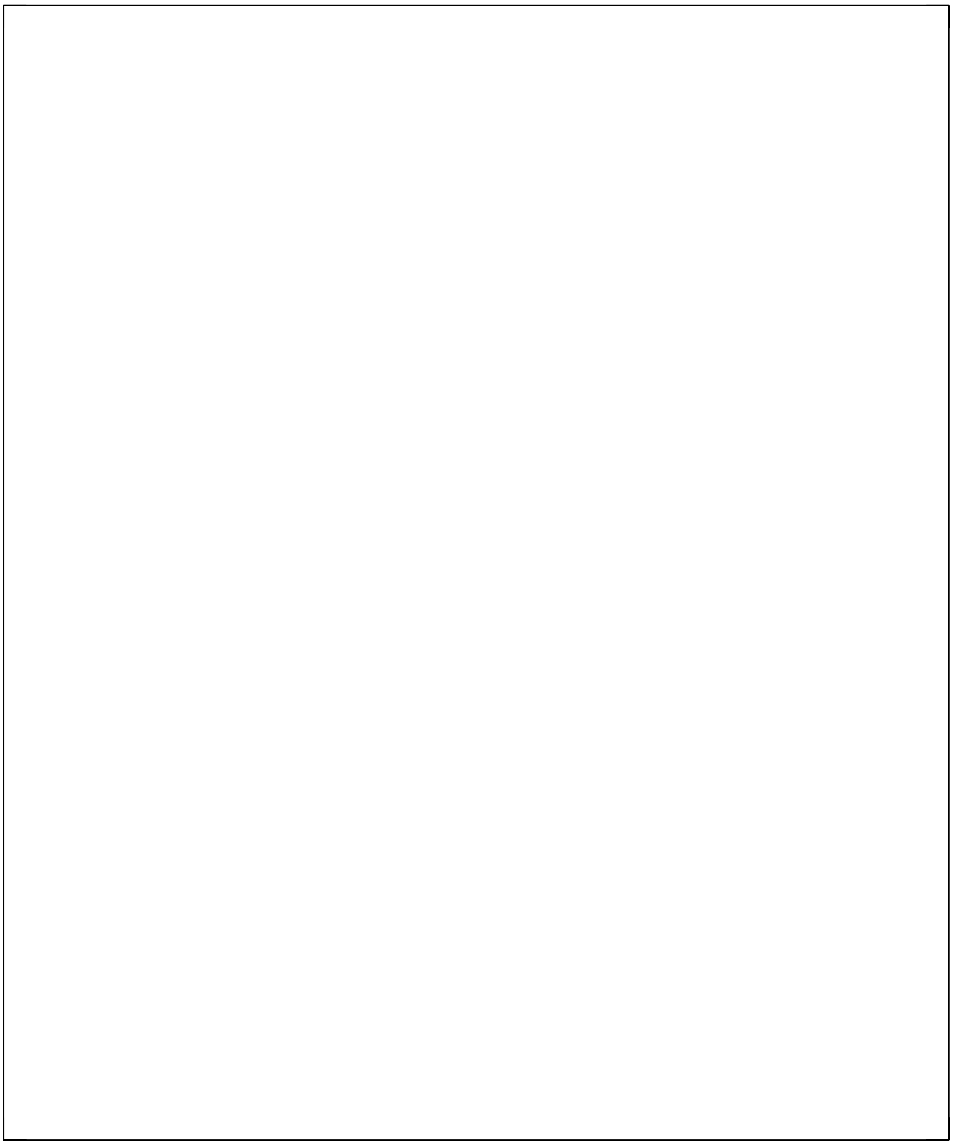

Figure 1.4: Observation of a dip in $\frac{d\sigma}{dt}$ for $P\overline{P}$ and PP interactions (from Ref. [51]). a) UA4 and ISR data. b) E710 $P\overline{P}$ data at $\sqrt{s}$=1800 GeV with a theoretical curve.

mb at $\sqrt{s}$=5 GeV to a minimum of 41.5 mb at $\sqrt{s}$=20 GeV and then started rising to $\sigma_T(P\overline{P})$=43.5 mb at $\sqrt{s} = 62GeV$ ([20]).

Recent experiments at Fermilab, E710 and CDF, have found that at $\sqrt{s}$=1800 GeV the total cross section is still increasing with energy although their values differ by about 7 mb (about 2 standard deviations difference). This difference is crucial for extrapolations at higher energies, and also for other experiments at the same energy that need to normalize to the total cross section.

Figure 1.5 shows a comparison of σ_T(P$\overline{P}$) and σ_T(PP) at different energies (Tevatron data is not shown).

1.5.4 ρ, The Ratio of the Real to the Imaginary part of the Forward Scattering Amplitude

Figure 1.6 shows the behavior of ρ(PP) and ρ(P$\overline{P}$). It has been observed that at lower energies $\rho(P\overline{P})$ is positive, decreasing with the energy until reaching a minimum and then starts increasing again. $\rho(PP)$ is negative at lower energies but increases towards positive values with $\sqrt{s}$, Experiments performed at $\sqrt{s}$= 52 GeV and $\sqrt{s}$=62 GeV show that $\rho(PP)$ and $\rho(P\overline{P})$ seem to converge to the same value. One can make extrapolations from lower energy data, and by use of dispersion relations ([12]) predict what can be expected at higher energies in the event that there is not a new phenomenon involved when the energy is increased, experiment UA4/2 has made a measurement of the ρ value at $\sqrt{s}$=546 GeV ([8], ρ=0.135$\pm$0.007) and experiment E710 measured ρ at $\sqrt{s}$=1800 GeV ([14], ρ=0.14$\pm$0.069). Both of these measurements are in agreement with the extrapolations from lower energy data.

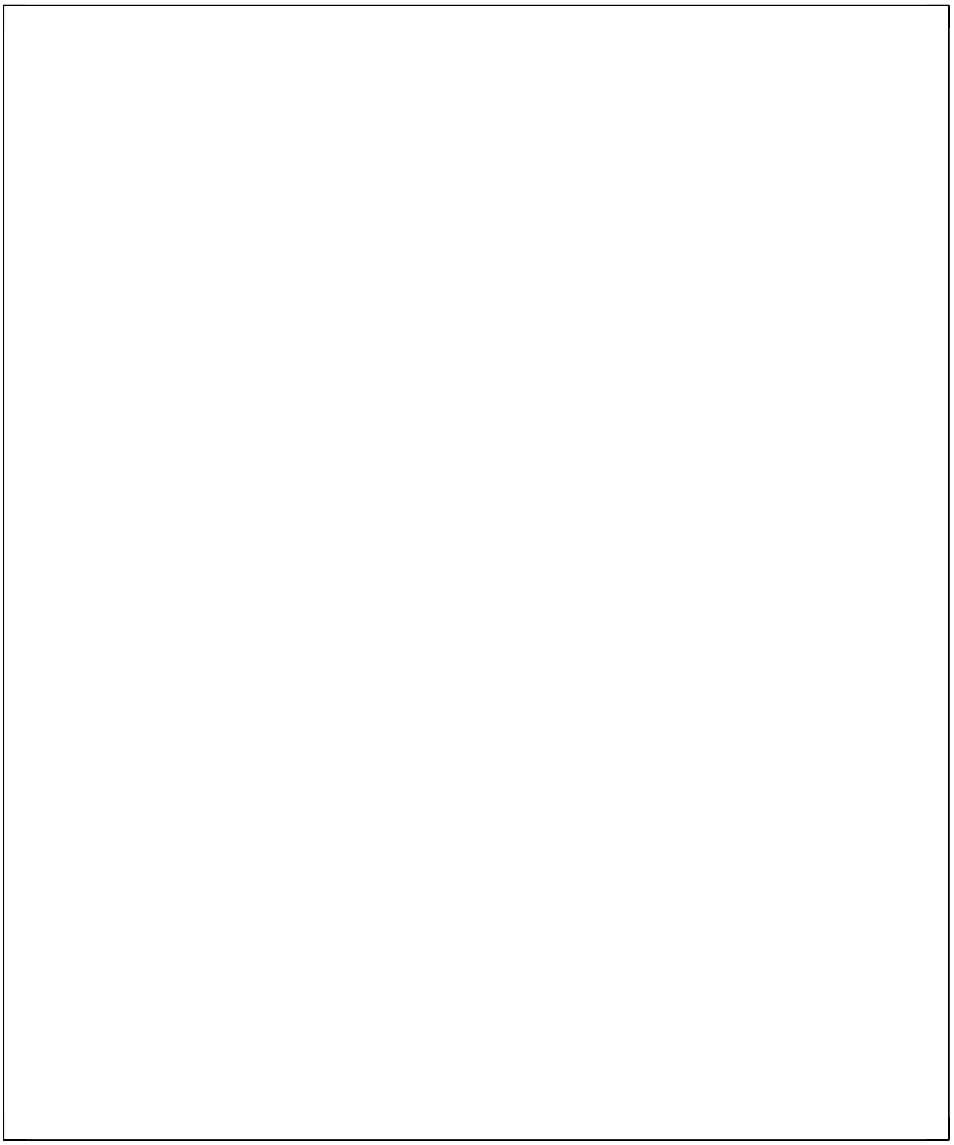

Figure 1.5: Comparison of $\sigma_T(\mathrm{P}\overline{P})$ and $\sigma_T(\mathrm{PP})$ at different energies (from Ref. [21]).

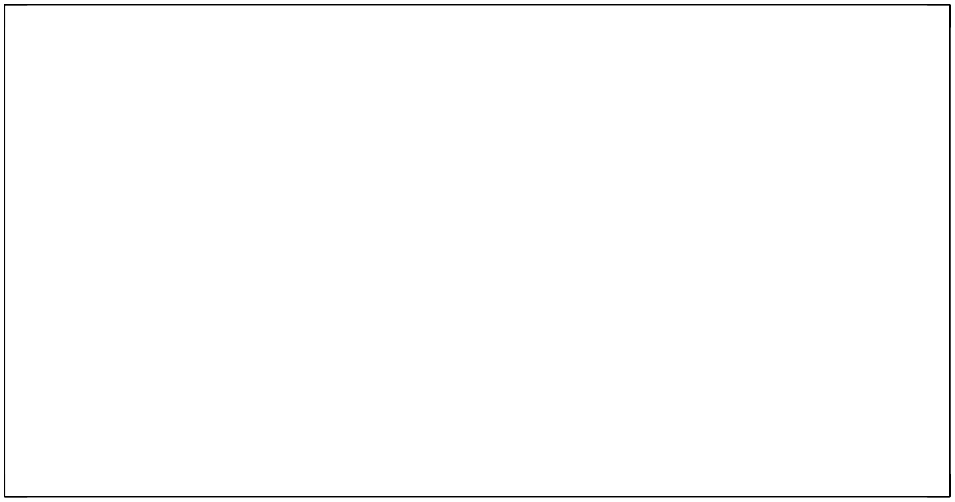

Figure 1.6: Comparison of $\rho(\mathrm{P}\overline{P})$ and $\rho(\mathrm{PP})$ at different energies (from Ref. [51]).

CHAPTER 2

Experimental Setup

2.1 The Fermilab Collider

The Fermilab accelerator complex allows the production of proton-antiproton collisions up to $\sqrt{s} = 1800$ GeV. Figure 2.1 shows a schematic view of the accelerator system. The acceleration process starts with the creation of negative hidrogen ions from a hidrogen gas bottle where H^- ions are extracted with a kinetic energy of 18 KeV which then get accelerated to a kinetic energy of 750 KeV by an electrostatic Crockoft-Walton accelerator. The H^- ions are then injected into a 79 meter Alvarez drift tube linear accelerator which accelerates the ions to 116 MeV and then after going through a 67 meter side-coupled linear accelerator the ions reach an energy of 400 MeV. Electrons are stripped off from the negative ions in the Booster, which is a 151 m diameter synchroton with a total of 96 magnets, that produces 8 GeV protons that then get injected into the Main Ring. The Main Ring is a former 400 GeV proton synchroton with a radius of 1000 meters with 774 dipole magnets, 240 quadrupole magnets and 18 dual RF cavities which operate at a frequency of 53 MHz. All the magnets used in the Main Ring are conventional copper coiled magnets. Protons in the Main Ring are accelerated to 150 GeV and

then they get transferred to the Tevatron where they are finally accelerated to 900 GeV an then get stored in the Tevatron ring. Antiprotons are produced by extracting 120 GeV protons from the Main Ring onto a nickel target. For every 10^{12} protons striking the target about 10^7 8 GeV antiprotons are produced which then get collected by a focusing magnetic lens and directed to the Debuncher. The Debuncher takes the antiprotons coming from the target with the same bunch structure as the Main Ring and reduces their momentum spread but produces a large time spread. Antiprotons are then extracted from the Debuncher and injected into the Accumulator. Successive batches are accumulated by RF stacking. The emittances of the stack are reduced by stochastic cooling which consists of the application of kicks of appropriate magnitude to the stored antiproton beam. About 6 x 10^7 antiprotons are stacked at every pulse. After few hours of stacking about $\approx 10^{11}$ antiprotons get accumulated. At that time antiprotons can be taken out of the stack, injected into the Main Ring and later from the Main Ring they get injected into the Tevatron.

The main feature of the Tevatron is that all its 216 quadrupoles and 774 dipole magnets are superconducting and are cooled with liquid helium to a temperature of 4.6 K. The magnets then carry a current of 4400 A. The Tevatron ring has the same diameter as the Main Ring and is placed about 65 cm below the Main Ring. The Tevatron operates such that there are six proton bunches and six antiproton bunches circulating in opposite directions, with two main collision regions which correspond to the two main detector facilities at Fermilab, D0 and B0. Proton and antiproton collisions occur every 3.5 μs (this is the RF clock we use in our experiment).

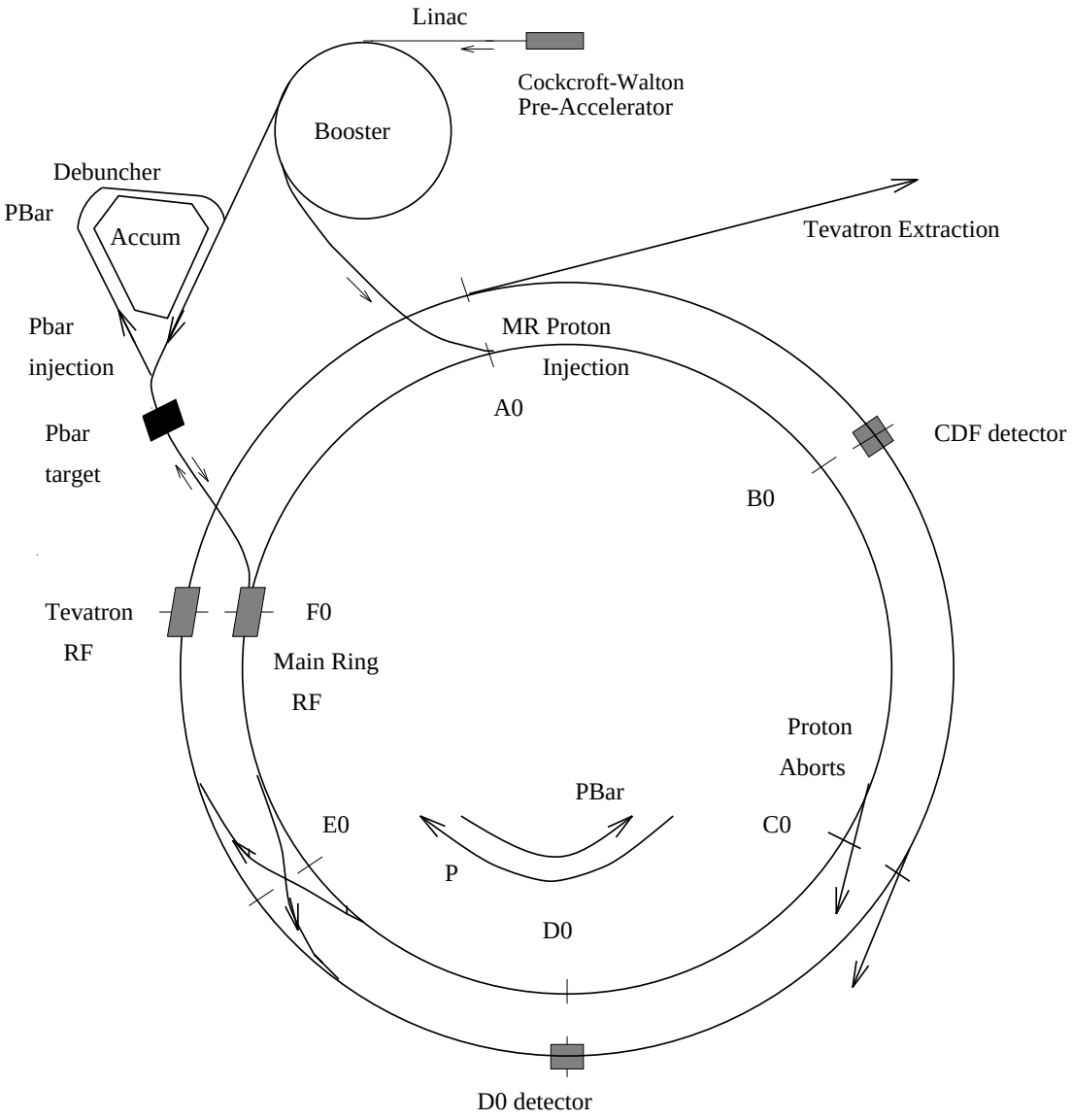

Figure 2.1: Fermilab accelerator complex.

Collisions at E0 and C0 are avoided during normal operation, to increase the luminosity at B0 and D0, by using electrostatic separators. Only for special runs, like the E811 experiment runs, the electrostatic separators were turned off. For normal Tevatron operation the number of protons per bunch is about 200 x 10^9 and the number of antiprotons is about 50 x 10^9. Peak luminosities obtained during the last Tevatron run (run IB during 1995-1996, see [50]) were over 2.0 x 10^{31} $cm^{-2}sec^{-1}$. The running conditions for our experiment are far from normal since we require small beam sizes to be able to locate our detectors as close as possible to the beam. To achieve our running conditions heavy beam scraping has to be done with the use of collimators in the machine. Our running conditions produce of the order of 5 x 10^9 particles per bunch (see Section 2.8).

A more detailed description of the Fermilab accelerator can be found in reference [49] and very detailed information about accelerator parameters and performance can be found in reference [50].

2.2 E811 Experiment

Figure 2.2 shows the layout of experiment E811. The experiment was located at the E0 interaction point in the Tevatron ring. There is a $\pm$25 meter straight section (with no magnets) around the E0 interaction point where we located 44 scintillation counters at 11 different places to count the inelastic events. The pseudorapidity range covered by the counters was $3.8 < \eta < 6.5$. The detectors to track the elastic events were located at two different locations in the accelerator lattice. One location was at 124 m to the right of the interaction point(when viewed from the center of the accelerator ring) where we tracked the scattered protons. The

other location was at 91 m to the left of the interaction point to track the scattered antiprotons. There were accelerator bending and focusing magnets between the interaction point and the location of the elastic detectors. The number of dipole and quadrupole magnets between each detector location and the E0 point was different (see Table 2.1), having as an effect different angular coverage between the scattered proton detectors and the scattered antiproton detectors. The effective distances from E0 to the detectors were about 80 m in the vertical plane and 46 m in the horizontal plane for the pbar detectors and 74 m in the vertical plane and 31 m in the horizontal plane for the proton detectors (see Table 4.4).

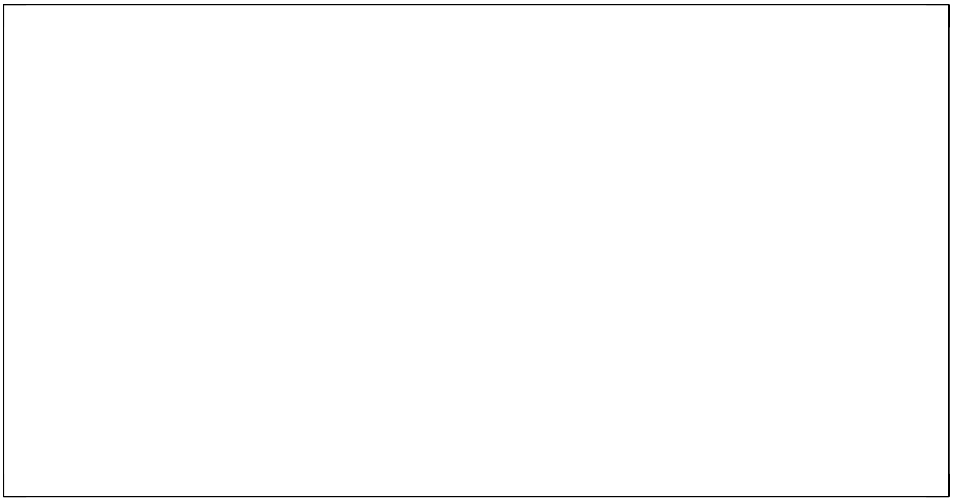

Figure 2.2: E811 schematic experiment layout.

The elastic detectors were placed inside the accelerator beam vacuum, one above and one below the circulating beam at each location and they were mounted

Table 2.1: E811 Lattice.

distance from E0 (m)	element	side with respect to E0
91.0	pbar detector	$\overline{P}$
86.3	dipole	$\overline{P}$
79.9	dipole	$\overline{P}$
73.5	dipole	$\overline{P}$
67.1	dipole	$\overline{P}$
61.9	quadrupole	$\overline{P}$
51.5	dipole	$\overline{P}$
45.1	dipole	$\overline{P}$
38.7	dipole	$\overline{P}$
35.2	quadrupole	$\overline{P}$
30.4	quadrupole	$\overline{P}$
0.0	E0 interaction point	
30.7	quadrupole	P
35.4	quadrupole	P
39.7	dipole	P
46.1	dipole	P
52.5	dipole	P
58.9	dipole	P
64.1	quadrupole	P
68.6	dipole	P
75.0	dipole	P
81.4	dipole	P
87.8	dipole	P
92.3	quadrupole	P
98.4	dipole	P
104.8	dipole	P
111.2	dipole	P
117.6	dipole	P
122.1	quadrupole	P
124.0	proton detectors	P

on a system with movable flanges and bellows that allow accurate vertical positioning with remote control which let us locate the detectors at different positions above and below from the beam. We were able to locate the detectors as close as 2.7 mm from the beam axis (see Table 2.4) reaching a minimum $|t|$ value of $|t| = 0.00092(GeV/c)^2$; around this $|t|$ value for $\sqrt{s} = 1800$ GeV is where nuclear-coulomb interference is expected to be maximum and where coulomb and nuclear scattering have equal contributions to the number of events (about 44 % each). Two scintillation counters were installed with each tracking detector for triggering and calibration purposes.

2.3 The Elastic Detectors

A view of one elastic detector is shown in Figure 2.3. The particle tracking is done by using a scintillating fiber bundle (made by Kuraray co., [58]) that is 45 mm long which has a semicircular cross section with 9 mm radius. The bundle is suspended inside the Tevatron vacuum pipe. The fibers in the bundle have a hexagonal cross section and are 100 μm diameter. The core of the fibers is polysterene plastic with an index of refraction of 1.59. The polysterene is doped with 1% weight of P-terphenyl and 0.2% weight of 3-Hidroxiflavone (3HF). The transmission peak in the scintillating bundle occurs at λ=530 nm which is the wavelength for the best optical transmission in polysterene; the fluorescence decay time for the 3HF is about 7.8 ns. The cladding of the fibers consists of a double layer. The first layer is made of PMMA (polymethylmethacrylate) with an index of refraction of 1.49. The second layer is made of a material with an index of refraction of 1.42. The thickness of each layer of cladding is 3 μm. There is an improvement of about 1.7 in the amount of light trapped in the double cladding fibers compared to single

cladding fibers ([40]).

In order to detect very small scattering angles we locate the flat face of the scintillating bundle as close as possible and parallel to the beam. However to avoid missing the particles that could travel through the cladding, the fibers were tilted in the vertical plane by about 6 mrad from one end to the other, the further fiber end from the interaction point being higher. In this way we guarantee that any particle scattered at E0 that hits the bundle will traverse at least 3 to 4 fibers.

The scintillating bundle is glued with a very high grade vacuum epoxy to a fiberglass light guide that has a 98 degree bend to transport the light produced in the fibers to the readout system that is outside the vacuum pipe. The fiberglass light guide has a circular cross section with 10 mm radius and is made of non scintillating glass fibers of 20 μm diameter. The glass to flange seal is mounted on bellows that allow alignment of the bottom of the scintillating bundle. Only half of the fiberglass light guide is used for transporting the light from the scintillating bundle to its readout system. The other half of the rod is used to transport the light of a scintillation counter that has been glued in the back of the detector and which is part of the triggering system (we named this counter as the "heel counter").

There is a scintillation counter that has been glued in the front face of the scintillating bundle (which we call the "toe counter"). The light of the toe counter is transported out of vacuum by a plexiglass light pipe and read out by a photomultiplier tube (Phillips XP1911). A particle scattered at E0 hits first the toe counter then goes through the scintillating fiber detector and then hits the heel counter.

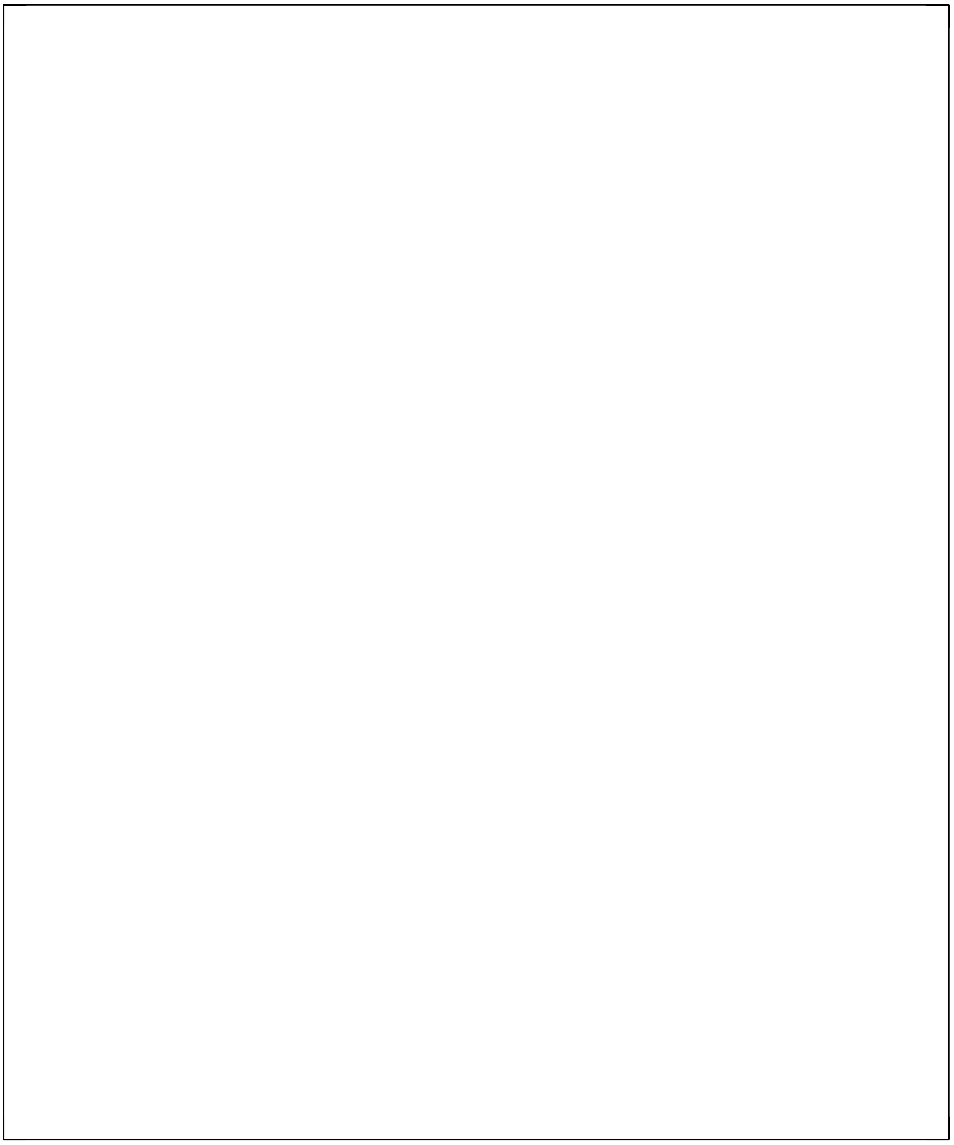

Figure 2.3: E811 scintillating fiber detector.

The complete system that is inside the Tevatron beam pipe is aluminized to avoid light produced by synchroton radiation from the circulating protons and antiprotons to get into any part of the detector.

2.3.1 Fiber Readout System

We used two double proximity microchannel plate image intensifier tubes (DEP XX1450) in cascade to amplify the light produced in the fibers. The face of the glass rod outside the vacuum is optically coupled to the photocathode of the first image intensifier. DEP XX1450 image intensifiers have a quantum efficiency of about 15%. They are made with an S20 photocathode and a P46 screen and with optical fiber windows (18 mm diameter) to allow better optical contact, reduce cross talk effects and produce a cutoff for the ultraviolet range. The P46 phosphor has a peak spectral response at $\lambda = 530$ nm and a decay time of about 160 ns (from 90 % to 10 %).

Half of the phosphor screen window of the second image intensifier (the image intensifier area that amplifies the light produced in the bundle) is coupled to a 2:1 taper which then is coupled to a ccd. The taper is used for matching the sizes of the ccd with the phosphor screen although it produces a reduction in light intensity by a factor of 4 (the ratio of the areas of its two faces). The other semicircle of the phosphor screen, which corresponds to the area of the image intensifiers that amplify the light produced in the heel counter, is coupled to a plexiglass light pipe with an angle of 15 degree that transports the amplified heel light to a photomultiplier tube (Hamamatsu R5600-U). The 15 degree angle was due to space restrictions. In our initial design we used a PIN diode (Hamamatsu s2662-03) instead of the photomultiplier tube to read out the heel counter light. The

physical dimensions of the PIN diode were appropriate but its low gain made it inefficient to see minimum ionizing particles.

The image intensifier gain depends on the voltages supplied to the microchannel plate and phosphor screen (anode). At nominal settings (maximum settings are -200V for photocathode, 800 V for microchannel plate and 6.0 KV for the phosphor screen) we measured a gain of about 10,000 for the system of fiberglass light guide and the two image intensifiers in cascade. Our voltage settings were such that we ran at about half of the maximum gain that could be achieved (our voltage settings were typically -200 V for the photocathode, 750 V for the microchannel plate and 5.5 kV for the anode). The light transmission in the fiberglass light guide was measured to be about 75 %.

The gain of these so-called second generation image intensifiers is accomplished by means of a microchannel plate. The microchannel plate is a thin disk (about 0.5 mm thick) made of 12 μm capillary glass tubes tilted by a small angle, (see Figure 2.4).

The top and bottom surfaces of the disk are metallized and kept at different voltages, the input face is grounded, we usually apply 750 Volts to the output face (maximum voltage to be applied is 800V). Every capillary tube acts as an electron multiplier keeping good spatial resolution. Where an electron initially produced in the photocathode hits a wall of a capillary tube in the microchannel plate, secondary electrons are emitted which are accelerated by the voltage difference between the two surfaces of the disk. Because of the tilting angle, secondary electrons hit again the walls of the capillary tube producing more secondary electrons. This process is repeated until the electrons reach the end of the disk when

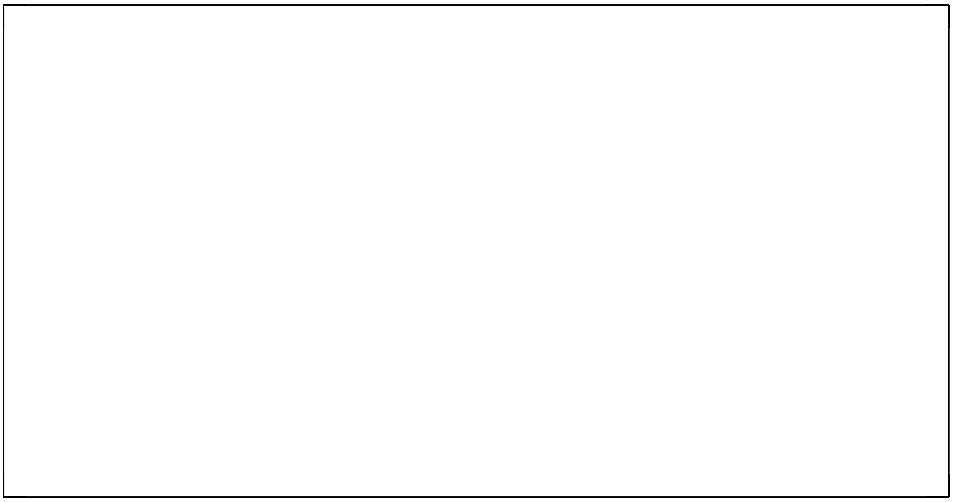

Figure 2.4: Microchannel plate.

they get accelerated towards the phosphor screen which is usually kept at 5.5 kV.

Another advantage of using second generation image intensifiers, apart from their high gain and distortion free-preservation of the image, is their capability of fast gating. We gated the photocathode of the first image intensifier after a trigger was produced to guarantee that no light from other particles went through the readout system. The other time when the image intensifiers were gated off was during the Main Ring injection and ramping or during any busy signal produced in our experiment. The gating circuit was adjusted such that the rise time for the gate was about 300 ns. The image intensifiers were turned on again after the busy signal of the experiment was released.

The ccd used was an EEV ccd 29-06 which is a three phase clocking MOS structure with anti blooming, fast clear facility and asynchronous readout. The total number of pixels in the ccd is 768 x 292, each with a dimension of 11 x 22 μm, the image region area is 8.5 x 6.4 mm. The ccd spectral response along with the spectral responses for other parts of the detector are shown in Figure 2.5.

Figure 2.6 shows the principle of operation of a p-type three phase clocking ccd (from reference [57]). Figure 2.6 (a) shows the basic structure of a p-channel MOS ccd, it is composed of an n-type substrate, an oxide layer and an electrode. Figures 2.6 (b)-(e) show the basic operation of one pixel of the ccd which is composed of three electrodes. When a negative voltage is applied to the electrode, the negative carriers are repelled away producing a depletion region below the electrode. If the electrode voltage is increased the depletion region is extended into the substrate. The negative potential attracts holes to the depletion region until they form a conducting channel at the oxide-semiconductor interface. The depletion region

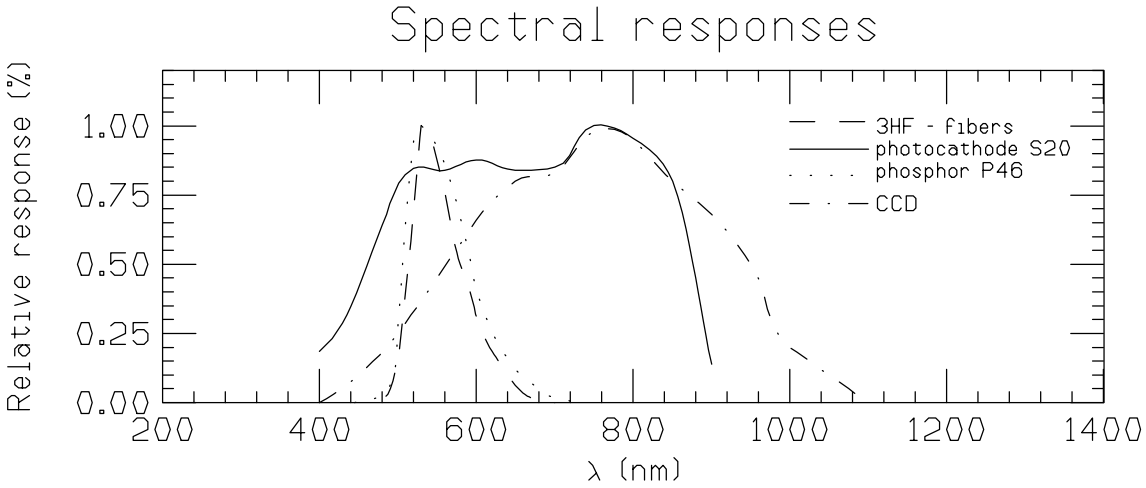

Figure 2.5: Spectral response for different parts of the detector.

can be considered as a potential well (although the holes are located immediately below the electrode, one can consider that they are confined into the well). Photons striking the ccd produce electron-hole pairs, electrons get repelled because of the negative polarity of the gate and the resulting holes are trapped into the potential well, the potential well is made deepest by applying a greater negative voltage to electrode ϕ_1 than that applied to electrodes ϕ_2 and ϕ_3 making the charge package to be located under ϕ_1 (Figure 2.6 (b)) A short time later the voltage applied to electrode ϕ_2 is increased and the voltage to ϕ_1 is reduced, the charge packet is then transferred to the deepest well (2.6 (c)); When the voltage applied to electrode ϕ_1 has decayed into its lowest value the potential well has been completely transferred to underneath electrode ϕ_2 (2.6 (d)). Later the voltage applied to electrode ϕ_3 is increased and the voltage to electrode ϕ_2 is reduced, then the charge package moves again to the right (2.6 (e)). For commercial ccd operation the charge is allowed to accumulate for 20 ms (European standard) and then by applying the three phase clock pulses the stored charge gets shifted to a memory area. The transfer time

from image area to memory area takes about 300 μs. The memory area can be read out while the ccd image area starts accumulating charge again. The memory zone is also an array of pixels not light sensitive just used to store the charge that is transferred from the image area of the ccd. The ccd also had the ability to prevent excess photocharges in a saturated pixel to spread out to neighboring pixels, this is obtained with an antiblooming electrode. When there is excess of charge in one pixel the charge excess falls into the anti-blooming drain instead of spreading out to neighboring pixels.

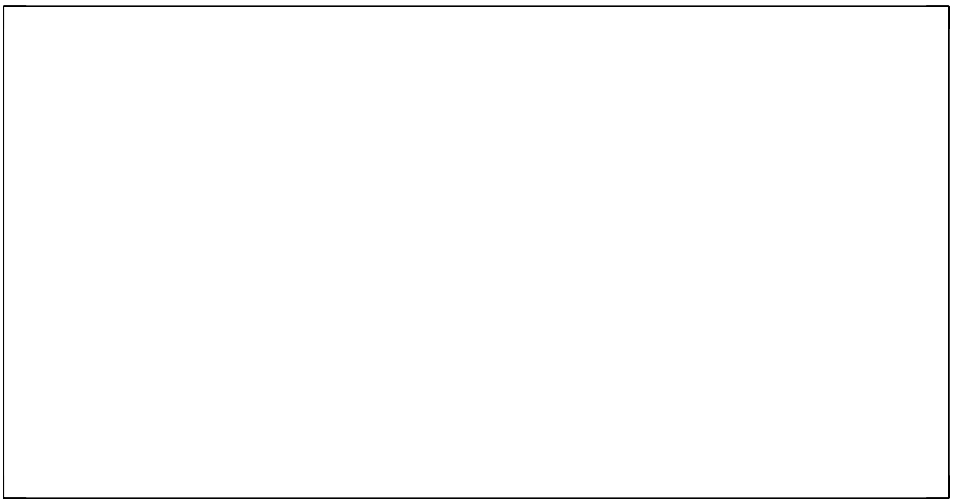

Figure 2.6: Principle of operation of a ccd.

The readout of the ccd is produced by a serial transfer of the pixel charges on the memory zone to an output register. The transfer is done by clocking the pixel electrodes in each horizontal line which is then transferred to the next until

all lines have been transferred. The readout time for one horizontal line is 64 μ s. To distinguish one line from the next one to read out, a pulse in between lines is generated (this is what we call horizontal synch). Once all the horizontal lines have been read out, a pulse is created to indicate that a complete ccd frame has been transferred from the memory area to the readout register and a new frame starts (this pulse is what we call the vertical synch), this pulse is made wide enough (0.5 ms) to include the time for synchronizing all the clocks and the transfer time from the image area to the memory area of the new frame. The total readout time for one frame is 20 ms (which is European TV standards). There is an output amplifier connected to the readout register which allows to set different gains in the camera. Gain studies were performed previously to our data taking. The clocks are generated and controlled by the camera electronics (EEV p46810).

The first ccds used in our experiment for beam tests were synchronous ccds. The charge integration time for every frame was the same, 20 ms. Once our trigger counters detected a hit and triggered the experiment electronics we had still to wait until the end of the integration time to be able to read out the frame. On average we had to wait half of the integration time which produced an extra 10 ms experiment dead time. For our final data taking we were able to upgrade our ccds to work in asynchronous mode. We had control of the integration time of the asynchronous ccd, by using a strobe pulse we could control the charge integration time in the image area which was equal to the width of the strobe pulse. The charge transfer from image area to memory area was started with the trailing edge of the strobe pulse. The strobe pulse trailing edge also produced a new vertical synch to allow the readout to start immediately after the charge transfer to the

memory area was completed. The readout time of the memory area was still 20 ms. With this new configuration we were able to reduce the average dead time by about 30 %. The main dead time per event was given by the 20 ms. The ccd readout time limited us to a maximum data taking rate of 50 HZ for elastic events.

Because a bunch crossing in the Tevatron occurs every 3.5 μs we also had to be able to clear the charge produced by a particle that hit one of the ccds but did not produce a master trigger (a master trigger requires 1 ccd on each side of the E0 interaction point to be hit, see Section 2.7). We accomplished this with the fast-clear facility. A fast-clear can be achieved with an extra clock for the voltage of the antiblooming electrodes. Charge accumulated on the pixels after a given time can be transferred to the potential well produced by the antiblooming electrodes if a clock signal reduces the voltage on the pixel electrodes and increases at the same time the voltage of the antiblooming electrodes, then all the charge in the pixels is transferred to the antiblooming drain. The fast-clear takes 1 μs. We fast-clear our ccds before every bunch crossing until a master trigger is generated, at that time the fast-clear signal is vetoed and the strobe pulse indicating the integration time length is terminated transferring the charge produced during the last bunch crossing to the memory area to be read out immediately. The fast-clear operation resumed with the leading edge of the following strobe pulse. It was very important to veto the fast-clear also during ccd readout time because the clocking of the electrodes to produce the fast-clear also induced some pickup noise on the readout register that resulted in spurious lines observed in the video signal. Notice that the ccd operation with asynchronous readout and fast-clear operation makes redundant the gating of the image intensifiers for the readout of the spot of light

produced by an event that triggered the experiment. The gating of the image intensifiers was still important to save the system from the high illumination levels that could happen when the Main Ring produced showers of particles as a result of losses, and some of those showers hit our detectors. References [41]- [43] give a more detailed description of ccd operation and characteristics.

2.3.2 CCD Dark Current and Radiation Damage

Dark current on the ccds was produced by two main sources, one is thermal noise and the other is pixel radiation damage. Dark signal noise due to thermal effects doubles for every 10 degree celsius temperature increase. We cooled down our ccds with dry air produced by a commercial air conditioner and connected to an air blower to get the air to the location of the ccd cameras. The air temperature was stabilized at about 15 $\pm$ 0.5 celsius as read out by a thermister located at each camera near the ccd chip. The most important factor for us was to keep the temperature constant, so that the dark current from frame to frame in the same run was about the same. Thermal dark current not only accumulates in the image area but also in the memory area. The ccd readout is done by transferring every horizontal line to the next until all the lines are read out by the output register. The dark current in the first line read out is lower than the dark current for the last horizontal line read out, and this effect produces a non uniform dark current level across the y coordinate of the ccd. The dark current is observed to increase linearly for smaller values of y which correspond to the last lines read out (see frames in Figure 4.1). Pixel radiation damage was an important factor of consideration in our experiment. CCD parameters, according to the manufacturer specifications, are expected to change for radiation levels greater than 10 Krad. Detailed description

on effects of radiation damage on ccds can be found in references [44] and [45].

The radiation levels measured at our detector locations (by using TLD badges) are shown in Table 2.2. The main radiation source was given by particle losses in the accelerator Main Ring. The radiation levels for detectors 3 and 4 were higher than for detectors 1 and 2 because accelerator Main Ring losses were higher near the location of detectors 3 and 4. We put radiation shielding around our detectors. The radiation shielding consisted of polyethelene beads and borax bags to capture some of the neutrons produced by Main Ring losses. After radiation shielding we found that our detectors could survive irradiation for over a month without reaching critical radiation levels (see table 2.2). For our final data taking, new ccds were installed and data taking was done two weeks after the ccds were installed. The first two weeks were used for equipment calibration and voltage settings. Pixel radiation damage during the two week period of exposure did not produce dark current levels that could affect our data. The first cameras installed for beam tests did not have any radiation shielding; after about a month of exposure they developed dark current levels that overlapped with the light intensity produced by minimum ionizing particles hitting the bundle. This resulted in unreliable ccd efficiencies and this had a great effect in the efficiencies determination for that beam test runs.

Table 2.2: Radiation levels at our detectors.

	before shielding		after shielding	
detector #	neutrons dose	gammas dose	neutrons dose	gammas dose
1	400 rad/week	200 rad/week	57 rad/week	27 rad/week
2	80 rad/week	5 rad/week	12 rad/week	1 rad/week
3	4000 rad/week	1000 rad/week	1500 rad/week	400 rad/week
4	800 rad/week	90 rad/week	350 rad/week	42 rads/week

The image intensifiers and bundle did not show any effect of radiation damage. The only component that had radiation damage was the fiberglass light guide for detectors 3 and 4. However, we found that they could be cured with exposure to high power ultraviolet light. We used a high power ultraviolet source made by Engineering Fiber Optic Systems (Ultracure 100SS plus) which has a high pressure 100 watt mercury vapor short arc lamp. The light from the lamp was transported by a flexible liquid filled light guide and then it was shined to one face of the fiberglass light guide, with the other face temporarily aluminized. This process was inverted later to shine from the other end too. The light intensity was about 200 watt/cm^2 with light of wavelengths 250 nm and 500 nm. The fiberglass light guide from detector 3 was the most affected by radiation damage, its optical transmission coefficient had been reduced to 21 % after radiation exposure (75 % is the normal transmission measured by us for a non-radiated fiberglass light guide). We found that after 14 hours of exposure the fiberglass light guide recovered to about 90 % of its normal optical transmission coefficient. We exposed to UV light both radiation damaged rods for a period of 40 hours.

The optoelectronic readout was also shielded for magnetic fields, using a μ metal shielding surrounding the readout system. Also the readout system was made light tight.

Image intensifiers, taper, ccd and fiberglass light guide were locked up to each other by using a series of mylar keyed rings. This was done to avoid any rotation or misalignment between the different readout elements during detector installation.

2.3.3 Triggering System

Each elastic detector had two ways to be triggered, either when the toe counter fired or the heel counter fired. Both counters were blue scintillation counters machined into a "T" shape as a way of defining sharp edges to be used for calibration coordinates. Both toe and heel counters had the same dimensions. The size of the elastic trigger counters are shown in Figure 2.7. The heel counter had the disadvantage of being behind the detector, which meant that a particle had to travel through the fiber bundle material and some fiberglass guide material before hitting the heel counter. Some particles that were not traveling inside the fiducial area defined by the heel counter could still make the heel fire from a secondary produced when the particle interacted either with the atoms of the scintillating bundle or with the atoms of the fiberglass light guide.

For calibration, distortion studies and diagnostic purposes we scribed 7 vertical lines and 4 horizontal lines each one 100 μm wide with a very accurate machine forming a reticle pattern at the interface of the toe counter and the bundle. A bright LED was installed at the interface of the toe photomultiplier tube and its light pipe. The LED was pulsed when no beam was in the Tevatron and helped us diagnose the complete system to check for dead or malfunctioning elements. Also data with the LED pattern digitized on the ccd were stored for later studies of distortions and calibrations. Figure 2.7 shows the reticle pattern on one of the toe counters.

The image intensifiers also have the feature of self triggering mode. The charge accumulated in the phosphor after the magnification of a light signal produces a pulse that after amplification can be used for triggering (the anode signal).

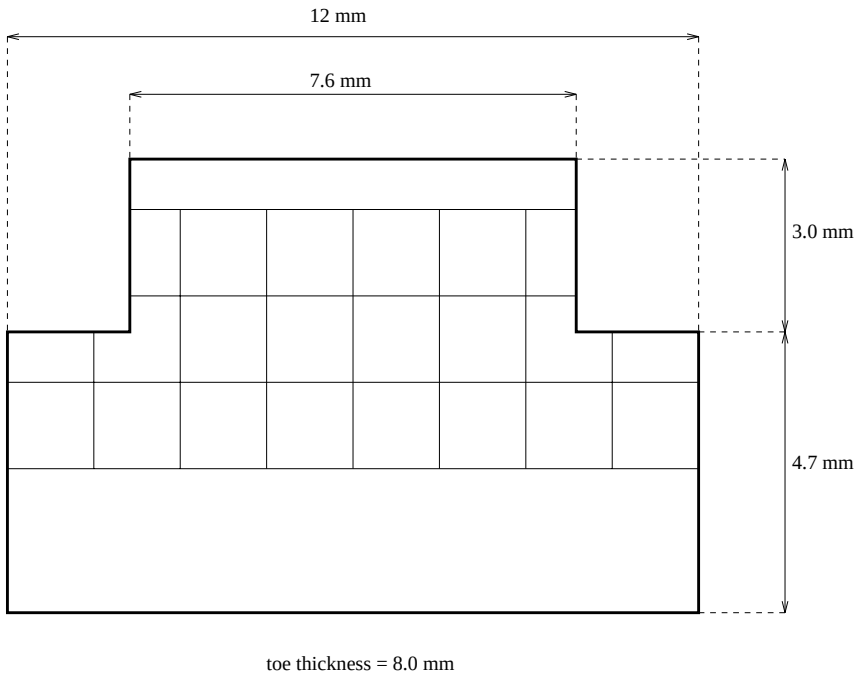

Figure 2.7: Toe counter outline.

However that signal turned out to be not appropriate for our purposes, since it was too slow (the rise time was about 80 ns), with a long decay time and high slew rate and very sensitive to ground loops, having noise pickup from the ccd and accelerator clocks which were very difficult to isolate. The self triggering mode can be used in less noisy environments and where tight coincidences in time are not needed. Another disadvantage of the self triggering mode in our experiment is that because light from the heel counter is also amplified through the image intensifiers the anode trigger signal was coupled to the heel signal. For absolute normalization experiments it is very important to have a trigger independent of the tracking system to avoid any bias in finding efficiencies for the system. In our experiment that independent trigger was given by the toe counter. We still recorded on tape the ADC and TDC information of the anode signal.

2.3.4 Detector Motion System

Each elastic detector has a step motor associated with it that allows detector vertical displacement in a range of 24 mm. We used LVDT's (linear variable differential transformers) as the position sensors for the detector motion system, which are potted coil assemblies with a moving core. In each "castle" (the vacuum vessel holding the two elastic detectors at the same location in the Tevatron ring) there are two sets of LVDT's installed, the primary and secondary LVDT's. Each set of LVDT's consists of three position sensors, the first two measure the position of the upper and lower detector with respect to the center of the castle and the third one measures the distance between upper an lower detectors. The second set of LVDT's is a copy of the first one which is used for getting higher system redundancy.

A block diagram of the the detector motion system is shown in Figure 2.8 . Each detector motor is powered by a motor drive amplifier. The motor drive amplifiers are controlled by the motor servo units in the VME crate in the experiment control room. Each motor servo controls its corresponding motor amplifier, it compares the desired position entered as a parameter in the computer to the actual digital position obtained from the LVDT drivers which are the ones that read out the position sensor and digitize the position information and then transmit it to the motor servo unit. If there is a difference between the desired position and the actual digitized reading the motor servo unit allows another 10 μm motor step. The process is stopped once the difference between desired position and actual position is within 10 μm. Once the detectors are positioned to the desired values with respect to the center of the castle the LVDT drivers keep updating the posi-

tion information with a period of about 1 ms. The accuracy in detector position measurement with the LVDT system was found to be about 20 μm. Detector motion is only performed by Tevatron control room operators due to the risk of quenching the store if the detectors are run into the beam. There were different precautions taken to avoid the chances of quenching the beam, the first one is that while moving the detectors, the counting rates of the toe counters were supervised and a maximum value for each detector was entered as a parameter on the detector motion software, the maximum value set was 100 KHz. We also used limit switches which allow a minimum distance between each detector and the center of the castle. The minimum distance was set to be 1.5 mm. As a redundancy, in case the limit switches fail we also had hard stops for a minimum distance between the upper an lower detector in one castle, the hard stops were machined to allow a minimum distance of 4 mm.

To compensate the torque produced on the detector motors by the Tevatron vacuum we used compressed air at a pressure of 120 psi. The LVDT sensors were previously calibrated in a table bench before final installation in the accelerator tunnel. After our data taking we also did a final calibration by reproducing the detector positions at which we had taken data and by measuring with parallel blocks and a caliper the distances of the movable flanges where the detectors were mounted to the central flange in the castle. With a precision machine we later measured the distance of the flanges where the detectors were mounted with respect to the bottom edge of the toe counters. With these measurements we were able to determine very accurately the distance between the upper and lower detector in the same castle for each run where we located our detectors to take data. These

distances are shown in Table 2.4.

2.4 The Video Data Acquisition System

The video signal from each ccd camera was transported from the detector location in the Tevatron tunnel to the experiment control room through a 75 ohm RG11 signal cable. All the other signals from the detectors and detector motion controls, camera controls and image intensifier gate signal were transported through RG8 50 ohm cables. High voltages were supplied through RG58 high voltage cables. The length of the cables was about 300 meters. The video signal at the experiment control room end was plugged into a synch stripper board, which is a special board that takes the video signal as an input and produces as an output the clocks needed for recognizing each horizontal line (horizontal synch) and the clocks needed to know the end of a frame and beginning of a new one (vertical synchs). The video, horizontal synch and vertical synch signals were then connected to the video data acquisition system (VDAS, developed at Fermilab) which digitizes and compacts the video information. Each VDAS system (there is one per elastic detector) consists of a FIFO controller, an ADC compactor, a trigger+synch board, a FIFO memory board and an external device bus board (EDB board) (see Figure 2.9). The VDAS system can be seen as a matrix of 500 x 300 elements, we just called each element a VDAS cell which has dimensions of about 45 μm x 45 μm. Once the video signal is received, the ccd pixels get mapped into the vdas cells. The vdas intensity thresholds, the digitization process and data compactification , which are explained below, are performed on the vdas cells. What we actually see in the recorded data on tape and work with in the analysis is the vdas cells rather than the ccd pixels. We make the convention from now on that every time the word

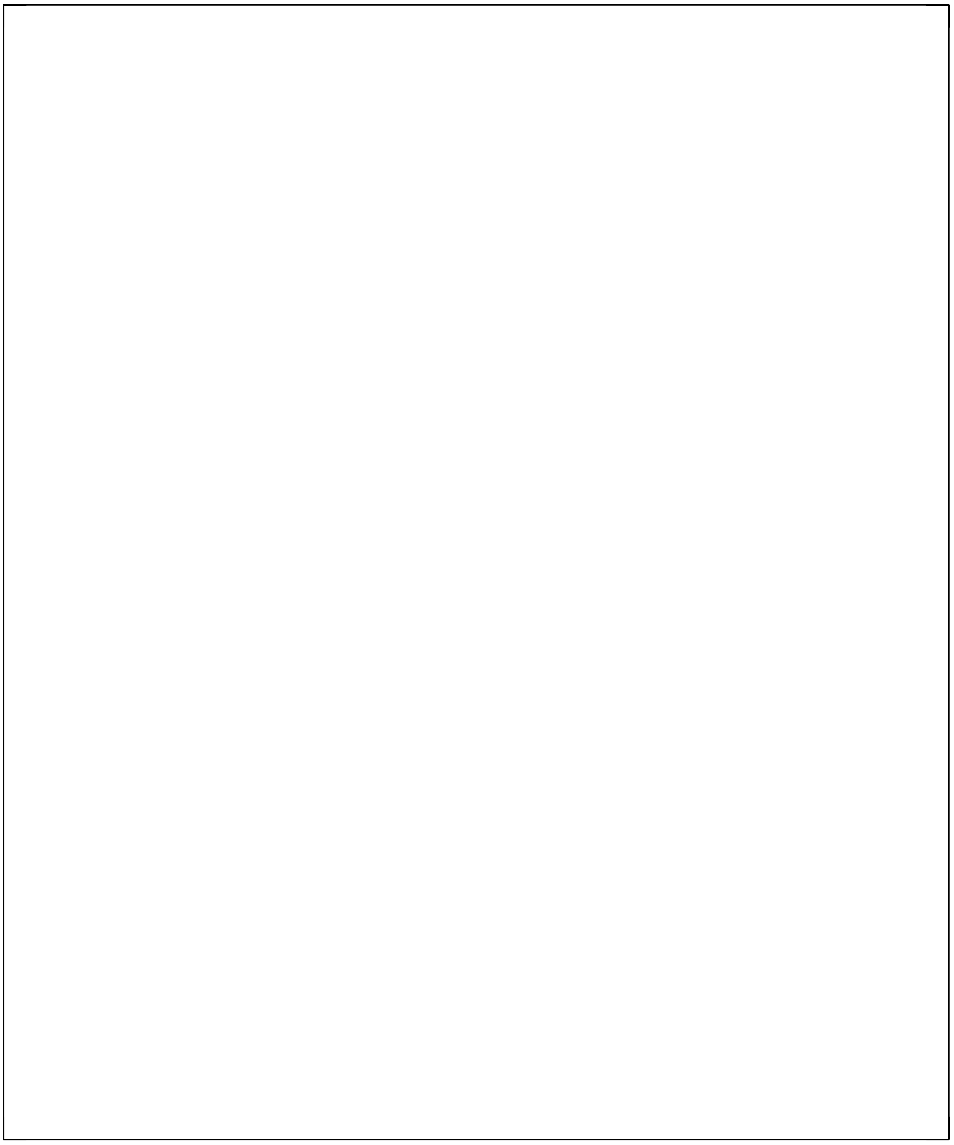

Figure 2.8: Block diagram for the detector motion system.

"pixel" is mentioned in the following sections of this document is to refer to a VDAS cell.

The trigger and synch board receives as an input the video signal, the horizontal synch, the vertical synch and a trigger. It also has two adjustable potentiometers to set the minimum and maximum levels for the digitization of the pixel intensity information that comes with the video signal. Any pixel intensity below or above the the two thresholds set is assumed to be 0. For our case we set the upper threshold to be above pixel saturation level and the lower threshold to be above the average pixel intensity for ccd dark current which was determined previously in our data taking period. There were still some noisy pixels surviving the lower threshold that got digitized and written onto tape, but these pixels usually correspond to the last horizontal lines to be read out by the output register on the ccd camera (see Figures 4.1 a) and b)). The trigger+synch board at the arrival of a trigger produces a busy signal (although delayed by about 2μs), assigns an event ID and waits until the next vertical synch is recognized before passing the information to the ADC compactor. The ADC compactor digitizes the pixel information within the two threshold limits set in the trigger+synch board with a 6 bit fast ADC and also counts the number of adjacent pixels with 0 intensity (intensity not within the threshold range). The information from the ADC compactor gets stored into the FIFO memory boards. The EDB i/o serves as interface to access the FIFO memory cards from the computer (which is either a VME 167 board or just a terminal). The FIFO controller board controls data operations, provides holding registers for memory cycles to write and store data, moves pointers to requested memory locations given from the computer and also gives the status of memory (full, near full, empty, near empty, read/write in progress, etc.). A detailed description of

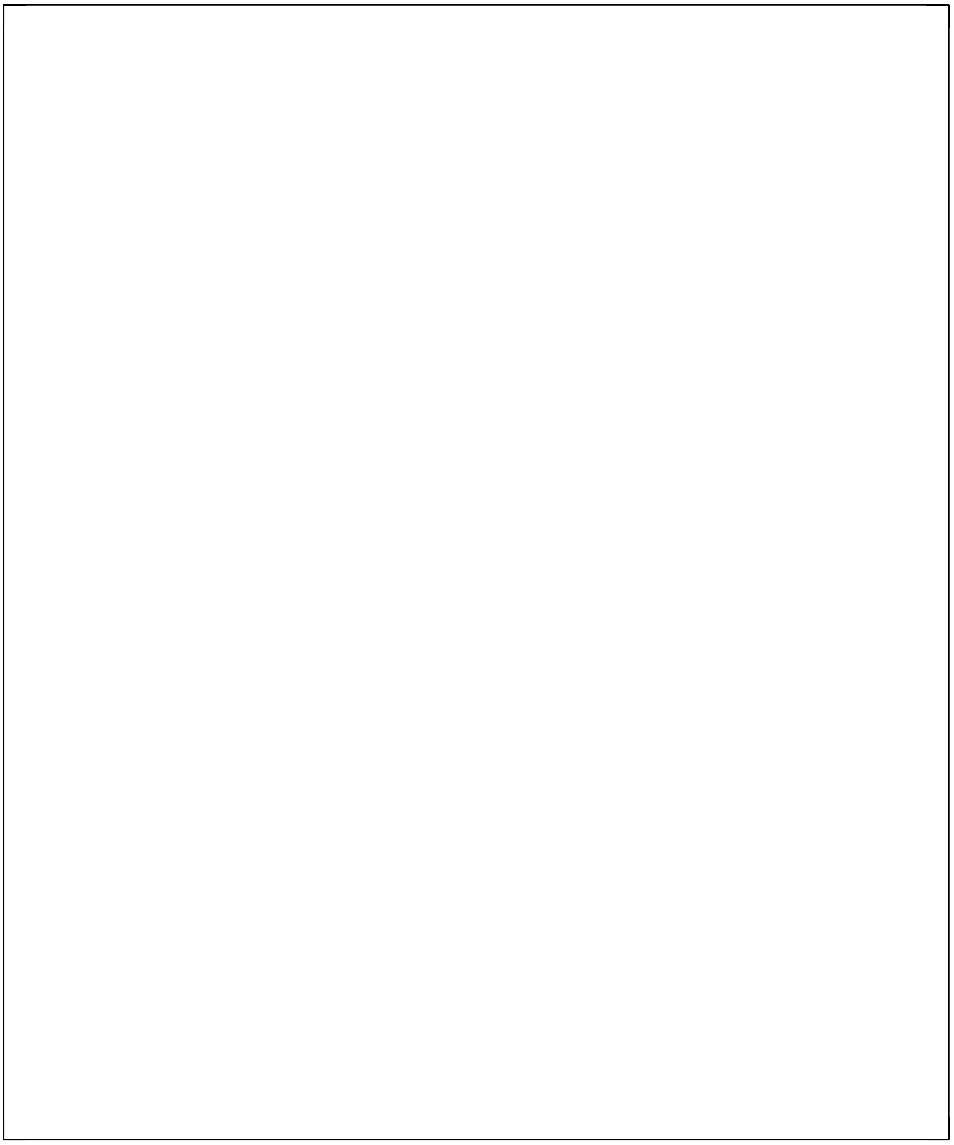

Figure 2.9: VDAS circuit layout.

operation and control of the VDAS system can be found in reference [48].

2.5 The Data Acquisition System

Most of the software for the DAQ system was developed at Fermilab by the DART group (Data Acquisition in Real Time). The experiment data acquisition system reads out the information stored on the FIFO memory boards of each vdas system and the ADC, TDC, trigger register and scaler information stored in 4 camac crates. The event readout of the camac and VDAS systems is controlled by a VME 167 microprocessor using Vxworks operating system. The DAQ subroutines are downloaded and developed from an INDIGO SGI machine which is connected through the VME crate via internet. The SGI computer is also used for online event monitoring using a HOIST server which allows an interface of the general PAW package (Physics Analysis Workstation, developed in CERN) and the VME 167 microprocessor for online event monitoring.

The data buffer was of variable size because of the compactification done in the VDAS system for the ccd information. In average all 4 VDAS systems added up to 10 KByte of data. The camac crates added an extra 1.5 Kbyte of data. The event builder program in the DAQ builds the data buffer to be written on tape. In case the DAQ system is triggered with an inelastic trigger (see Section 2.7.4) the data buffer to be written on tape only contains CAMAC data. Only when the DAQ is triggered with an elastic trigger the event builder concatenates the information from each VDAS system and then adds the CAMAC information. There was a third type of trigger for the DAQ and it was for the accelerator data which was recorded on tape every minute. The accelerator data contained parameters about

the beam conditions like bunch intensities, luminosity, emittances, etc.

2.5.1 Optical Distortions

We studied optical distortions in the different pieces of the detector before assembling them together to make sure that we only use detector elements for which distortions could be corrected later on in the analysis stage. To study distortions of the scintillating bundle and fiberglass light guide we used a 500 μm x 500 μm grid reticle which was placed in the front face of each of these two elements separately before detector assembly. Line was shined underneath the grid reticle and a camera was focused on the other side to see the transmitted reticle lines trough the bundle or fiberglass guide. The camera had a cross hair at the center and the scintillating bundle (or fiberglass guide) was mounted on top of a movable table with micrometer positioning in both X and Y coordinates. By aligning the camera's cross hair on top of each line intersection of the observed reticle, we were able to determine the X,Y coordinates of that intersection point. A connection between the micrometer and a PC allowed automatic recording of the position of each intersection. At the end we ended up with a map of the transmitted reticle that we could use for correcting distortions for an individual element. Figures 2.10 and 2.11 show the mapped points obtained for the scintillating bundle and fiberglass light guide for detector 4 (the detector with the worse distortions). Also in those plots is shown the area of the toe reticle which is the region of interest.

For studying the distortions of the detector readout system we used a negative of the reticle described above such that only light trough the reticle lines could be transmitted. That reticle was optically coupled to the photocathode of the first

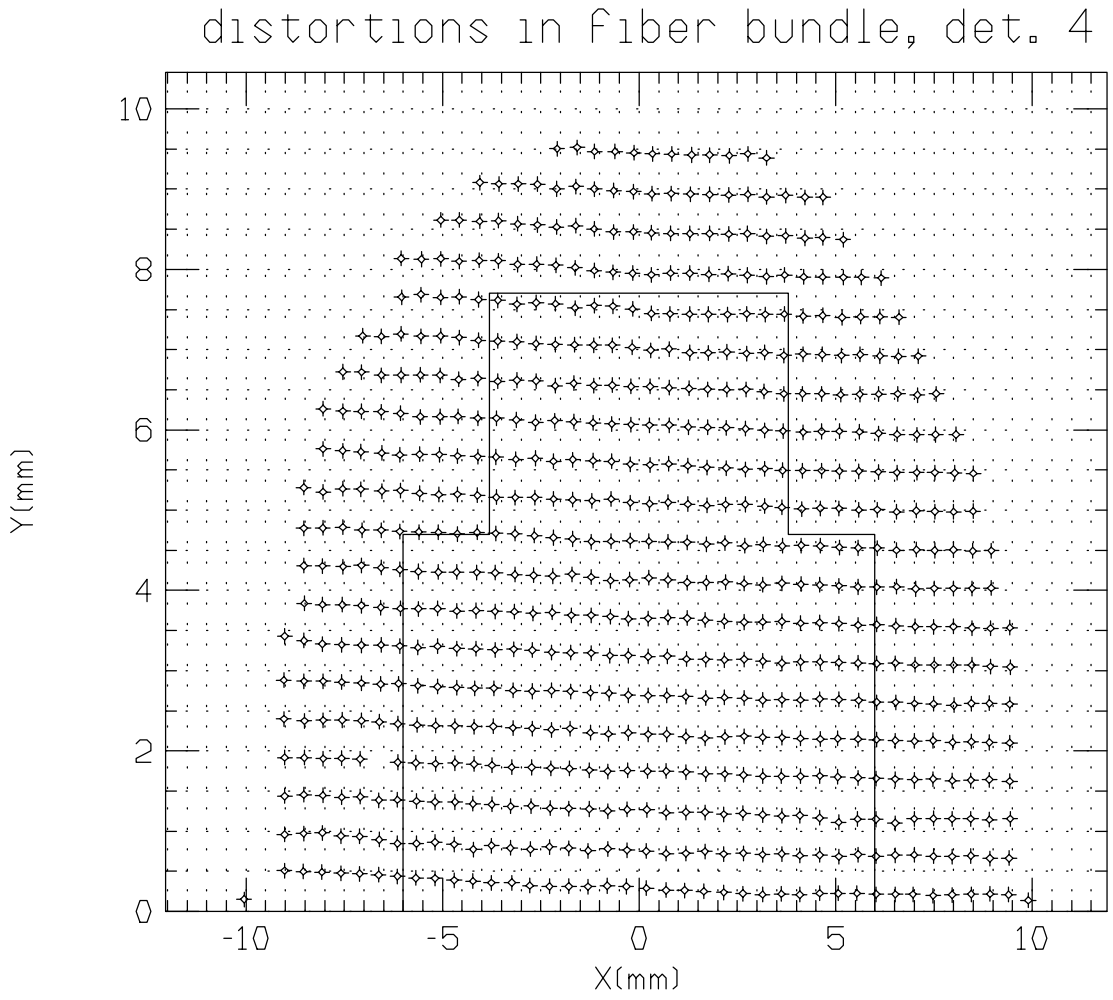

Figure 2.10: Distortions in the scintillating fiber bundle of detector 4. A 500 μm x 500μm reticle pattern is observed through the scintillating bundle.

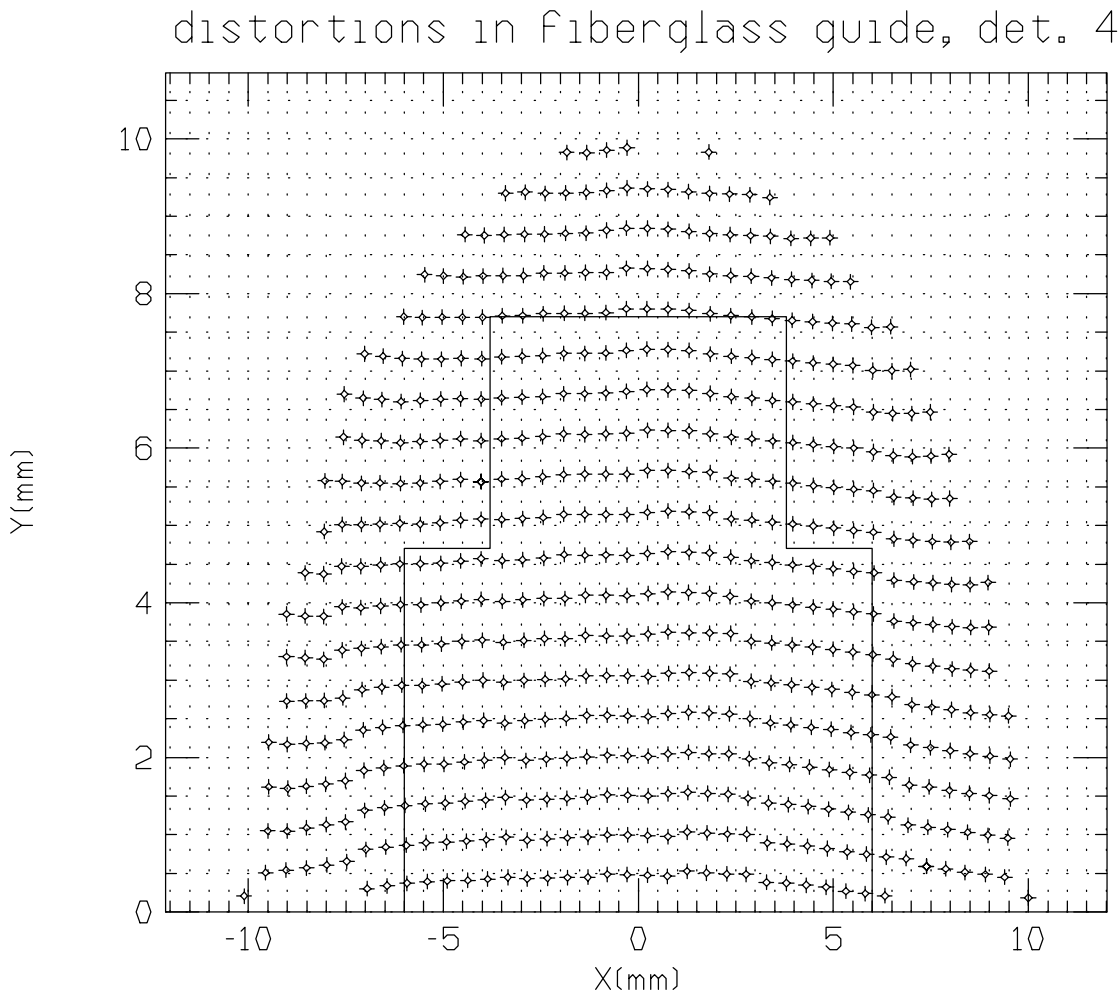

Figure 2.11: Distortions in the fiberglass light guide of detector 4. A 500 μm x 500 μm reticle pattern is observed through the fiberglass light guide.

image intensifier, an LED was placed underneath the reticle and the image intensifiers and ccd were turned on with gain settings used to observe minimum ionizing particles. Figure 2.12 shows the reticle reconstructed from reading out the data that we recorded on tape by using the complete readout system for detector 4. The same process was run for all 4 detectors. The conclusions made by studying each detector piece separately was that the fiberglass light guide and the scintillating bundle were the main contributors to optical distortions in the detector, while the distortions in the optoelectronic readout were very small. After detector installation in the Tevatron pipe we found that detector rotations also have to be taken into account when correcting for distortions, this is because particles hitting the bundle do not follow the same path as light in the front face of the bundle. Also shifts in glueing pieces together have to be taken into account for doing the distortion corrections for the whole detector system. For the final analysis we decided to use the reticle scribed on the toe counter for doing the distortion corrections of the whole detector (see Section 4.2).

2.6 The Inelastic Counters

The inelastic counters were placed at 6 different locations at the left side (L_0 to L_5) of the interaction point and 5 different locations at the right side (R_1 to R_5) of the interaction point. At each location there were 4 annular counters (α, β, γ and δ) forming a ring around the Tevatron beam pipe. Figure 2.13 shows the distances of each ring counter with respect to the interaction point and the value of pseudorapidity covered by that counter. The inner diameter of the ring counters was equal to the diameter of the beam pipe at that location. For counters L_0 to L_4

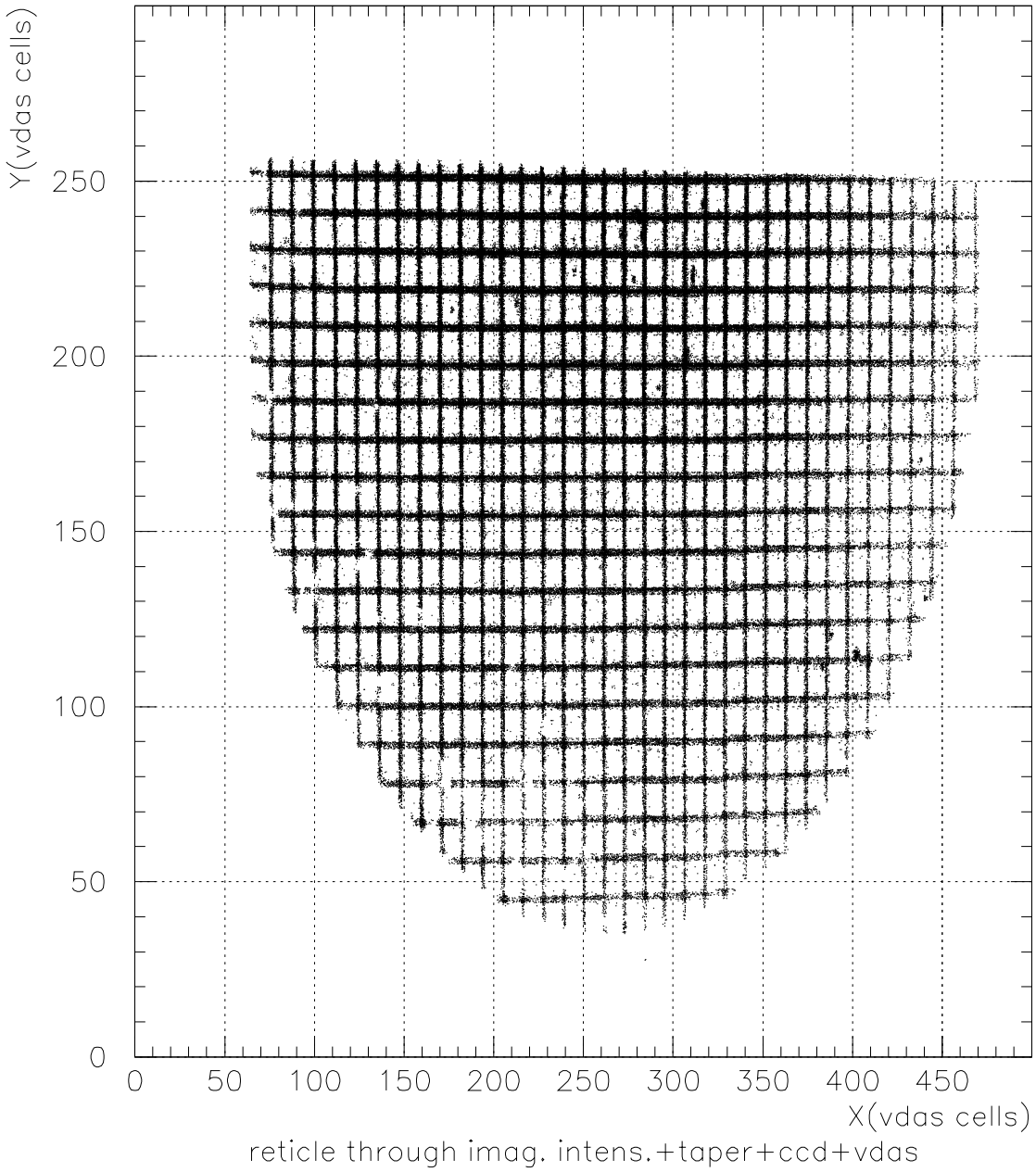

Figure 2.12: Distortions in the opto-electronic readout system of detector 4. A 500 μm x 500 μm reticle pattern is observed through the image intens.+taper+ccd+VDAS.

and R_1 to R_4 the inner diameter was 101.6 mm. Counters L_5 and R_5 had an inner diameter of 76.2 mm. The height of all the counters was 25.4 mm and they were 6.4 mm thick. Each counter was read out by a Phillips XP2262 photomultiplier tube. Since the minimum scattering angle that the inelastic counters could observe was 3 mrad, the probability of having an elastic scattering event at that angle compared to the angles covered by the elastic detectors was negligible.

2.7 Experiment Fast Logic

2.7.1 Elastic Counters Logic

The block diagram for the elastic trigger counters logic is shown in Figure 2.14. There are three trigger signals obtained from each elastic detector: the toe trigger counter signal, the heel trigger counter signal and the anode signal. We record on tape ADC and TDC information for each of them. The rates used for monitoring vertical detector motion are taken from the toe counter in coincidence with the RF signal. We put in an "OR" the toe and heel trigger signals for the upper and lower detectors located at the same place and then make the coincidence to the RF. Time delay curves were made during experiment tune up to find the delay on the trigger signal such that the coincidence to the RF occur only for particles with time of flight consistent with particles scattered at the E0 interaction point. An elastic trigger ($O * O$ trigger) is produced by the coincidence of the RF signal with at least one toe or heel counter of detectors 1 and 2 and with at least one toe or heel counter of detectors 3 and 4. Detectors 1 and 2 are also called "D" detectors in some of our diagrams because they are located at the D47 point in the accelerator lattice. Detectors 3 and 4 are the "E" detectors because they are located at the E14 point. We start the TDC's and the gates for the ADC's and

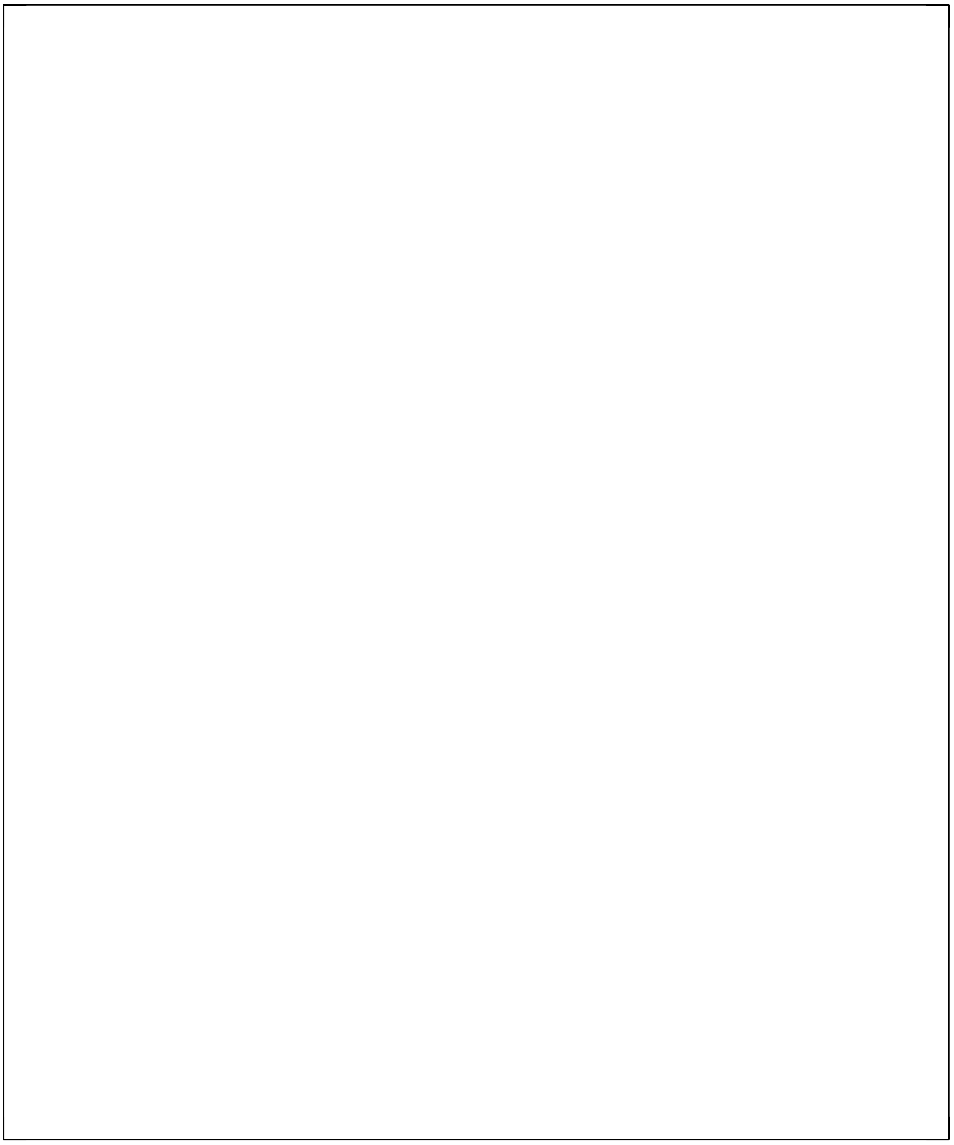

Figure 2.13: Ring counters.

trigger bit registers only if there is a hit in any of the elastic counters (toe or heel) or any hit in any of our ring counters.

2.7.2 Inelastic Counters Logic

Figure 2.15 shows the block diagram for the logic of the inelastic counters. Trigger counters L_3, L_4 and L_5 are put in an "OR" to produce the L_{3-5} signal which produces the L trigger signal after coincidence with the RF clock. In a similar way the R signal is produced from counters R_3, R_4 and R_5. The L and R trigger signals are used to record events that we call single arm events since they only require hits at one side of the interaction point. Also the coincidence of the L and R signals produce the LR trigger which is the double arm event trigger since it requires a hit at each side of the interaction point.

The L_{3-5} and R_{3-5} signals are made 200 nsec wide and clipped before making the coincidence to the RF, which is equivalent to producing a 200 ns deadtime after a hit in any L_{3-5} or R_{3-5} counter. This is done to avoid triggering on particles produced by beam-gas scattering at the opposite side before the collision at E0 takes place. The 200 nsec time is called the early hit veto since the type of events vetoed will generally have a time of flight shorter than a particle scattered at E0.

Figure 2.15 also shows how the C trigger signal is produced. We initially put in an "OR" counters L_0, L_1, L_2, R_1 and R_2 and then make a coincidence with the RF signal. These counters are so close to E0 that our TDC's cannot resolve the early hits. So no early veto is made for the C signal.

Notice that the LR signal could be formed by coincidences of the L trigger and an R trigger that do not correspond to an interaction at E0, but instead to

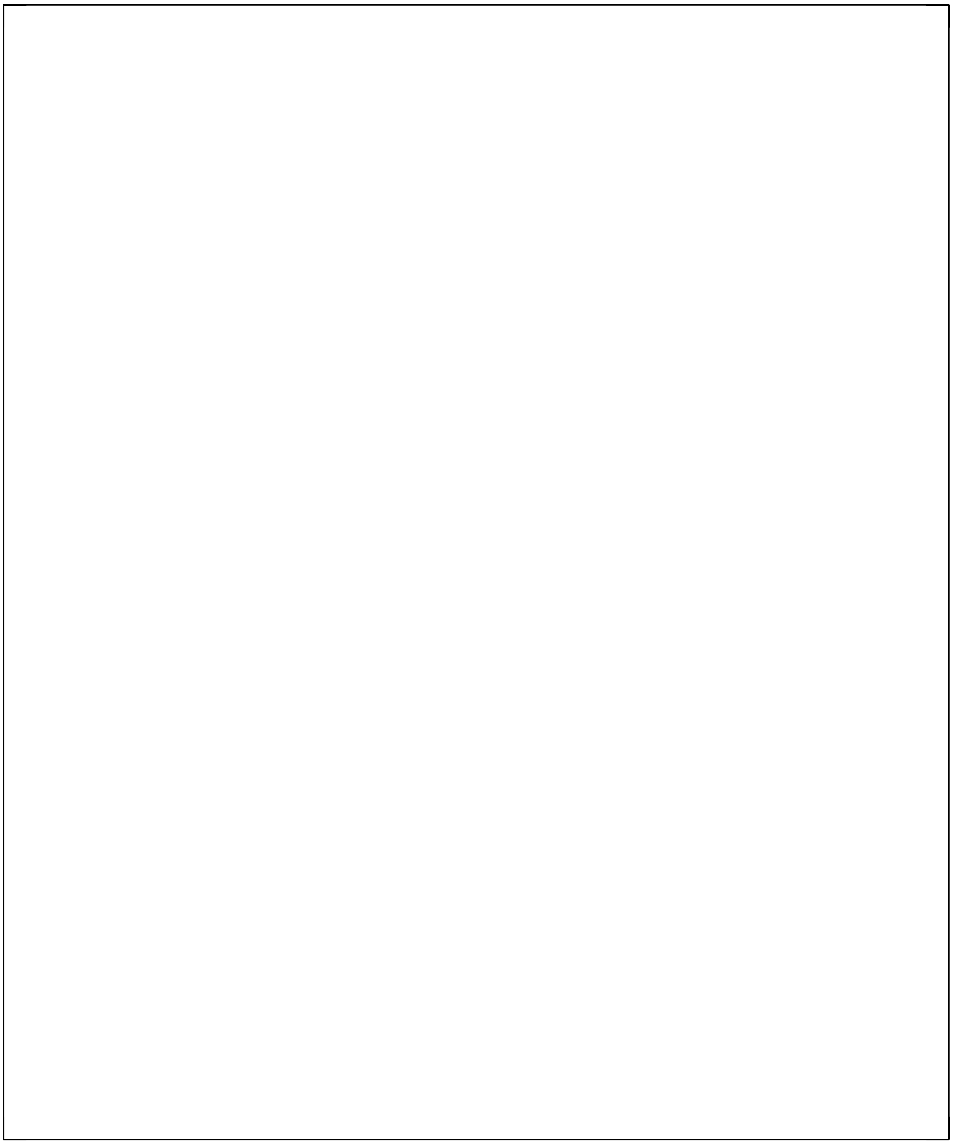

Figure 2.14: Logic for the elastic counters.

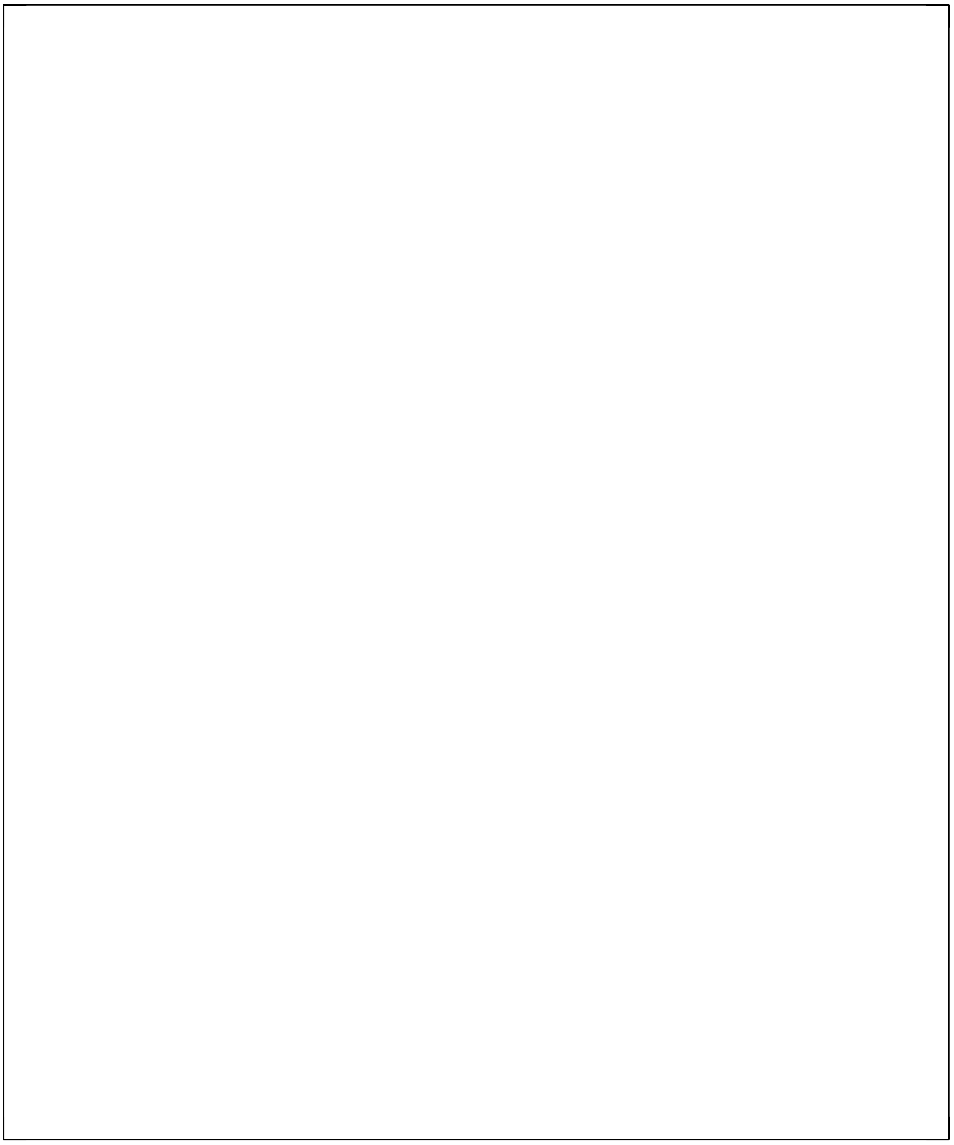

Figure 2.15: Logic for the inelastic counters.

Figure 2.15: (continued)

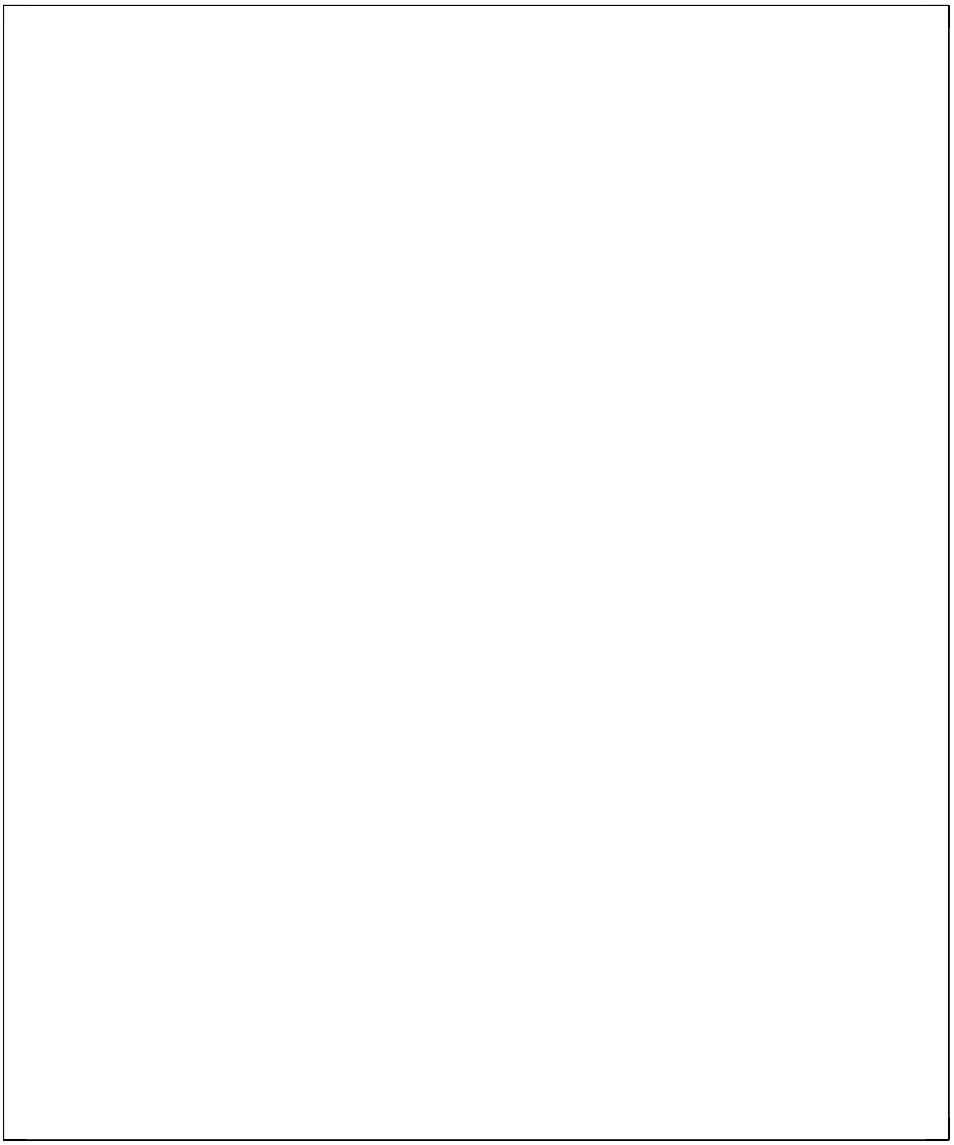

accidental beam-gas scattering at both sides or also accidental noise. One way to estimate the accidental rates in the LR signal is by taking the L trigger signal and delay it by one complete period of travel around the Tevatron ring (21 μs) which means looking at the same bunch crossing after one turn in the machine and make the coincidence to the R signal (this coincidence is called $L_{21}R$, see Figure 2.16). Since the probability of having a good LR after one round in the Tevatron machine is negligible (Inelastic secondaries do not get trapped in the Tevatron for one complete turn) then the $L_{21}R$ signal measures the LR accidentals. In the data analysis we found that the number of LR events that get rejected with the ADC cuts is very close to the number of events predicted by $L_{21}R$ signal which indicates that most of the LR accidentals are from noise pulses.

Figure 2.16 shows the schematic circuit for the logic of the $L_{21}R$ signal. Notice that when we make the delay of 21 μs we reject L events that could have come in the following 5 crossings from the one that is being delayed. To correct for that we just count the number of L events before and after the 21 μs delay. The ratio is the correction to apply. We found that that correction was smaller than 1 %. In the schematic circuit shown in Figure 2.16 we also see a veto to the L signal produced by R_{3-5} signal. That veto is to remove events where one particle fired both R and L counters, i.e. halo scrapping.

2.7.3 Luminosity Monitor

The number of good LR events (LR events produced by an interaction at E0) scales with the luminosity. One way to produce a luminosity monitor is to select a subclass of LR events which are noise free. We have selected this subclass of LR events as the ones that always produce a hit in all 4 counters that form the L_5

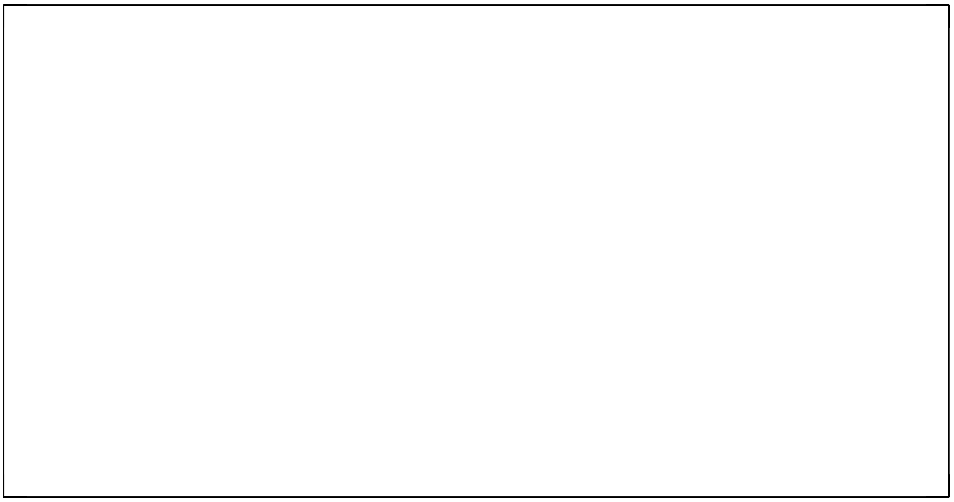

Figure 2.16: Logic to measure the accidental coincidences in the LR trigger.

ring counter (L_5^*) and also produce a hit in all 4 counters of the R_5 ring counter (R_5^*). The coincidence of L_5^*, R_5^* and the RF clock is called M which is our luminosity monitor (see Figure 2.17). We estimate the accidentals on the M signal by delaying by 21 μsec the L_5^* signal and making the coincidence with the R_5^* signal. The accidentals on the M signal are called M'. Since there is not a direct measurement of the luminosity at the E0 interaction point one way to determine the E0 integrated luminosity is by plotting the integrated luminosity measured somewhere else in the Tevatron ring and plot for different runs the integrated luminosity at other accelerator point versus $M - M'$. The slope of a straight line fit to the data is the conversion factor to get from $M - M'$ to integrated luminosity. This procedure was followed earlier in the analysis of the E710 experiment (see [53]). In our analysis we only use the luminosity monitor as a diagnostic tool.

2.7.4 Master Trigger

We have five signals that could be used to trigger the experiment:

1. $O * O$ signal which is the trigger for elastic events.

2. LR signal is the trigger for double arm inelastic events.

3. L signal is the trigger for inelastic events hitting one of the counters L_{3-5}.

4. R signal is the trigger for inelastic events hitting one of the counters R_{3-5}.

5. C signal is the trigger for inelastic events hitting one of the counters L_0, L_1, L_2, R_1 or R_2.

The master trigger is a combination of these signals weighted by different prescaling factors (see Figure 2.18) which were set depending on the conditions

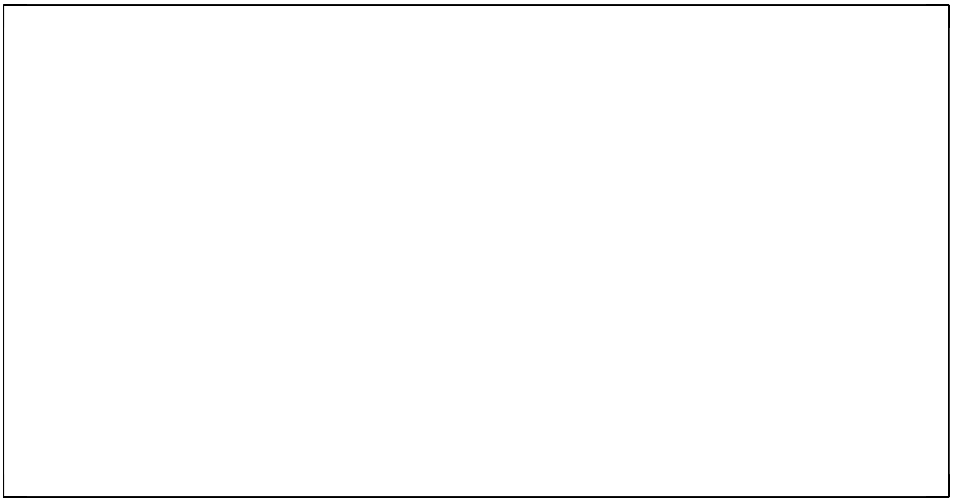

Figure 2.17: The luminosity monitor.

of the run and the type of data we wanted to take. Once a master trigger was generated, immediately a master trigger busy signal was produced to busy out the experiment. This was done because the computer took much longer in producing the computer busy signal. The VDAS systems were only triggered with the $O * O$ trigger. In case of an inelastic trigger and no $O * O$ trigger, only the information from the ring counters was read out. The signal generated to trigger the VDAS systems is what we call the "OUTER TRIGGER" in Figure 2.18. Also VDAS has a delay of about 2 μs in producing a busy signal after it has been triggered, so when we had an $O * O$ trigger, we generated an outer trigger busy 5 μs wide to immediately turn off the image intensifiers and stop the integration time in the ccd. The camac crates were cleared every time there was a hit in one of the elastic or inelastic counters and no master trigger was produced.

2.7.5 Gating

Figure 2.19 shows a block diagram for the experiment gating logic. The photocathode gate is dependent on the experiment gates in the following way:

$$\begin{aligned} \text{photocathode gate} \;=\; & \text{VDAS busy} + \text{outer trigg. busy} + \text{MR gate} \\ & + \text{flying wire} + \text{run switch} \end{aligned} \tag{2.1}$$

where "+" stands for a logical "OR".

We turn off the image intensifiers once we get the VDAS busy signal but since the VDAS busy has a delay of 2 μs we compensate that with the outer trigger busy that is produced immediately after the master trigger. We also turn off the image intensifiers during the Main Ring gate (we gate off the complete experiment during Main Ring injection and ramping) or during a flying wire in the Tevatron or by

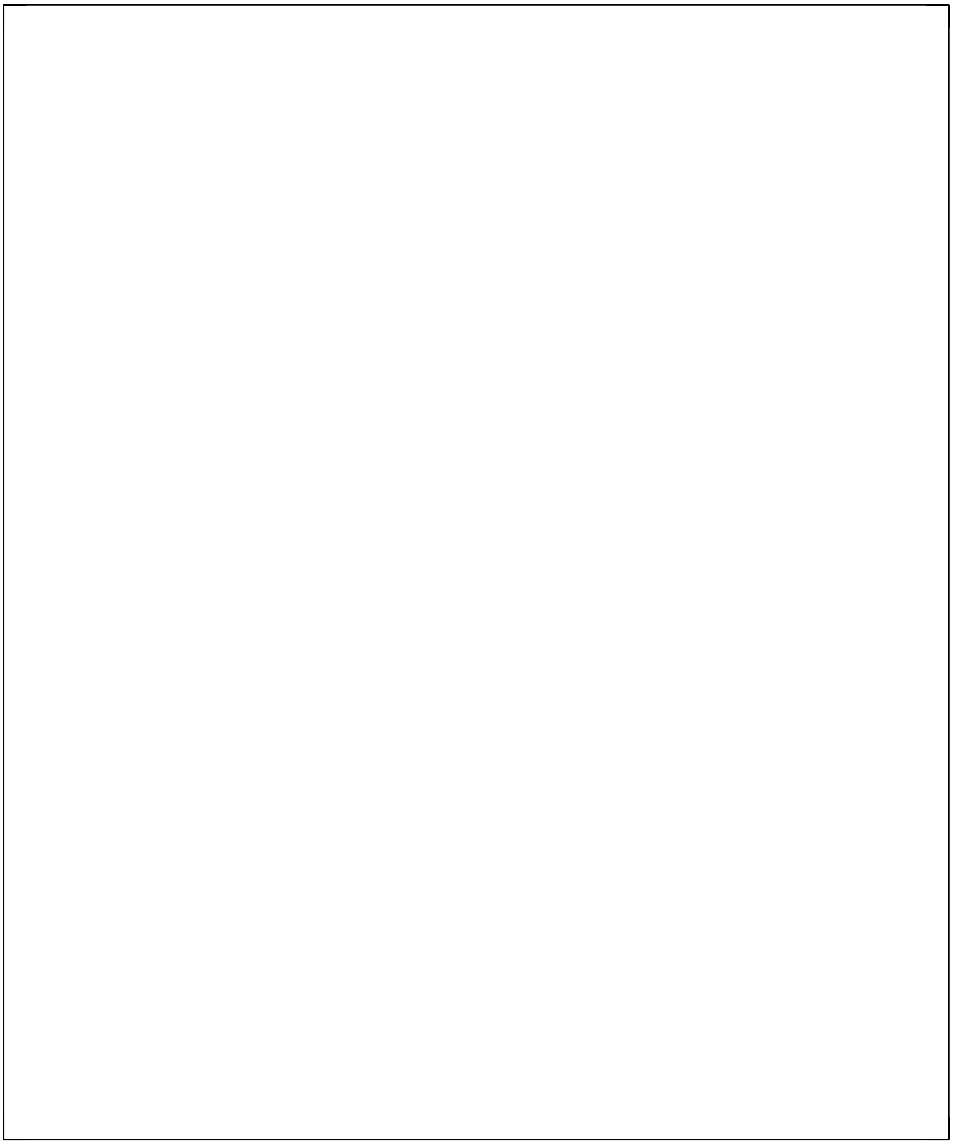

Figure 2.18: Logic for the master trigger.

a manual control implemented to freeze out the complete experiment if needed. Notice that the strobe pulse which controls the ccd integration time is also the same signal as the photocathode gate which is equivalent of turning on and off the image area of the ccd at the same time with the image intensifiers. The fast clear signal is produced by the RF signal for the elastic detectors (RF(O)) with a delay of 200 ns to make sure that in case there is a master trigger there is enough time to veto the fast clear. The fast clear is slaved to the signal of the photocathode gate. When the image intensifiers are on, fast clears are allowed to be sent to the ccd cameras, once the image intensifiers are turned off, having the strobe pulse off, there is no need to clear the ccd cameras. Also we know that sending clears during readout of the cameras produces interference with the readout register. The gate to turn off the image intensifiers is very fast (about 300 ns) but the gate to turn them on is very slow (about 5 μs). A precaution is needed for the strobe pulse, once a strobe pulse is sent to the cameras to start integration time it is necessary to make sure that the strobe pulse is at least 2 ms wide. This is to give enough time to the camera to resynchronize its internal clocks.

We do not read out the ccd cameras if no $O * O$ trigger is formed. Then for inelastic triggers there is not need to include the extra dead times produced by the camera readout and therefore the rate at which we can take inelastic data is much faster which is about 300 HZ compared to 50 HZ for the elastic data that is limited by the ccd readout.

The gating in the experiment is produced by vetoing the RF pulse needed in the coincidence units to produce each of the five triggers mentioned above. We have two different units to be vetoed, one is the unit that gives the RF for inelastic events

and the other is the one that gives the RF for elastic events. Also we delay the RF signal for inelastic and elastic events differently, this is because the difference in timing between the inelastic counters which are closer to the interaction point compared to the elastic detectors.

We can summarize the vetos for elastic and inelastic triggers in the following way ("+" is used for a logic "OR"):

$$\text{Inelastic triggers veto} = \text{computer busy} + \text{bin gate} + \text{master trigger busy} \quad (2.2)$$

$$\begin{aligned} \text{elastic trigger veto} \;=\; & \text{computer busy} + \text{computer busy addition} + \text{bin gate} \\ & + \text{vertical synch} + \text{VDAS busy} \\ & + \text{VDAS busy addition} + \text{master trigger busy} \end{aligned} \quad (2.3)$$

$$\text{bin gate} = \text{MR gate} + \text{MR gate addition} + \text{flying wire signal} + \text{run switch} \quad (2.4)$$

The VDAS busy addition is to avoid any trigger to arrive during the first 2 ms of the starting of the strobe pulse. The Main Ring gate addition is to avoid any triggers while the image intensifiers are still turning on because the detector will not be at full gain yet. The computer busy addition is relevant when the ccd cameras are operated in synchronous mode and it is to guarantee that one fast clear is sent to the ccd cameras before a master trigger is produced. The vertical synch is included in the vetos because we do not want an event produced while data is being transferred from the image area to the memory area of the ccd.

Finally, after counting number of elastic and number of inelastic events they have to be normalized to the same live time. We had one clock for the inelastic triggers live time (GCLK) and one clock for the elastic triggers live time (GCLK(O))

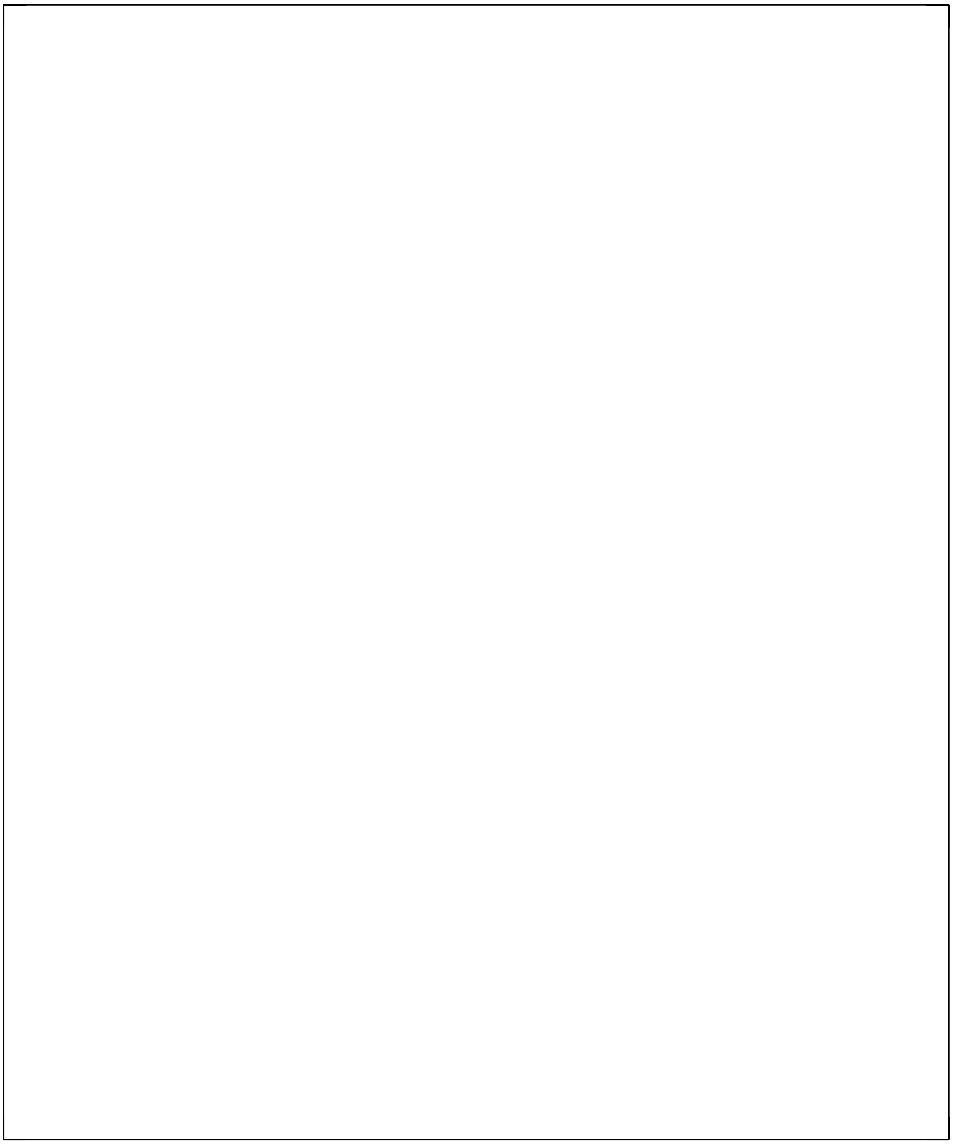

Figure 2.19: Logic for the experiment gating.

(see Figure 2.20). At the end in the analysis we normalize elastic and inelastic events to a common clock. The ratio of the clocks GCLK(O) to GCLK was different from run to run because it was dependent on the input rates to the DAQ system and the operating rate of the DAQ system which includes event buffer building and tape writing. The variable size of the VDAS buffers was the main source to have variable live time ratios (GCLK(O)/GCLK) from run to run depending on the run conditions.

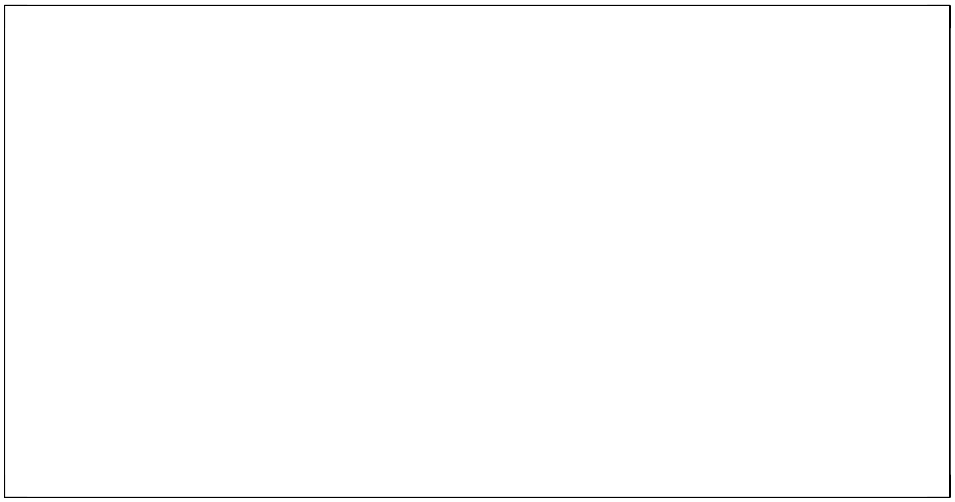

Figure 2.20: Gated clocks for inelastic and elastic triggers.

2.8 Physics Runs

Our data was obtained during a period of 5 days in which 4 different stores were injected in the Tevatron ring. The first three stores with 6 proton and 6 antiproton

bunches colliding. The last one with one proton and one antiproton bunch missing such that only 4 bunch-bunch interactions were produced . Two stores lasted about 24 hours and other two lasted about 17 hours. Just after injection in the Tevatron, the initial proton and antiproton bunch intensities were about 65 x 10^9 particles/bunch. We had to scrape each proton and antiproton beam to be able to locate vertically our detectors as close as possible to the beam axis. After scraping was complete the proton and antiproton bunch intensities were reduced to values below 6x10^9 particles/bunch. Table 2.3 shows the luminosities, bunch intensities and emittances at which we started taking data once the scraping in each store was completed. In the first store we took data before the final scraping, so two entries appear in Table 2.3. We placed our detectors at different vertical positions during each store, the data taken at the same pot position in the same store is what we call one of our runs.

Table 2.3: Initial Luminosities and intensities for each of our data stores.

store #	initial luminosity $(*10^{27} cm^{-2} sec^{-1})$	$\frac{protons}{bunch}$ $(*10^9)$	$\frac{antiprotons}{bunch}$ $(*10^9)$	$emittance_P$ π(mm-mrad)	$emittance_{\overline{P}}$ π(mm-mrad)
5865-I	9.6	18.4	15.4	3.2	4.2
5865-II	1.3	6.7	5.3	2.8	3.3
5866	1.6	6.8	5.5	2.8	2.8
5867	0.5	4.1	2.8	2.0	2.1
5868	6.1	16.5	13.5	3.3	4.6

Table 2.4 shows the master trigger used in each run and the distance between the upper and lower detector at which we took data (ΔH_{12} and ΔH_{34}). Table 2.5 shows the number of elastic and inelastic triggers taken in each run with their live times (GCLK(O) and GCLK) and a measurement of LR accidentals using the $L_{21}R$ signal, also the values of the luminosity monitor before and after subtracting

the accidental background is shown (M, $M - M'$).

Table 2.4: Master trigger, distance between upper and lower detectors and $|t|$ range for our physics runs.

run #	master trigger	ΔH_{12} (mm)	ΔH_{34} (mm)	$\|t\|$ range $(GeV/c)^2$
1	OO+LR/10	16.67	15.46	0.00875< $\|t\|$ <0.0361
2	OO+LR/10	6.40	6.17	0.00130< $\|t\|$ <0.0192
3	OO+LR/10	5.54	5.76	0.00097< $\|t\|$ <0.0180
4	OO+LR/10	5.53	5.76	0.00096< $\|t\|$ <0.0180
5	OO+LR/10	5.89	6.30	0.00109< $\|t\|$ <0.0185
6	OO+LR/10	5.89	6.28	0.00109< $\|t\|$ <0.0185
7	OO+LR/15	5.23	5.40	0.00086< $\|t\|$ <0.0176
8	OO+LR/5	5.18	5.54	0.00085< $\|t\|$ <0.0176
9	OO+LR/5	5.39	5.54	0.00092< $\|t\|$ <0.0178
10	OO+$\frac{LR}{40}+\frac{L}{4}+\frac{R}{4}+\frac{C}{400}$	16.68	15.31	0.00876< $\|t\|$ <0.0363

Table 2.5: Values of GCLK, GCLK(O), luminosity monitor, number of LR prescaled events, expected % of accidental coincidences in the LR trigger, and number of $O * O$ triggers.

run #	GCLK (s)	GCLK(O) (s)	M-M1	M	LRpr sclrs	L21R/LR	OOpr sclrs
1	320	349	12582	12877	8758	0.02885	114042
2	1861	1457	13330	13532	9565	0.03168	151816
3	1968	1599	10950	11124	8033	0.05465	146382
4	8317	6734	35246	35912	27296	0.15022	357980
5	9820	8109	54644	56498	37487	0.06713	449189
6	5190	4560	21735	22559	15148	0.07591	279645
7	1188	1046	3277	3335	4914	0.15907	49990
8	14084	12158	25187	25834	37197	0.10946	746339
9	8181	7461	8903	9222	11127	0.12291	199222
10	3628	3345	67003	68416	49853	0.11767	53761

CHAPTER 3

Experimental Methods

We describe here the experimental methods that can be used to measure the total cross section for $P\overline{P}$ interactions. At the end we describe the analysis method we follow.

3.1 Luminosity Dependent Method

One measures $\frac{dN_n}{dt}$ for $P\overline{P}$ nuclear elastic scattering events in certain $|t|$ interval and then makes the extrapolation to $|t| = 0$. $\frac{dN}{dt}$ is proportional to $\frac{d\sigma_n}{dt}$ where the proportionality constant is the integrated Luminosity L ($L = \int_0^t \mathcal{L} dt$, $\mathcal{L}$ being the instantaneous luminosity), then one can write:

$$\left(\frac{dN_n}{dt}\right)_{t=0} = L\left(\frac{d\sigma_n}{dt}\right)_{t=0} \tag{3.1}$$

from equation 1.18 :

$$\left(\frac{d\sigma_n}{dt}\right)_{t=0} = \frac{(1+\rho^2)\sigma_T^2}{16\pi(\hbar c)^2} \tag{3.2}$$

One can then obtain σ_T as

$$\sigma_T^2 = \frac{1}{L}\frac{16\pi(\hbar c)^2}{1+\rho^2}\left(\frac{dN_n}{dt}\right)_{t=0} \tag{3.3}$$

$\frac{dN_n}{dt}$ is measured in a $|t|$ interval where interference and coulomb contributions to the number of $P\overline{P}$ scattered events are very small. A previous measurement of ρ at the same energy is needed to fully determine σ_T, however since measurements from lower energy have shown that the ρ value is small ($\rho < 0.15$). Then the coupling between ρ and σ_T in equation 3.3 is very weak. The precision of the luminosity dependent method is limited by the uncertainty in the integrated luminosity which for the Tevatron collider is about $\pm 15\%$. Since σ_T goes as $1/\sqrt{L}$ then the uncertainty in the total cross section due to the uncertainty in the luminosity is 7 %. The first measurement of the total cross section at the Tevatron was performed with this method (see reference [1]).

3.2 Luminosity Independent Method

If one measures both the total number of inelastic and total number of elastic events then the total cross section can be written as

$$\sigma_T = \frac{N_T}{L} = \frac{N_{el} + N_{in}}{L} \tag{3.4}$$

If one divides equation 3.3 by equation 3.4 one obtains the following equation that does not contain the integrated luminosity:

$$\sigma_T = \frac{16\pi(\hbar c)^2}{1+\rho^2}\left(\frac{dN_n}{dt}\right)_{t=0}\frac{1.0}{N_{el}+N_{in}} \tag{3.5}$$

The number of elastic events can be obtained by integrating $\frac{dN_n}{dt}$:

$$\begin{aligned} N_{el} &= \int_0^\infty \left(\frac{dN_n}{dt}\right)_{t=0} e^{-B|t|} d|t| \\ &= \frac{1}{B}\left(\frac{dN_n}{dt}\right)_{t=0} \end{aligned} \tag{3.6}$$

Then to measure the total cross section one has to make the extrapolation of $\frac{dN_n}{dt}$ to $|t| = 0$, measure the B value and also measure the number of inelastic events. Here we also have to obtain the value of ρ from another source.

3.3 Coulomb Normalization

The two previous methods only use events produced by nuclear scattering. Any coulomb or nuclear-coulomb interference contribution to the number of events has to be subtracted before making the extrapolation to $|t| = 0$. If data is taken at very small scattering angles such that coulomb scattering becomes the main contributor to the $\frac{dN}{dt}$ distribution for some of the low $|t|$ bins then one can just fit the function given by equation 1.18 and fit the 4 parameters: σ_T, B, ρ and L. This method is called coulomb normalization because the differential cross section for coulomb scattering is known. The coulomb data are determining more accurately the normalization L. Coulomb scattering at higher energies requires detection of very small scattering angles. At $\sqrt{s}$=1800 GeV coulomb scattering becomes dominant for angles smaller that 30 μm.

3.4 Combined Method

From equation 3.6 the number of elastic events can be written as

$$\begin{aligned} N_{el} &= \frac{L}{B}\left(\frac{d\sigma_n}{dt}\right)_{t=0} \\ &= \frac{L}{B}\frac{\sigma_T^2(1+\rho^2)}{16\pi(\hbar c)^2} \end{aligned} \tag{3.7}$$

substituting equation 3.7 into 3.4 one can write:

$$\frac{dN_n}{dt} = \frac{N_{in}}{1-\frac{\sigma_T(1+\rho^2)}{16\pi B(\hbar c)^2}}\frac{\sigma_T(1+\rho^2)}{16\pi(\hbar c)^2}e^{-B|t|} \tag{3.8}$$

$$\frac{dN_c}{dt} = \frac{N_{in}}{1-\frac{\sigma_T(1+\rho^2)}{16\pi B(\hbar c)^2}} \frac{4\pi\alpha^2(\hbar c)^2 G^4(t)}{\sigma_T |t|^2} \tag{3.9}$$

$$\frac{dN_{nc}}{dt} = \frac{N_{in}}{1-\frac{\sigma_T(1+\rho^2)}{16\pi B(\hbar c)^2}} \frac{\alpha(\rho-\alpha\phi(t))G^2(t)}{|t|} e^{-\frac{B|t|}{2}} \tag{3.10}$$

If we measure in an independent way N_{in} then we just make a three parameter fit to $\frac{dN}{dt}$. This method is very useful when data is taken for $|t|$ values greater than the $|t|$ value where coulomb and nuclear scattering have the same contributions to the total number of events (see [14]).

3.5 Our Analysis Method

We use the luminosity independent method to measure the total cross section as described by equation 3.5. The method to obtain the value of $\frac{dN_{el}}{dt}\Big|_{t=0}$ is explained in section 4.

The total number of inelastic events is determined by using the ring counters that we placed in the straight section around the interaction point. The inelastic events hitting our ring counters can be classified as follows:

1. Events hitting at least one ring counter at each side of the interaction point which we call double arm events.

2. Events that hit one or more ring counters at one side but do not hit any ring counter in the opposite side of the interaction point. We call this second class of events single arm events.

The double arm events are mostly non single diffractive events with a small contribution from single diffractive events that have one or more backward decay particles. The fraction of single diffractive events with this characteristic should

be rather small since it will be only possible for the decays of very high mass final states. We quote the estimation made by E710 (see ref [2]) of 5±5 % for this type of events.

The single arm events are mostly beam-gas scattering events (about 94%, see reference [2]). If one subtracts the high background level, the remaining events are single diffractive events with a contribution from non single diffractive events that were not recorded with the double arm trigger. Since three measurements of the cross section for diffractive events have been performed at the same energy ([2], [3], [4]) and they agree within the errors we can use the world average for the single diffractive events as an alternative to the very high single arm background subtraction used in E710. In the method used here we just multiply the known single diffractive cross section by the integrated luminosity to obtain the number of single diffractive events and then just measure the number of nondiffractive events.

If we call LR_{ob} the number of double arm events measured from our ring counters and LR_{nd} the number of non single diffractive events contributing to LR_{ob} then we can write

$$LR_{ob} = LR_{nd} + 0.05 * (2\sigma_{sd} * L) \tag{3.11}$$

where L is the integrated luminosity. The quantity $2 * \sigma_{sd}$ is the proton and antiproton diffractive dissociation.

The number of inelastic events can be written as the sum of non single diffractive and single diffractive events:

$$N_{in} = \frac{LR_{nd}}{f} + 2\sigma_{sd} * L \tag{3.12}$$

where f is the fraction of the total number of non single diffractive events recorded

by the double arm trigger. We also define

$$\mu = \frac{2\sigma_{sd}}{\sigma_{nd}} = \frac{2\sigma_{sd}}{\sigma_{in} - 2\sigma_{sd}} \tag{3.13}$$

with σ_{in} being the inelastic cross section and σ_{nd} being the cross section for all non single diffractive events. equations 3.12 and 3.11 can be rewritten as:

$$N_{in} = \frac{LR_{nd}}{f}(1+\mu) \tag{3.14}$$

$$LR_{ob} = LR_{nd}(1 + 0.05 * \frac{\mu}{f}) \tag{3.15}$$

Combining equations 3.14 and 3.15 we obtain:

$$N_{in} = \frac{LR_{ob}}{f}\left(\frac{1+\mu}{1+0.05*\frac{\mu}{f}}\right) \tag{3.16}$$

We also know the following relations:

$$\sigma_T = \frac{16\pi(\hbar c)^2 B}{1+\rho^2}\frac{N_{el}}{N_{el}+N_{in}} \tag{3.17}$$

$$\sigma_{el} = \sigma_T\left(\frac{N_{el}}{N_{el}+N_{in}}\right) \tag{3.18}$$

$$\sigma_T = \sigma_{in} + \sigma_{el} \tag{3.19}$$

The measurements we can make are:

1. measure the number of elastics : $N_{el} = \frac{1}{B}\frac{dN}{dt}\Big|_{t=0}$
2. measure the value of LR_{ob}.
3. estimate the factor f (our acceptance for non single diffractive events).

The values we assume are known are :

1. fix $2\sigma_{sd}$ to the world average ($2\sigma_{sd}$=9.452 ±0.419 mb , references [2], [3], [4]).

2. fix the B value to the world average (B=16.99±0.22 $(GeV/c)^{-2}$).

3. Similar to experiments UA4([17]), E710 ([2]) and CDF([13]) fix ρ to ρ=0.145 which is the extrapolation from lower energies (both UA4/2 and E710 measurements of ρ agree with this value, [8], [14]).

The uncertainties in the values we fix are taken as part of the systematic errors in our measurement.

Equations 3.16, 3.17, 3.18 and 3.19 with the measurements described above constitute a set of four simultaneous equations with 4 unknowns: σ_T, σ_{in}, σ_{el} and N_{in}. Because the equations are non linear we can outline the following iterative procedure for solving them:

1. give an initial value for σ_{in} as a first guess

2. evaluate N_{inel} from equation 3.16

3. obtain σ_T from equation 3.17

4. obtain σ_{el} from equation 3.18

5. get a new value of σ_{in} from 3.19

6. goto 2) and repeat cycle until convergence.

CHAPTER 4

Elastic Data Analysis

The goal of this analysis is to extract the optical point, $\frac{dN_{el}}{dt}\Big|_{t=0}$ (nuclear part), from our data.

To count the number of elastic events we first apply TDC and ADC cuts in our trigger counters to select only events consistent with real particles traversing our detectors (Sections 4.4.2, 4.4.4). Once we have identified a possible particle with our trigger counters we scan our ccds to obtain the ccd coordinates of the fibers hit by the passing particle; we determine the hit coordinates by using the center of gravity of the hit pixels and then we convert these to positions in real space (Section 4.1, 4.2,4.3). Because the coordinates for the scattered proton and the scattered antiproton have to be complimentary with respect to the interaction point, after taking into account smearing effects caused by the beam sizes, we can apply collinearity requirements to the real space X and Y coordinates of the hits in the two corresponding detectors (or what we call diagonal cuts in the XX and YY scatter plots, Section 4.4.5). The presence of accelerator magnets between the interaction point and our detectors requires a good knowledge of the transport matrix elements in order to obtain the correct scattering angle from the X and Y

coordinates (Section 4.5). To find the position of our detectors with respect to the beam axis we can use random halo tracks. We use the fact that the Y distributions of halo particles are the same above and below the beam (Section 4.9.2). There are extra advantages in our analysis to integrate over the X coordinate and plot elastic events as a function of Y; we have an extra background estimation procedure that requires integration over X (Section 4.8.1); Also, integrating over X reduces the effect of coulomb and interference terms on the elastics distribution. We have to subtract the coulomb and interference terms from our data sample since we are interested here only in elastic events produced by nuclear scattering (Section 4.10). Other way we estimate the background is by fitting the shape of the events outside the YY diagonal plot and make an extrapolation to inside the diagonal (4.8.3). We also make a comparison of the Y background shape as given by the off XX diagonal events to the shape obtained from background triggers that were part of the master trigger (Section 4.8.2). After subtracting background and coulomb and nuclear-coulomb interference contributions to the number of events, we apply corrections due to geometrical losses (Section 4.7) and also corrections due to hardware and software efficiencies (Section 4.6). Finally we make the extrapolation to $|t|$=0 and average the intercepts obtained from the two defining detectors. The average of the intercepts washes out the systematic uncertainties of the beam position in the vertical axis (Section 4.11).

4.1 Cluster Identification

Figure 4.1 shows two elastic candidate events as they were recorded on one of the ccds. In each ccd frame are observed the cluster produced by the real particle that hit the detector, some noisy pixels caused by ccd dark current, and some small

clusters caused by image intensifier noise.

Most of the effect caused by ccd dark current is eliminated with our hardware pixel intensity threshold cut. The remaining dark current pixels that survived the threshold cut always have very low intensity and they are scattered around the ccd region that accumulates most of the dark current (the bottom part of the ccd). Therefore, the probability of finding three or more of these pixels clustered together is very small.

Image intensifier noise is the result of positive ions produced at the microchannel plate that get accelerated back to hit the photocathode producing noise electrons that then get multiplied at the microchannel plate; the number of these electrons depends on the image intensifier gain and the number of photons being intensified. Since we ran our image intensifiers at very high gain, to guarantee very good efficiency, we ended up having image intensifier noise producing clusters containing only a few pixels, which have lower intensities than real particles.

Clusters produced by real particles hitting the detector contained many pixels, these were of high intensity and had different topologies. The experiment was originally designed to have at least 3 scintillating fibers hit by the passage of a particle through the detector. To achieve this, fibers in the bundle were tilted vertically from one end to the other by a few microradians. Because some detectors might have some additional rotation during installation, such detectors would have more fibers being hit. Also, because the length of the scintillating bundle was $\approx$10% of the nuclear interaction length, we could have interactions of the particle in the detector. Both of these factors gave, as a result, cluster topologies which differ from one detector to another since detector tilting angles, thresholds and gains

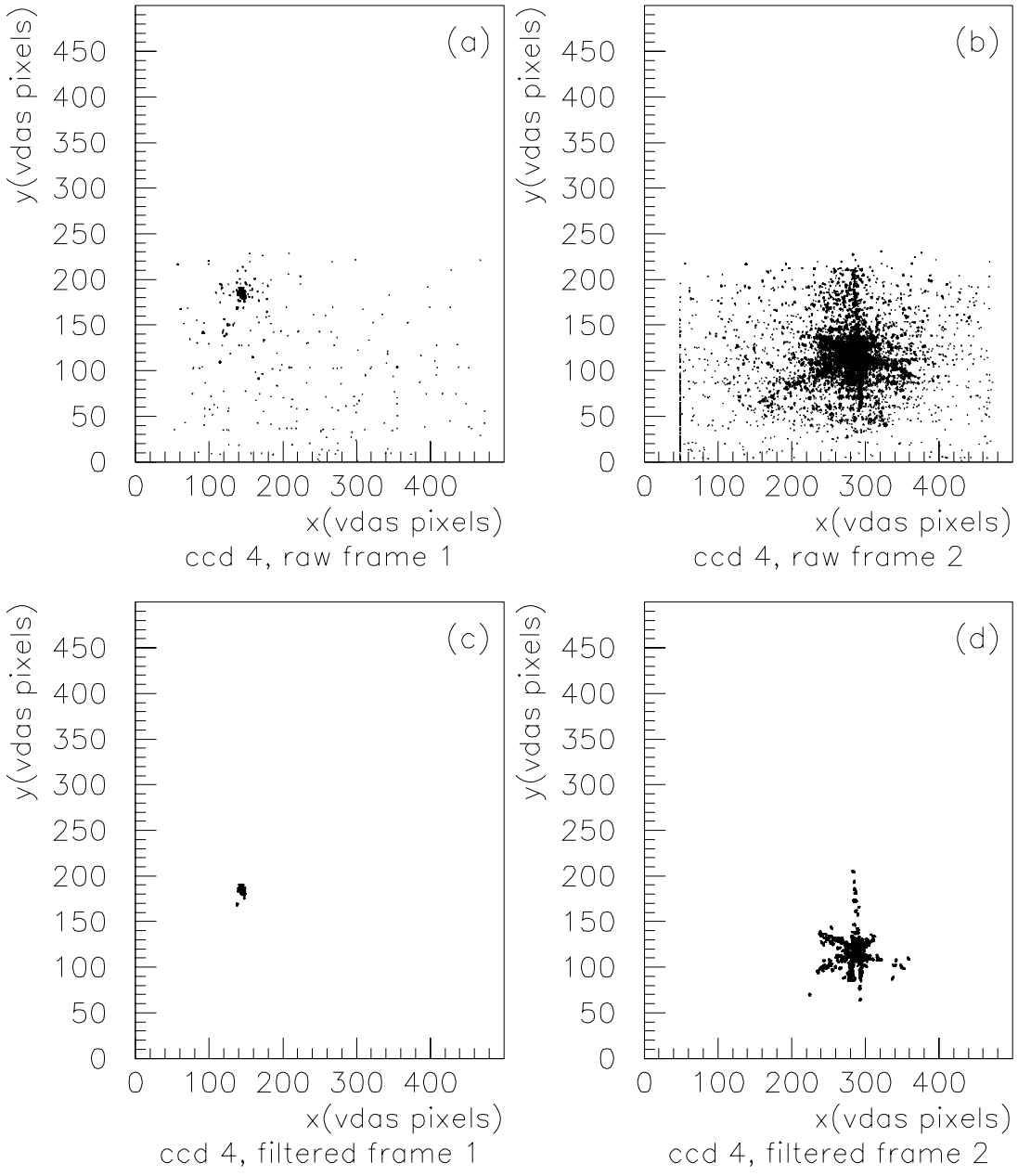

Figure 4.1: a) ccd frame for a particle not interacting with the scintillating fiber bundle. b) ccd frame for a particle interacting with the bundle. c) software filtered frame for event in a). d) software filtered frame for event in b).

were different. Figure 4.1a) shows a typical cluster produced by a particle that did not interact with the bundle and also shows (in Figure 4.1b) a cluster produced in the case of a nuclear interaction between the incident particle and an atomic nucleus in the bundle.

We used two methods to identify the cluster due to a real particle:
1) by number of hit pixels.
2) by putting a threshold on the sum of the intensities of the pixels belonging to the cluster. This sum is what we call cluster intensity.

The ccd was scanned searching for clusters that had 5 or more pixels above threshold, where the threshold was chosen to be greater than most of the dark current intensities. Pixels whose intensities are below the threshold are not considered in further analysis. Figures 4.1c) and 4.1d) also show the result of this filtering when applied to the 2 raw frames, Figures 4.1a) and 4.1b). If no cluster survived the 5 pixel cut then we declared the frame to be empty.
The cluster intensity cut was chosen by studying frames with only one cluster surviving the 5 pixel requirement and in which the scintillation trigger counters in the detector had a hit consistent with a minimum ionizing particle. Once we applied the cluster intensity cut to the whole data sample only 1 cluster survived in about 99 % of the events. The remaining 1% corresponded to multiple hits in the detector (see Section 4.4.6).

Once the cluster was identified following the above procedure, the coordinates of the hit were found by using the cluster center of gravity:

$$Xcg = \frac{\sum_{i=1}^{n} I_i * x_i}{\sum_{i=1}^{n} I_i}$$

$$Ycg = \frac{\sum_{i=1}^{n} I_i * y_i}{\sum_{i=1}^{n} I_i} \tag{4.1}$$

where x_i,y_i = pixel column and row numbers respectively

I_i = intensity of pixel i.

The size of each pixel, as explained in Section 4.2, is about 45 x 45 μm in real space.

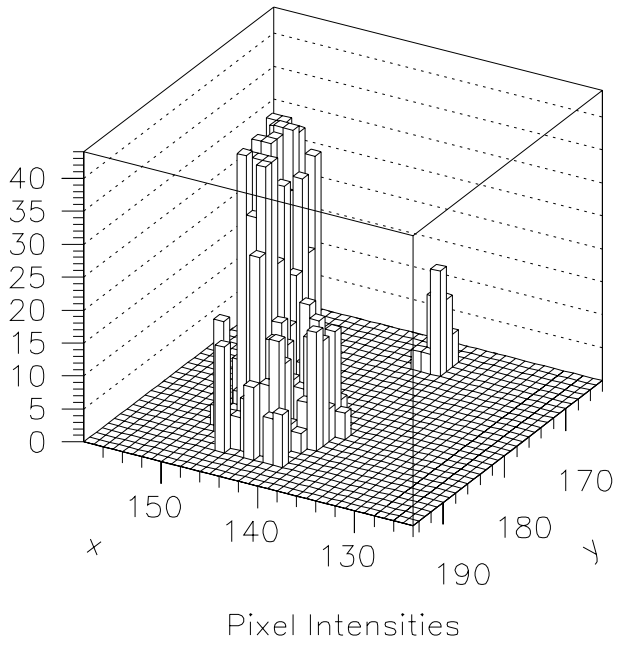

Figure 4.2: Pixel intensity for a real particle cluster compared to pixel intensity for a noise cluster.

Because of the high gains we used in the image intensifiers and ccds, to guarantee high detector efficiency, the intensity of some pixels in the cluster saturated. Figure 4.2 shows the pixel intensities from the event of Figure 4.1c). It is observed that the peak of the cluster is cut off because of saturation of the ccd. The ccd

saturation along with the extra number of fibers hit due to tilting angles increased the uncertainty in the determination of the hit coordinates.

The uncertainty in the hit position is obtained as the square root of the weighted sum of the squares of the cluster pixel distances from the center of gravity:

$$\begin{aligned} \sigma^2_{Xcg} &= \frac{\sum_{i=1}^{n} I_i * (x_i - Xcg)^2}{\sum_{i=1}^{n} I_i} \\ \sigma^2_{Ycg} &= \frac{\sum_{i=1}^{n} I_i * (y_i - Ycg)^2}{\sum_{i=1}^{n} I_i} \end{aligned} \tag{4.2}$$

The σ_{Xcg} and σ_{Ycg} distributions for one of the detectors is shown in Figure 4.3. Nuclear interactions of particles in the detector usually ended up with larger uncertainties producing long tails in the hit uncertainty distributions.

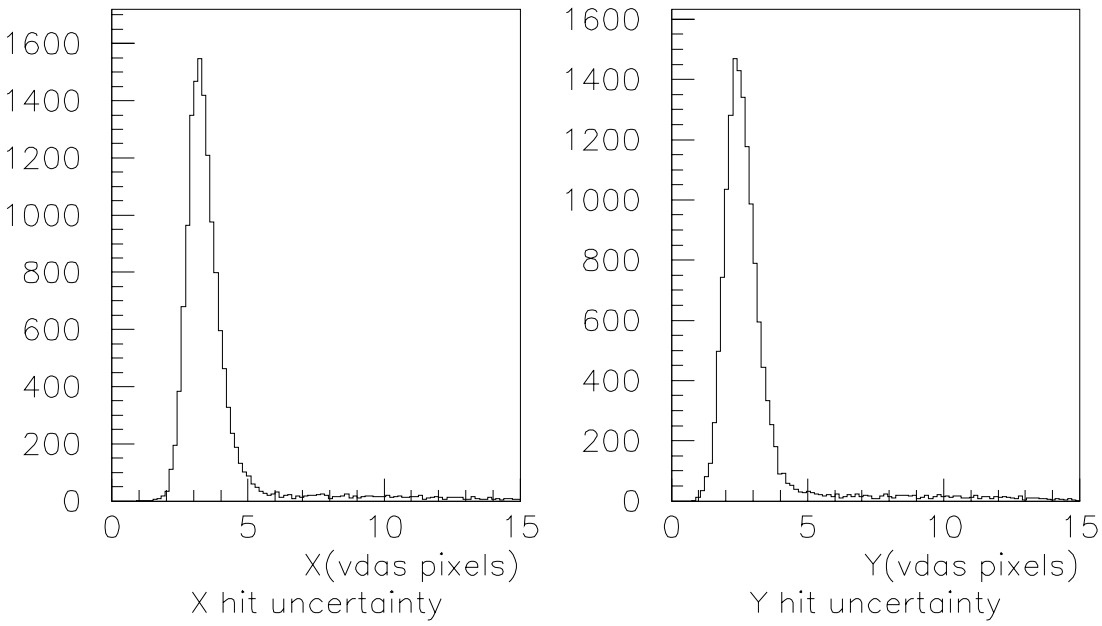

Figure 4.3: Uncertainties in cluster hit coordinates.

The X,Y uncertainty distributions peaked at about 3 vdas pixels ($\approx$ 130 μm)

for all detectors except the X distribution of detector 1 which peaked at about 5 vdas pixels ($\approx$ 230 μm); the X coordinate uncertainty in detector 1 was poorer because it had the largest tilting angle in the horizontal plane. Since we wanted to keep coordinate uncertainties smaller than the elastic scattering resolution due to finite beam size and divergence at the interaction region, we used an upper cut in the cluster uncertainty distributions. The upper cut was 7 vdas pixels for X and Y coordinates in all detectors except X coordinate of detector 1 where we used a cut of 10 vdas pixels; the size of a vdas pixel is about 45 μm. The precise method for conversion to mm is explained in Section 4.2.

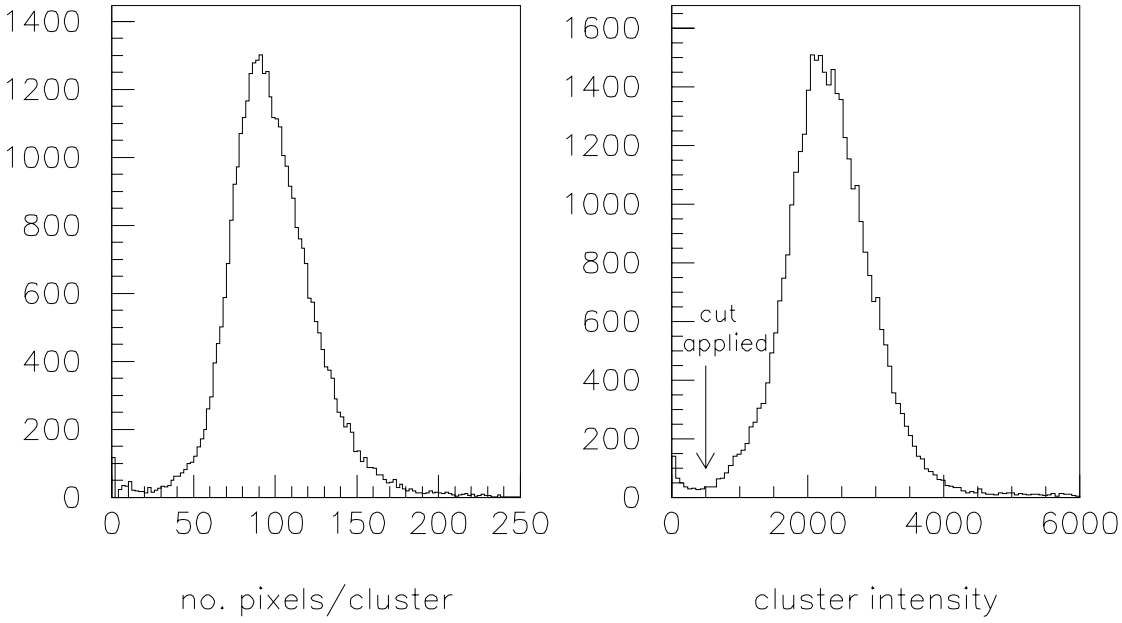

Figure 4.4: Distributions of number of pixels/cluster and cluster intensity after hit uncertainty cuts.

Figure 4.4 shows the distribution of number of pixels/cluster and the cluster

intensity distribution after applying the hit uncertainty cuts. Most of the nuclear interaction clusters, which contain a larger number of pixels and higher cluster intensity, get cut off by the hit uncertainty cut. Also shown in Figure 4.4 is the low threshold cut in cluster intensity that we applied to remove events (noise, etc.) not caused by a real particle.

4.2 Distortion Corrections and Coordinate Calibrations

A description of the study of distortions of each piece of the detector was given in Section 2.5.1. Here we are going to describe the distortion corrections for the complete apparatus.

Before glueing the toe counter to the scintillating bundle, 4 horizontal lines and 7 vertical lines were accurately scribed on the aluminized toe face, forming a reticle pattern that we called the toe reticle. The width of each line was 100 μm and the separation between lines was 1.5 mm, the first horizontal line was scribed 2.5 mm from the bottom edge of the toe. At times when no beam particles were in the Tevatron, light was shined from a bright LED installed near the interface of the toe light pipe and toe photomultiplier. Some of the light from the toe reticle was picked up by the scintillating fibers of the bundle. The image intensifiers and ccds were turned on with the same gains as when running with beam. The LED intensity was adjusted so as to be able to see the reticle lines on the ccd and then many ccd frames for each detector were recorded on tape. As we described in Section 2.5.1, the two main sources for distortions were the scintillating bundle and the fiber glass light guide. Distortions in the image intensifiers, taper and ccd

were negligible.

We also took halo data (when electrostatic separators were on, i.e. no collisions at E0) triggering on each detector independently and having the detectors at about 10 mm from the beam. If we only accept events in which the toe counter fired and with a cluster consistent with a real particle, we can identify the edges of that counter by fitting an error function to the distribution of hits around each edge. Also, elastic data can be used for finding the edges of the toe counter; but since most of our dedicated running time was done with the detectors very close to the beam, most of the data was located near the bottom of the detector giving fewer hits on the upper edges of the toe counter. We can correct the ccd output for detector distortions and also calibrate the vdas pixel coordinates to mm by using the data from the LED reticle and the knowledge of the edges from the mapping of real particles.

Light produced by the LED reticle at the front face of the scintillating bundle can travel through a different path than light produced by particles going through the bundle. This is caused by either detector tilting angles or twisting and magnification or any other type of distortion in the fibers inside the bundle. Detector tilting angles produced some small shifts of the edges of the toe scintillator when they were mapped with particles as compared with the edges when the mapping was done with the LED reticle. We also observed, in detector 1, some fiber twisting that produced a rotation of the toe outlines as observed by either mapping method.

The initial step we followed for correcting distortions was to get the toe outlines

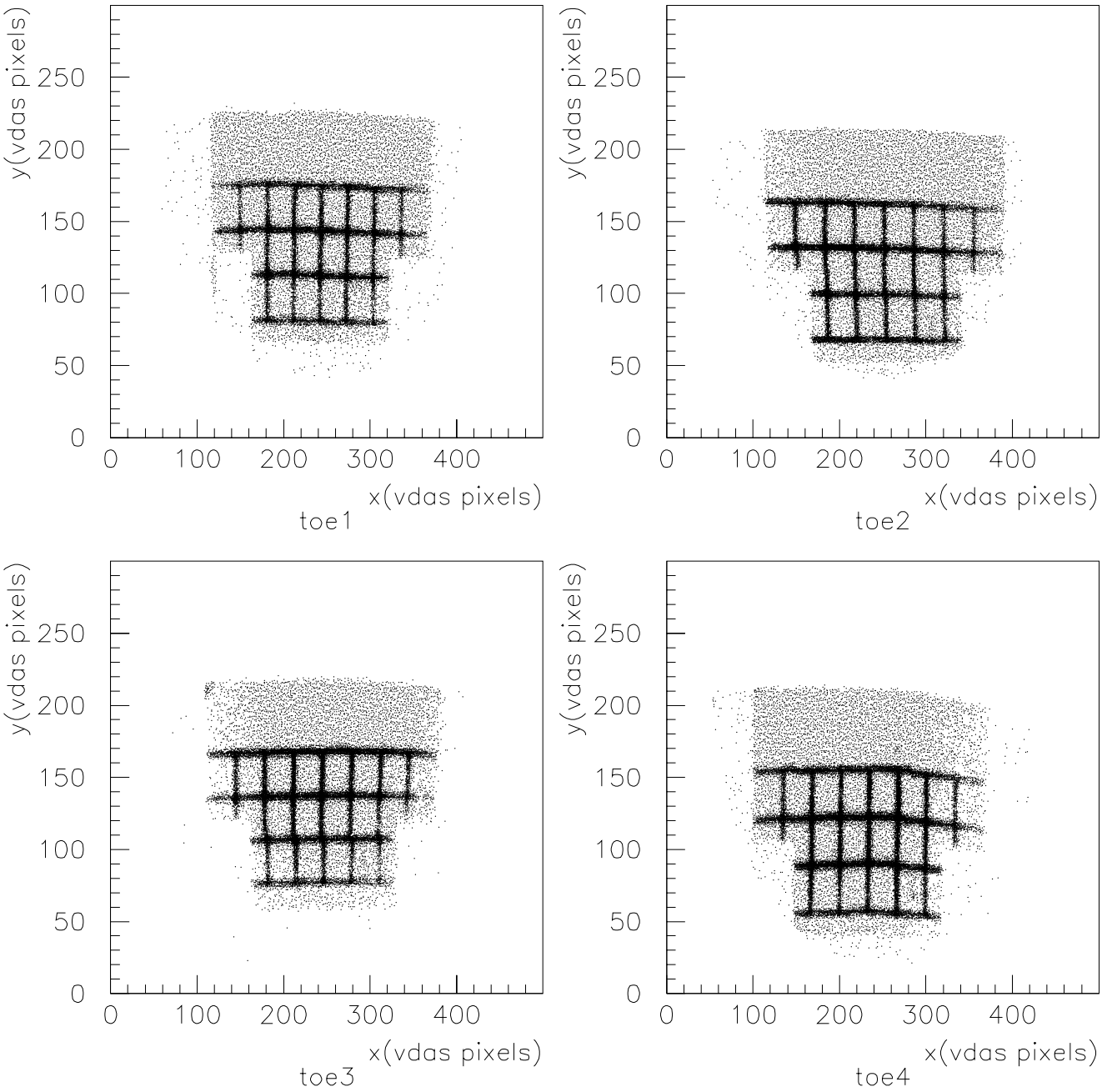

Figure 4.5: Optical distortions within the toe counter area.

as observed by the two methods to agree. To do this, we shifted the toe edges mapped with particles to overlap with the edges as predicted by the LED reticle. Some small demagnification ($\approx 3\%$) factors had to be used in detectors 1 and 4 to get a good agreement. Also a rotation correction of 2.3 degrees was needed for detector 1. No fiber twisting was observed in any of the other three detectors. This initial step can also be seen as just mapping the toe outline as predicted by real particles as if it were produced at the front face of the bundle where the toe reticle was placed. The overlap of the outlines from the two mappings is shown in Figure 4.5, the shadow area is what we get when mapping with particles, and the black solid lines is the toe reticle pattern observed on the ccd.

Once the two toe outlines from the two mapping procedures agreed, we corrected for distortions within the toe area. We found the position on the ccd of each crossing of the reticle lines. Then we measured the X, Y distances in vdas pixels between neighboring crossings and then determined the average X, Y distance between crossings. Table 4.1 shows the average distances found.

Table 4.1: Average distances in vdas pixels between neighbor reticle crossings. The corresponding distance in real space is 1.5 mm.

	$\langle \Delta X_{crossing} \rangle$ (vdas pixels)	$\langle \Delta Y_{crossing} \rangle$ (vdas pixels)
DET 1	31.0	31.0
DET 2	34.0	31.0
DET 3	33.0	30.0
DET 4	33.0	33.0

We then picked up one crossing point as a reference. The positions of all of the other reticle crossings with respect to our reference, if no distortions existed, can be calculated by using the average distances we found above. The difference

between the crossing position that we observe on the ccd compared to the case of no distortions is the correction that we have to apply. With the above procedure we ended up with a table of how much correction we had to apply for each crossing point. After studying the complete toe reticle lines as seen on the ccd we concluded that no major local distortion is observed between crossings and therefore we use a linear interpolation between the crossings. The correction that we have to apply to any point on the ccd is taken as the linear interpolation of the corrections that we have to apply to the 4 closest reticle crossings to that point.

In the first 2.5 mm from the beam side of the detector we do not have any reticle line. The only extra knowledge we can use for distortion corrections is the toe edge as it was mapped by particles and after overlapping the toe outline to the predicted outline from the led reticle. To get a better knowledge of the corrections to be made in the area near the beam side of the detector, we extrapolated the reticle vertical lines by fitting a straight line to them and finding the intercept of each line with the toe bottom edge. The intercepts found in this way were used as extra crossing points in determining the corrections.

Because the distance between reticle crossing lines in real space is 1.5 mm, the calibrations for the ccds could be determined. The average distance in vdas pixels, as we found above, has to be equal to 1.5 mm. We also used the edges of the toe counters to verify the coordinate calibrations.

4.3 Coordinates Determination

The coordinates of a hit in mm with respect to the Tevatron beam are defined as follows: positive Z is in the direction of the in-time particle in each detector, that is the pbar direction for detectors 1 and 2 and the proton direction for detectors 3 and 4. Y is defined to be always positive when moving away from the beam in the vertical direction (i.e. Y is positive up from the beam for detectors 1 and 3, and it is positive for detectors 2 and 4 when moving down from the beam). X satisfies the right hand rule.

The conversion from vdas cell coordinates to real space is given by (see Figure 4.6):

$$X_i = Xc_i + Xbeam_i$$

$$X_i = xcal_i * (xdc_i - xcg_i) + Xbeam_i \tag{4.3}$$

$$Y_i = Yb_i + Ybeam_i$$

$$Y_i = ycal_i * (ydb_i - ycg_i) + Ybeam_i \tag{4.4}$$

where

Xc_i = x hit coordinate from center of toe counter of detector i.

$xcal_i$ = mm/pixel conversion for x coordinate of detector i.

xdc_i = x coordinate of the center of the toe counter on ccd i.

xcg_i = x coordinate of center of gravity of the hit in detector i.

$Xbeam_i$ = x coordinate of the beam position measured from the center of of the toe of detector i.

Yb_i = y hit coordinate from bottom of toe counter of detector i.

$ycal_i$ = mm/pixel conversion for y coordinate of detector i.

ydb_i = y coordinate of the bottom edge of the toe counter on ccd i.

ycg_i = y coordinate of center of gravity of the hit in detector i.

$ybeam_i$ = y distance between the bottom edge of the toe counter and the beam center.

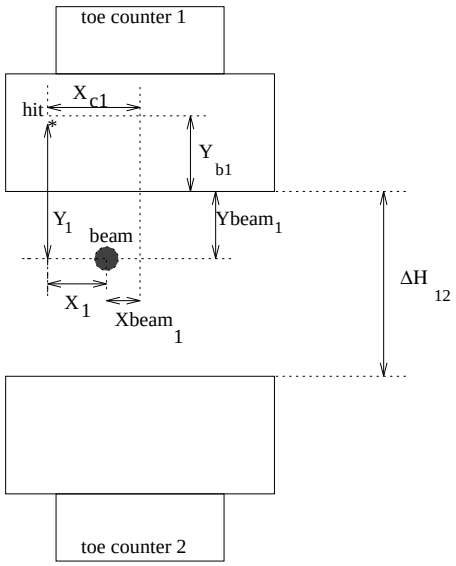

Figure 4.6: Hit coordinates definition.

The procedure to measure Xbeam and Ybeam is explained in Section 4.9.

The scattering angle as measured by detector i is:

$$\theta_i^2 = \frac{X_i^2}{Leffx_i^2} + \frac{Y_i^2}{Leffy_i^2} \tag{4.5}$$

$Leffx_i$ and $Leffy_i$ are the x and y effective distances between the interaction point and detector i which are described in Section 4.5 .

4.4 Elastic Event Selection

The procedure for deciding whether or not a particular event is a good elastic candidate is as follows:

1.) Prescaler requirement

2.) TDC cuts

3.) ADC cuts

4.) cluster cuts

5.) Diagonal cuts

6.) Multiple hits

4.4.1 Prescaler Requirement

Only events for which the OO prescaler incremented were used to search for an elastic event. As explained in Section 2.7, the OO trigger was the coincidence of any trigger counter in the two left detectors with any trigger counter in the two right detectors and in coincidence with the RF clock signal from the Tevatron control room; this later coincidence guaranteed that both particles came from an interaction at our collision point.

4.4.2 TDC Cuts

The time of flight distribution for one toe counter is shown in Figure 4.7. Because of the 70 ns resolving time of the coincidence of elastic counters and RF, we ended up accepting also events from the satellite bunches of the proton and antiproton circulating beams, which are 19 ns apart from the main bunch. The number of events on the satellite bunches that we observe in our time of flight distributions by the toe counter compared to the main bunch are about 1.1% for the early satellite and 2.0% for the late satellite on the pbar beam and 1.4% for the early satellite and 2.4% for the late satellite on the proton beam. In our analysis we only used

the interactions produced by the main bunches.

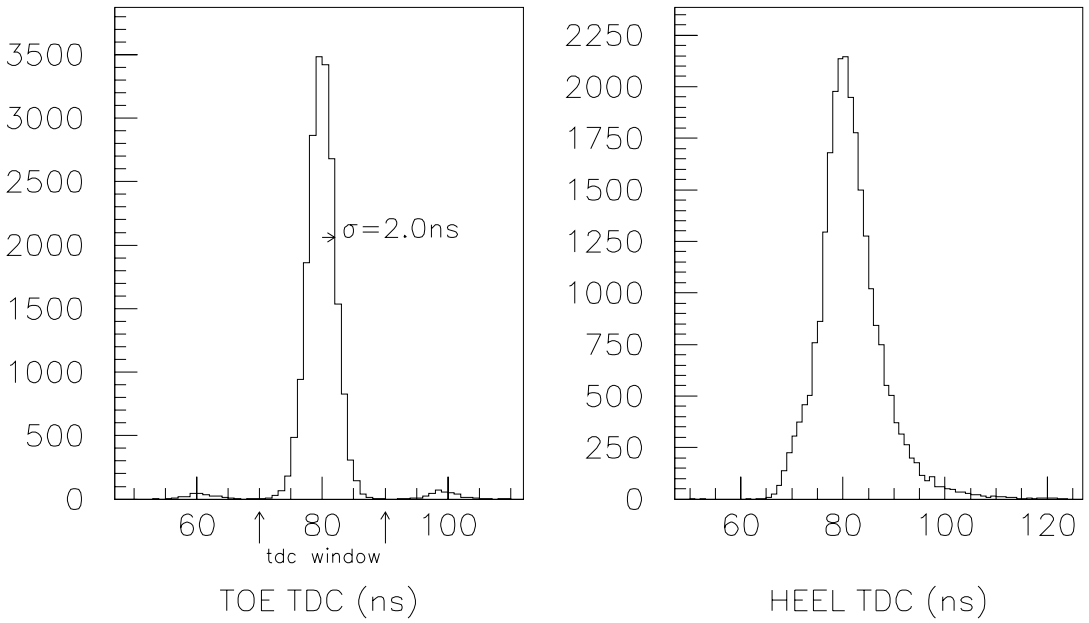

Figure 4.7: Time of flight distributions as measured by toe and heel counters.

The heel TDC does not have good time resolution (see figure 4.7) because its photomultiplier sees the light from the heel counter after it has been amplified by the image intensifiers. Because of the slow decay time of the phosphors of the image intensifiers (see Section 2.3.1), the TDC of the heel counter cannot discriminate the satellite bunches from the main bunch. We only used the heel counter to measure the efficiencies of hardware and software (see Section 4.6).

The TDC width of the main bunch we measured in the toe counter was 2.0 ns. This width comes from counter resolution and particle bunch size in the accelerator. We used a TDC window of ± 10 ns around the peak to avoid cutting out any event

from the main bunch (see Figure 4.7).

To have an elastic candidate event, either a coincidence of toe counters in detectors 1 and 4 was required or a coincidence of the toe counters in detectors 2 and 3, where toe counters TDC's had to be within the windows discussed above.

4.4.3 Cluster Cuts

As we already explained (Section 4.1) the cluster cuts we applied were :

1.) hit uncertainty cut

2.) cluster intensity cut

4.4.4 ADC Cuts

The ADC distributions for toe and heel counters before applying any cut and after applying cluster cuts and TDC cuts on the toe are shown in Figure 4.8. The high number of events overflowing the heel ADC is a consequence of the heel being located in the back of the detector. Nuclear interactions between the passing particle and the bundle or glass light guide can produce showers of particles that the heel will see, enhancing the light produced in the heel. Even in the case of a nuclear interaction produced by a particle hitting the detector outside the area covered by the heel, the heel can still be hit by a secondary particle produced in that nuclear interaction. Nuclear interactions produced in the scintillating bundle get rejected with the hit uncertainty cuts, so in our analysis the effect of nuclear interactions on the heel counter comes from nuclear interactions produced in the fiberglass light guide.

The lines of the toe reticle cover about 8% of the area of the toe counter. We

can expect to have cross talk between the scintillating bundle and the toe counter through this area. The amount of light cross-talked to the toe will be higher when nuclear interactions occur in the bundle. This is the reason that the number of events overflowing the toe ADC get reduced after applying the hit uncertainty cut which eliminates most of the nuclear interactions. The hit uncertainty cut also reduces the overflows on the heel counter. However the heel counter will still be seeing the nuclear interaction that occur in the glass light guide material that the particle has to travel through before reaching the heel counter. Figure 4.8 shows the ADC cut we applied to the toe counter. We only applied ADC cuts on the heel for efficiencies determination.

4.4.5 Diagonal Cuts

If a proton and a pbar scattered elastically we should measure the same scattering angle on both sides of the interaction point. Therefore if we plot y4 vs y1 (or y3 vs y2), which is the vertical hit coordinate of detector 4 versus the vertical hit coordinate of detector 1, for each event, we should see the elastic events within a band centered on a straight line whose slope is the ratio of the vertical effective distances for the two detectors. The width of the band gives us the resolution for measuring the hit coordinates which is dependent on the detector resolutions and on beam properties. Also if we make a scatter plot for the horizontal coordinates, the same type of correlation will be observed.

Figure 4.9 shows the scatter plots obtained when the detectors are located at two different positions from the beam and after applying TDC cuts, ADC cuts

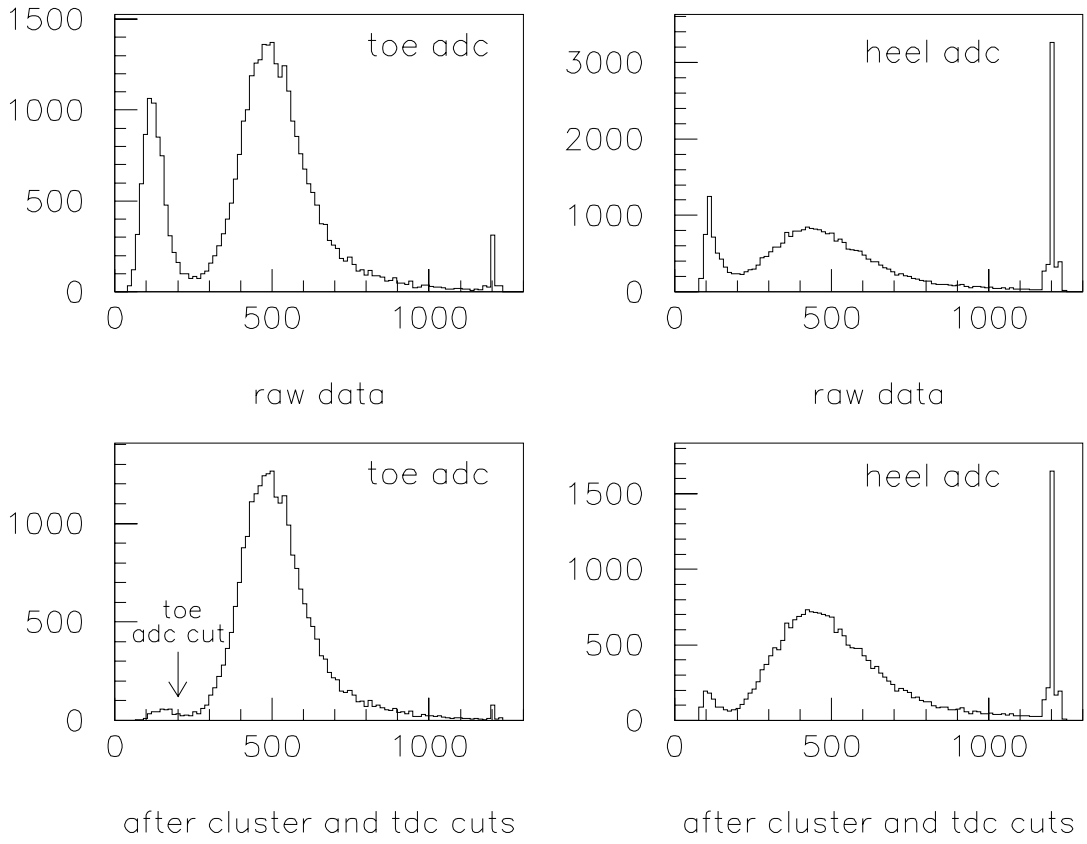

Figure 4.8: ADC distributions for toe and heel counters.

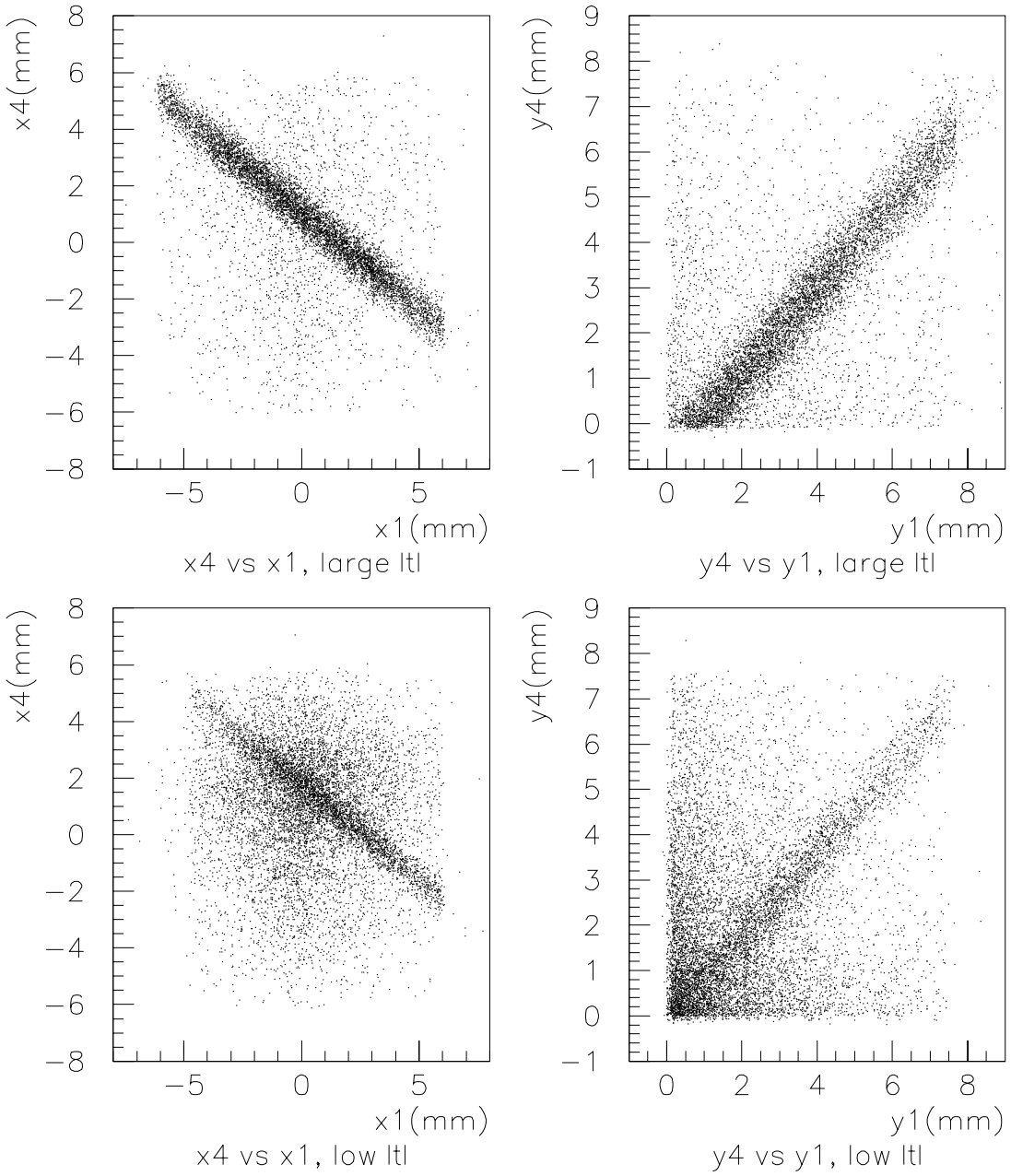

Figure 4.9: XX and YY correlations for elastic events with detectors at two different vertical positions.

and cluster cuts on detectors 1 and 4. The vertical hit coordinates in these plots are measured with respect to the bottom of the detectors. The horizontal hit coordinates are measured with respect to the center of the toe counter.
From Figure 4.9 one can observe the increase in background when the detectors get closer to the beam. In Section 4.8 we will describe the methods we used to estimate the background inside the elastic diagonal band.

We can cut around the band where elastics are concentrated to produce a cleaner sample. The way to determine the cut is by selecting a region of the detector with low background and fitting a gaussian function to the distributions:

$$\Delta\theta_{y14} = Yb1/Leffy1 - Yb4/Leffy4$$
$$\Delta\theta_{x14} = Xc1/Leffx1 - Xc4/Leffx4 \quad (4.6)$$

where $Yb1$, $Yb4$ are the vertical hit coordinates measured from the bottom of the toe counters for detectors 1 and 4 respectively. Xc1, Xc4 are the horizontal hit coordinates measured from the center of the toe counters. The cut we apply is $3*\sigma$ around the measured mean value to each of the two distributions $\Delta\theta_{y14}$ and $\Delta\theta_{x14}$ (these distributions are shown in Figure 4.10). Notice that we did not need to know the hit coordinates with respect to the beam since they do not affect the value of σ, they will only reflect in a shift of the mean value. The mean value value of the distribution is important for estimating the losses of events due to geometrical acceptance (see Section 4.7).

The same procedure is applied to the combination of detectors 2 and 3.

Tables 4.2 and 4.3 show the results of the gaussian fit to the elastic distributions, as defined in equation 4.6, for the 10 sets of data we took.

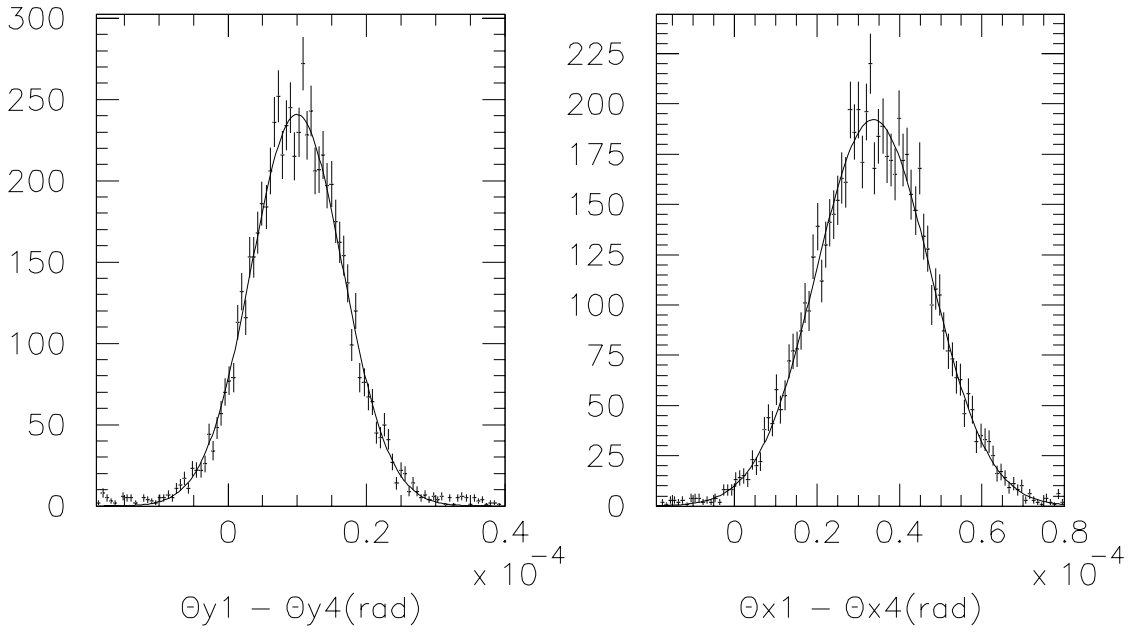

Figure 4.10: Collinearity distributions from equation 4.6.

Table 4.2: Width of elastic band from detectors 1-4.

set no.	σ_{xx14} (μrad)	$mean_{xx14}$ (μrad)	σ_{yy14} (μrad)	$mean_{yy14}$ (μrad)
1	12.5±0.5	21.8±0.7	5.5±0.2	-9.4±0.2
2	11.7±0.4	23.7±0.6	4.9±0.2	3.6±0.2
3	12.5±0.3	23.4±0.4	5.3±0.2	-3.7±0.2
4	13.4±0.3	23.1±0.3	6.1±0.2	-4.0±0.2
5	12.0±0.3	58.5±0.2	5.7±0.2	2.5±0.2
6	13.1±0.5	58.1±0.5	6.2±0.2	2.6±0.2
7	12.1±0.7	28.6±0.7	4.0±0.2	-0.3±0.2
8	12.8±0.4	29.4±0.4	4.4±0.1	0.4±0.2
9	13.7±0.5	30.7±0.5	5.3±0.2	0.1±0.2
10	13.9±0.3	33.2±0.2	6.3±0.1	9.4±0.1

Table 4.3: Width of elastic band from detectors 2-3.

set no.	σ_{xx23} (μrad)	$mean_{xx23}$ (μrad)	σ_{yy23} (μrad)	$mean_{yy23}$ (μrad)
1	12.4±0.4	17.1±0.4	5.5±0.2	1.5±0.2
2	11.1±0.5	18.4±0.6	4.9±0.2	-4.9±0.2
3	12.1±0.4	17.5±0.4	5.4±0.3	5.0±0.2
4	13.6±0.3	18.2±0.5	6.5±0.3	6.6±0.2
5	11.8±0.4	-17.6±0.3	5.7±0.2	2.9±0.2
6	13.2±0.4	-16.4±0.5	6.4±0.2	3.2±0.2
7	11.8±0.5	8.8±0.6	4.4±0.4	4.6±0.4
8	12.0±0.3	10.1±0.3	4.5±0.3	3.2±0.2
9	13.1±0.6	9.1±0.6	5.7±0.3	1.0±0.3
10	13.5±0.1	5.9±0.2	6.4±0.1	-20.4±0.1

4.4.6 Multiple Hits

The average detector rates after coincidence with RF timing were of the order of 1.5 KHz and the average rate for elastic events was of the order of 2 Hz for most of the runs we took with the detectors closer to the beam. Because these numbers are very small when compared to bunch crossing frequency (1.0/3.5μsec), the probability of having a good elastic candidate with two particles hitting one of the detectors is very low (about 1%). For this type of event two clusters above cluster intensity threshold were identified in one of the detectors by the cluster search algorithm. The coordinates of both clusters were compared to the coordinates of the hit in the conjugate detector that defined the elastic pair(1-4 or 2-3). The cluster whose coordinates were closer to the coordinates of the conjugate detector was selected as the best elastic candidate.

4.5 Effective Lengths

The effective lengths are defined in Appendix A as the transport matrix elements that correlate the scattering angle at the interaction point to the displacement from the beam observed at our detectors as if the particle had traveled in a straight line a distance equal to the effective length.

The values of effective lengths for detectors 1 and 2 are different from detectors 3 and 4 because the Tevatron lattice was not symmetric between the interaction point and our two detector locations (see Section 2.2). A good knowledge of these values is important for our measurements since their uncertainty will reflect as an uncertainty in the scattering angle. There are two ways to obtain the effective lengths:

1)The effective lengths can be calculated by using the accelerator lattice parameters in equation A.10. These are the values provided by the Tevatron staff (see Table 4.4).

Table 4.4: E811 Effective Lengths from Accelerator group.

	E811 effective lengths from Accelerator group
$Leffx_1$(m)	45.7
$Leffx_4$(m)	31.3
$\frac{Leffx_1}{Leffx_4}$	1.458
$Leffy_1$(m)	80.3
$Leffy_4$(m)	73.9
$\frac{Leffy_1}{Leffy_4}$	1.087

2) A previous experiment (E710) located at the same interaction point and with almost identical Tevatron lattice measured the effective lengths for the vertical axis

for the same two locations where we have our elastic detectors. The only difference between the two experiments was that a magnet located at the E13 point was run at a different current in the two experiments and therefore could affect the effective lengths for detectors 3 and 4. The measurement by experiment E710 was possible because that experiment had elastic detectors located at 4 different points in the Tevatron. Two of the locations were identical to our experiment, while the two extra pairs of elastic detectors were located in the straight section (no magnets) around E0. A measurement of the effective lengths was obtained by fitting the elastic tracks that went through the detectors in the straight section and the detectors after the magnets (see Reference [55] for a detailed description). The E710 measurements averaged 1 % agreement to the accelerator values calculated by the accelerator group (see Table 4.5).

Table 4.5: Measurements for Y effective lengths by experiment E710 compared to values obtained from accelerator group.

	E710	Accelerator group
$Leffx_1$(m)		45.6
$Leffx_4$(m)		30.0
$\frac{Leffx_1}{Leffx_4}$		1.52
$Leffy_1$(m)	80.4±1.0	80.6
$Leffy_4$(m)	76.5±1.0	75.1
$\frac{Leffy_1}{Leffy_4}$	1.051±0.006	1.073

In the present experiment we cannot make an absolute measurement because we do not have elastic detectors in the straight section. But we can still measure the ratio of the effective lengths between our two location points for both x and y.

The ratios of the effective lengths can be determined from a clean elastic event sample by fitting a straight line to each set of elastic events (data from detectors

1-4 or detectors 2-3), since the straight line fit for detectors 1-4 must have the same slope as the straight line fit for detectors 2-3, we can do a simultaneous fit by minimizing the following χ^2 functions:

$$\chi^2_{yy} = \sum_i \frac{(Y_{1i} - c_{yy} * Y_{4i} - d_1)^2}{\sigma^2_{YY14}} + \sum_i \frac{(Y_{2i} - c_{YY} * Y_{3i} - d_2)^2}{\sigma^2_{YY23}} \quad (4.7)$$

$$\chi^2_{xx} = \sum_i \frac{(X_{1i} - c_{XX} * X_{4i} - d_3)^2}{\sigma^2_{XX14}} + \sum_i \frac{(X_{2i} - c_{XX} * y_{3i} - d_4)^2}{\sigma^2_{XX23}} \quad (4.8)$$

where

$c_{XX} = Leffx_1/leffx_4$

$c_{YY} = Leffy_1/leffy_4$

$\sigma_{XX14}, \sigma_{XX23}$ = sigmas of X4-X1 and X3-X2 distributions, when using only elastics.

$\sigma_{YY14}, \sigma_{YY23}$ = sigmas of Y4-Y1 and Y3-Y2 distributions, when using only elastics.

We used the sample of data in which the detectors were farther away from the beam (i.e. the high $|t|$ data) and applied tight cuts to clean up the elastic sample. There were about 5000 elastics remaining after the cuts from each detector combination that defined an elastic pair. The amount of background remaining inside the XX and YY diagonals was estimated to be about 1%. The results we obtained are shown in Tables 4.6 and 4.7.

The ratios we have measured for the effective lengths in X agree within 2% and in Y within 3% with the values given by the accelerator group. Since E710 measured directly the effective lengths in Y for detectors 1 and 2 with 1.2 % uncertainty and within 0.2% agreement with the accelerator group, the 3.5% disagreement we have with the accelerator group in the Y effective lengths has to come from the uncertainty in the value of the effective lengths for detectors 3 and 4.

Table 4.6: Ratio of Y effective lengths.

	data from detectors 1-4	data from detectors 2-3	simultaneous fit	Accel. group	E710
$\frac{Leffy_1}{Leffy_4}$	1.048±0.006	1.053±0.006	1.050±0.004	1.087	1.051±0.006
d_1	0.900±0.022	0.0	0.891±0.016		
d_2	0.0	-1.534±0.027	-1.524±0.021		
χ^2_{df}	0.957	0.937	0.946		

Table 4.7: Ratio of X effective lengths.

	only data from detectors 1-4	only data from detectors 2-3	Simultaneous fit	Accelerator group
$\frac{Leffx_1}{Leffx_4}$	1.435±0.004	1.439±0.004	1.437±0.003	1.458
d_3	1.502±0.009	0.0	1.504±0.008	
d_4	0.0	0.241±0.008	0.241±0.008	
χ^2_{df}	1.065	1.126	1.097	

Because the effective lengths for detectors 1 and 2 did not change between experiment e710 and e811 (taken during two different Tevatron runs separated by about 7 years) the most conservative approach we can follow in our analysis is to use these two detectors as our defining detectors. The other relevant reason to take detectors 1 and 2 as defining detectors is because of solid angle coverage. The effective lengths in X and Y directions for detectors 1 and 2 are bigger than the ones for detectors 3 and 4, and thus reflects as detectors 3 and 4 having more solid angle coverage than 1 and 2. Then, we use the coordinates of detectors 1 and 2 to determine the scattering angle. Coordinates of detectors 3 and 4 are used for making diagonal cuts (i.e. for determining that the events are elastics) and to determine corrections for geometrical losses. Since the E710 measurement of the effective length in the Y axis for detectors 1 and 2 was obtained with a 1.2%

uncertainty and agreeing with the accelerator lattice calculations, we can expect the accelerator lattice calculations to be within 1.2% uncertainty and quote the same uncertainty for the effective lengths in the X axis.

4.6 Efficiency Determination

The overall efficiency for counting elastics in one combination of detectors defining an elastic pair can be written as the product of the efficiency of the toe counters and the efficiency of the ccds.

$$\varepsilon_{tot} = \varepsilon_{toe}^{(\overline{P})} * \varepsilon_{toe}^{(P)} * \varepsilon_{ccd}^{(\overline{P})} * \varepsilon_{ccd}^{(P)} \tag{4.9}$$

where:
$\varepsilon_{toe}^{(\overline{P})}$,$\varepsilon_{toe}^{(P)}$ are the efficiencies for the toe counters at the antiproton and proton sides.
$\varepsilon_{ccd}^{(\overline{P})}$,$\varepsilon_{ccd}^{(P)}$ are the efficiencies of the whole tracking system for the $\overline{P}$ and proton sides.

4.6.1 Toe Counter Efficiencies

The efficiency of each toe counter was obtained by selecting a sample of good tracks that were elastic candidates and counting how many of them had the toe counter firing within its TDC and ADC windows. A good track was defined as an event that passed the hit uncertainty cuts, cluster intensity cuts, heel ADC and TDC cuts in both detectors as well as X($\overline{P}$)vsX(P) and Y($\overline{P}$)vsY(P) diagonal cuts for elastics; the toe counter in the opposite detector was also required to be hit. Since the heel was required for the efficiency determination, we also had to make fiducial cuts that guaranteed that a particle should traverse both the toe and heel counters of a given detector. For the low $|t|$ data (detectors at about 3.0 mm from

the beam), the first 3.0 mm from the bottom of the toe counter were also cut in the efficiency determination because we are not using that data in our present analysis.

$$\varepsilon_{toe} = \frac{\#\text{good tracks with toe firing}}{\#\text{good tracks}} \tag{4.10}$$

We made a tight cut on the heel counter TDC to guarantee that the time of flight of the particle is consistent with the timing for the main peak in the colliding bunch. We only accepted events whose time of flight, as measured by the heel counter, was within ± 5 ns around the peak of the main bunch . The tight window was made to reduce the contribution of the satellites to the total number of events accepted; since these events cause an underestimation of the toe efficiencies. The overlap between time of flight from satellite bunches and main bunch in the heel counter TDC is caused by its poor time resolution.
We determined the percentage of events from the satellite bunches compared to the number of events from the main bunch that remained inside the heel TDC window. This was done by making cuts on the toe TDC and then counting events inside the heel TDC window. The contamination of satellite events in the heel TDC window for the main bunch was less than 0.1% in all the heel counters.

We also checked that the cross talk between the scintillating bundle and the toe counter, through the led reticle, was not affecting the determination of the toe counter efficiencies. We compared the efficiency of the toe counter obtained by selecting events that hit the detector at the position of the toe reticle lines with the efficiency obtained by only selecting events that did not hit the detector near the reticle lines. The two efficiency values obtained in these two ways were always statistically equal.

Table 4.8 shows the toe efficiencies we obtained for our data. The reason why toe counter efficiencies for detectors 1 and 2 are lower than for 3 and 4 is that for toe counters 1 and 2 the ADC pedestal tail was overlapping the lower tail of the minimum ionizing peak. We had to keep the high voltages down to avoid firing our discriminators with many ADC pedestal pulses.

Table 4.8: Efficiencies of toe counters.

data set #	efficiency toe counter 1	efficiency toe counter 2	efficiency toe counter 3	efficiency toe counter 4
1	0.9959±0.0024	0.9963±0.0026	0.9936±0.0037	0.9980±0.0020
2	0.9901±0.0044	0.9915±0.0038	0.9982±0.0018	1.0000±0.0023
3	0.9892±0.0048	0.9913±0.0039	1.0000±0.0019	1.0000±0.0024
4	0.9833±0.0035	0.9867±0.0026	0.9974±0.0012	0.9975±0.0015
5	0.9719±0.0037	0.9811±0.0027	0.9985±0.0008	0.9985±0.0009
6	0.9589±0.0066	0.9777±0.0043	0.9984±0.0012	0.9989±0.0011
7	0.9774±0.0129	0.9815±0.0106	1.0000±0.0077	1.0000±0.0074
8	0.9732±0.0055	0.9741±0.0045	0.9992±0.0008	0.9978±0.0015
9	0.9742±0.0090	0.9654±0.0085	1.0000±0.0019	1.0000±0.0034
10	0.9804±0.0022	0.9831±0.0019	0.9996±0.0003	0.9997±0.0003

4.6.2 CCD Efficiencies

The ccd efficiencies correspond to the efficiencies of the whole tracking system: Scintillating bundle, image intensifiers, taper and ccd. To find the efficiency of the tracking system in one detector we selected events in which the toe and heel counter of that detector were within TDC and ADC windows; we also required that the conjugate detector, defining the elastic pair, had a hit passing the cluster intensity cut and also having the heel and toe counters firing within TDC and ADC windows. We then counted the number of events in the detector under study that had a cluster consistent with a real particle. The ratio of number of clusters found from the sample to total number of events in the sample gave us the tracking

system efficiency or what we call the ccd efficiencies. Table 4.9 shows the values obtained for the ccd efficiencies in our 10 data sets. The ccd efficiency fluctuations were due to some malfunctioning in the ccds which few times became inactive in the middle of some runs and we had to reset the power on them. The ccds and the ccd electronics had to operate in a high radiation environment, sometimes the ccd electronics malfunctioned due to a spurious particle hitting the chips. The times where we reset the power on the ccds were in one of the runs of data set 1 and data set 4 where ccd 3 was malfunctioning and in data sets 8 and 9, ccds 1 and 2 had to be reset. Data set 1 shows a lower efficiency for ccd 4 because we were running its image intensifiers at lower voltages, they were adjusted for the other runs. Fluctuations of 1.0% in the ccd efficiencies are due mainly to voltage drifting in the image intensifiers and ccd gains which were adjusted at the beginning of each run.

Table 4.9: CCD efficiencies.

data set #	efficiency ccd 1	efficiency ccd 2	efficiency ccd 3	efficiency ccd 4
1	0.9957±0.0021	0.9919±0.0031	0.9128±0.0087	0.9641±0.0133
2	0.9923±0.0023	0.9822±0.0031	0.9845±0.0034	0.9983±0.0012
3	0.9835±0.0034	0.9728±0.0033	0.9848±0.0033	0.9939±0.0023
4	0.9872±0.0017	0.9728±0.0017	0.9447±0.0035	0.9922±0.0015
5	0.9918±0.0010	0.9833±0.0014	0.9745±0.0028	0.9942±0.0011
6	0.9913±0.0013	0.9808±0.0020	0.9746±0.0038	0.9926±0.0015
7	0.9628±0.0084	0.9801±0.0066	0.9803±0.0087	0.9848±0.0068
8	0.8921±0.0050	0.9499±0.0025	0.9850±0.0014	0.9854±0.0020
9	0.9676±0.0047	0.9457±0.0042	0.9897±0.0028	0.9890±0.0035
10	0.9949±0.0013	0.9760±0.0022	0.9886±0.0025	0.9973±0.0009

We also removed the requirement of having the heel counter firing to accept a track, as a way to check for possible biases in the selected sample for the efficiency

determination. We found that for runs in which we could remove all the pedestal noise in the toe counters with the ADC cuts, the values of efficiencies obtained by using or not using the heel were statistically compatible. There were three runs (data sets 7,8 and 9 from Table 4.9) in which the noise levels in the toe counters of detectors 1 and 2 were very high and overlapping with the signal; these pulses were removed when requiring the heel counter in coincidence with the toe.

Table 4.10 shows the efficiency of each elastic pair of detectors as defined by equation 4.9.

Table 4.10: Detector efficiencies.

data set #	efficiency combination 1-4	efficiency combination 2-3
1	0.9541±0.0136	0.8963±0.0099
2	0.9808±0.0055	0.9570±0.0060
3	0.9669±0.0066	0.9497±0.0061
4	0.9607±0.0043	0.9044±0.0045
5	0.9569±0.0040	0.9387±0.0040
6	0.9425±0.0068	0.9331±0.0059
7	0.9267±0.0174	0.9430±0.0163
8	0.8604±0.0073	0.9107±0.0051
9	0.9323±0.0108	0.9036±0.0094
10	0.9725±0.0027	0.9482±0.0037

4.6.3 Correction due to Hit Uncertainty Cuts

As we explained in Section 4.1 we use the hit uncertainty cut to throw away clusters that were already identified but whose hit coordinates were poorly determined due to the high intensity of many pixels in the cluster and to saturation effects in our detectors. We count the number of events in which we find the toe and heel within TDC and ADC windows in each detector and also with clusters above minimum

cluster intensity in both CCDs and then we find the number of events that remain after the hit uncertainty cuts (see Table 4.11). The fluctuation in the % of events accepted with the hit uncertainty cuts is due to the fact that we were increasing with time the voltages on the image intensifiers and ccd gains to try to keep the detectors very efficient, this produced as a result changes in the saturation effects. The big drop observed for ccd4 in data set 9 is due to a temporal shift in ccd gain which shifted the cluster intensity towards higher values.

Table 4.11: Fraction of events remaining after hit uncertainty cuts.

data set #	detector 1	detector 2	detector 3	detector 4
1	0.9476±0.0063	0.9464±0.0057	0.9323±0.0063	0.9412±0.0066
2	0.9516±0.0068	0.9410±0.0069	0.9521±0.0062	0.9325±0.0080
3	0.9465±0.0078	0.9332±0.0074	0.9349±0.0073	0.9370±0.0084
4	0.9424±0.0046	0.9308±0.0039	0.9411±0.0036	0.9263±0.0052
5	0.9361±0.0039	0.9241±0.0035	0.9535±0.0028	0.9190±0.0043
6	0.9205±0.0059	0.9155±0.0052	0.9519±0.0040	0.9220±0.0059
7	0.9145±0.0170	0.9266±0.0136	0.9484±0.0115	0.9368±0.0148
8	0.9080±0.0091	0.9391±0.0070	0.9442±0.0069	0.9200±0.0086
9	0.9039±0.0150	0.9279±0.0081	0.9585±0.0063	0.8605±0.0133
10	0.9318±0.0028	0.9408±0.0023	0.9660±0.0018	0.9348±0.0031

4.6.4 Strobe Pulse Misfiring Correction

We found that in each run there is a small fraction of events in which the ccds did not record any information about the clusters. We can identify a set of events for which the toe and heel counter in each pair of detectors were consistent with a real particle (within TDC and ADC windows) but the ccds in both detectors did not record any pixel with information. This is consistent with the ccds not responding to the strobe pulse used to control the integration time. We checked

each of the four combinations of detectors that the OO trigger is composed of, and all combinations had the same fraction of events with a good particle hitting the toe and heel counters and no information on both ccds. Table 4.12 shows the average fraction of events being lost by the ccds not responding; this is another correction we had to apply to the number of elastics we determined. This correction is of the order of 1.0 % for all the data sets except number 1. For data set 1 the adjustment to operate the ccd camera in asynchronous mode was run too low producing a strobe pulse misfiring in 8.9 % of the events.

Table 4.12: Fraction of events with strobe pulse misfiring.

data set #	fraction of events with strobe pulse misfiring
1	0.0890±0.0040
2	0.0060±0.0006
3	0.0085±0.0006
4	0.0105±0.0004
5	0.0089±0.0004
6	0.0086±0.0004
7	0.0098±0.0014
8	0.0121±0.0006
9	0.0113±0.0007
10	0.0160±0.0011

4.6.5 Overall Corrections

The overall corrections, detector efficiencies and software corrections, that we have to apply to the number of events determined from each elastic pair of detectors is shown in Table 4.13.

Table 4.13: Overall corrections for each elastic combination.

data set #	efficiency combination 1-4	efficiency combination 2-3
1	0.7727±0.0138	0.7181±0.0107
2	0.8651±0.0108	0.8523±0.0100
3	0.8503±0.0119	0.8215±0.0106
4	0.8299±0.0072	0.7839±0.0059
5	0.8159±0.0062	0.8198±0.0053
6	0.7930±0.0092	0.8061±0.0077
7	0.7862±0.0242	0.8206±0.0212
8	0.7045±0.0113	0.8058±0.0095
9	0.7169±0.0182	0.7946±0.0120
10	0.8335±0.0045	0.8479±0.0043

4.7 Geometrical Losses

If we take a small cell of dimensions Δx, Δy in one of the detectors, the coordinates of elastic events from that cell in the conjugate detector are gaussianly distributed. The cause of this smearing effect is the beam size and divergence at the interaction point. Therefore, if we divide the complete detector in small cells, there will be cells with limited acceptance for elastic events since their gaussian distributions will not be fully contained within the area of the conjugate detector. For a cell with coordinates X,Y and dimensions Δx and Δy, with Δx and Δy small, the amount of losses due to the finite size of the conjugate detector can be determined as:

$$\text{losses} = 1 - \frac{\int\int_{Area'} \exp\left(-\frac{(Y-\frac{Leff_Y}{Leff_{Y'}}Y'-Y_0)^2}{2\sigma^2_{YY'}}\right) * \exp\left(-\frac{(X-\frac{Leff_X}{Leff_{X'}}X'-X_0)^2}{2\sigma^2_{XX'}}\right) dX'dY'}{\int_{-\infty}^{\infty}\int_{-\infty}^{\infty} \exp\left(-\frac{(Y-\frac{Leff_Y}{Leff_{Y'}}Y'-Y_0)^2}{2\sigma^2_{YY'}}\right) * \exp\left(-\frac{(X-\frac{Leff_X}{Leff_{X'}}X'-X_0)^2}{2\sigma^2_{XX'}}\right) dX'dY'} \tag{4.11}$$

X' and Y' are the hit coordinates on the conjugate detector. $Area'$ is the area of the conjugate detector. $\sigma_{XX'}$ and $\sigma_{YY'}$ are the width of the XX and YY diagonals as measured in the defining detectors. X_0 and Y_0 are the mean values of the XX and YY diagonals measured in the defining side. If we divide both numerator and denominator by the effective lengths of the defining side we obtained the widths of the elastic distributions in microradians and then we use the values of σ's and mean values from Tables 4.2 and 4.3. We do not need to know the beam positions to determine the corrections for geometrical losses, we only need to use a reference point in each detector and know the values of σ's.

In our analysis, as explained in Section 4.5, we take detectors 1 and 2 as the defining detectors. Therefore we use equation 4.11 integrating over detectors 3 and 4. The size of the cells we take in the defining detectors are 100μm x 100μm.

One advantage we have for taking detectors 1 and 2 as defining is that the solid angle in X covered by detectors 3 and 4 is bigger since the value of the effective length in X is $\approx 43\%$ smaller than in the defining side((Table 4.7). Also the effective length in Y for detectors 3 and 4 is $\approx 5\%$ smaller than in the defining side (Table 4.6) which means more solid angle coverage in Y too. The main source for losses in X is that we ran with a beam offset with respect to the center of the detectors which was worse at the proton side.

Since the binning for counting elastics is done over the Y coordinate (we integrate over the X coordinate), the correction for geometrical losses in each Y-bin, due to X coverage at the conjugate side, is the average correction over all the cells

belonging to the Y-bin. For the values of the Y coordinates with respect to the beam center that we used (Y > 5.0 mm), we found that the average correction for geometrical losses obtained either by weighting each cell belonging to the Y-bin with a flat distribution or with the scattering distribution (equation 1.18) we get the same answer within 0.1% for average losses less than 20%. We only use Y-bins that have loss corrections of less than 10%. We could in principle use only the region of the defining detector which was free of geometrical losses for our present analysis. However the importance of finding a correction for geometrical losses resides in being able to use Y-bins closer to the beam where the contribution from coulomb scattering is higher. These bins will be very valuable for measuring ρ (the ratio of the real to the imaginary part of the scattering amplitude) and to be able to use coulomb scattering for normalization. Figure 4.11 shows the fraction of elastic events expected as a function of position in the detector, for the run with the highest beam offset in the horizontal plane. The white area at the center of the detector represents the area free of losses; the first contour line, from the center of the detector, represents the location where we expect about 1% losses, and every other contour line represents an increase of about 5% losses. When expected losses start to be significant (greater than 10%) we cut out that area of the detector.

4.8 Background Subtraction

After all cuts have been applied, including the diagonal cuts, there will be still some background contaminating the data sample of elastic events. The two main sources of background are beam-gas interactions and beam halo hitting our detectors. Background levels increase drastically when we move our detectors closer to the beam (see Figure 4.9). The highest background levels are found at the lowest

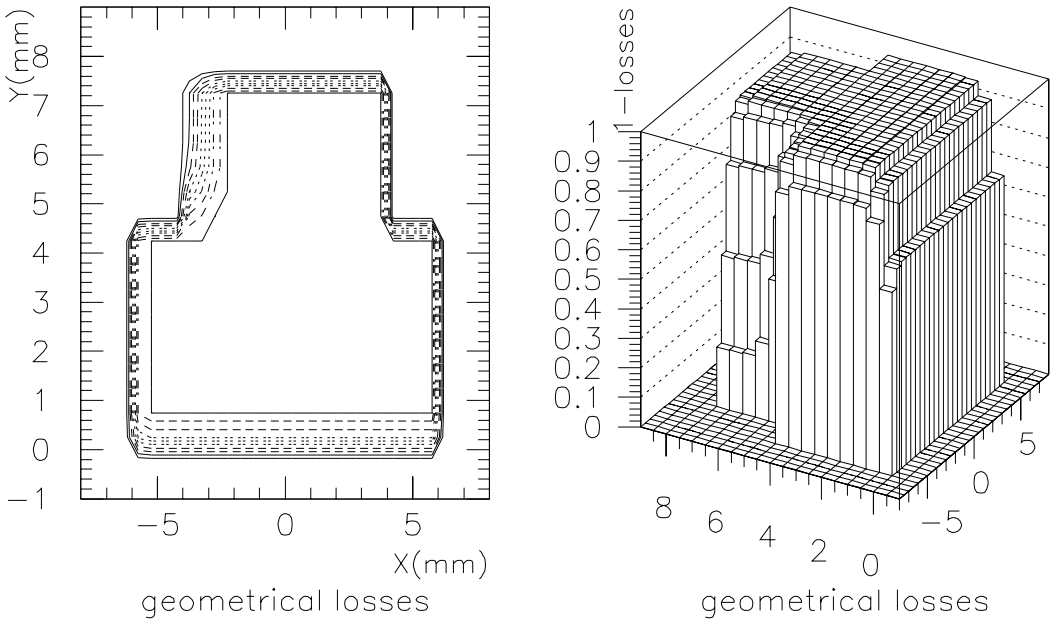

Figure 4.11: Fraction of elastic events expected due to geometrical losses.

X and Y values where also the coulomb scattering contribution becomes significant. It is very important to find a precise method of estimating the background contamination if one intends to use coulomb scattering events as another way of normalizing the elastic data to measure the total cross section. For our present analysis, which is based in finding the optical point, we only have to use the data sample where the nuclear scattering is the only contributor to elastic events. Any contribution from coulomb and nuclear-coulomb interference terms in the scattering amplitude have to be subtracted. Therefore, we only want to use data where these contributions are very small. Because of this constraint we are not using data with Y coordinates within 3.0 mm from the bottom of the detector for the low $|t|$ runs (runs with the detectors placed at about 3.0 mm from the beam axis). We describe below the methods to determine the background in our region of interest.

4.8.1 Off XX Diagonal Events

The background events that get rejected with the diagonal cut to the X(P)vsX($\overline{P}$) scatter plot can be used to estimate the background shape in the Y coordinate. This statement is true if the X and Y distributions for background events are independent. One way to check this is by making slices in the X(P)vsX($\overline{P}$) scatter plot for the events rejected with the diagonal cut and compare the Y distributions from each slice. If we take the slices $3.5\sigma < |\Delta XX| < 5.5\sigma$, $5.5\sigma < |\Delta XX| < 7.5\sigma$, $7.5\sigma < |\Delta XX| < 9.5\sigma$, and plot the Y($\overline{P}$) and Y(P) distributions one finds that the shapes are statistically compatible among the slices; if one takes one Y distribution from a particular slice and uses the Y distribution from one of the other two slices to fit its shape using only a constant parameter to vary in the fit, one finds that the constant where the fit converges agrees to the ratio of the number of events

between the two Y distributions and that the χ^2/d.f. is close to 1.0, which checks out that the distributions are statistically compatible. The comparisons of slice $3.5\sigma < |\Delta XX| < 5.5\sigma$ to $5.5\sigma < |\Delta XX| < 7.5\sigma$ and $3.5\sigma < |\Delta XX| < 5.5\sigma$ to $7.5\sigma < |\Delta XX| < 9.5\sigma$ for one of our high statistics runs are shown in Figure 4.12.

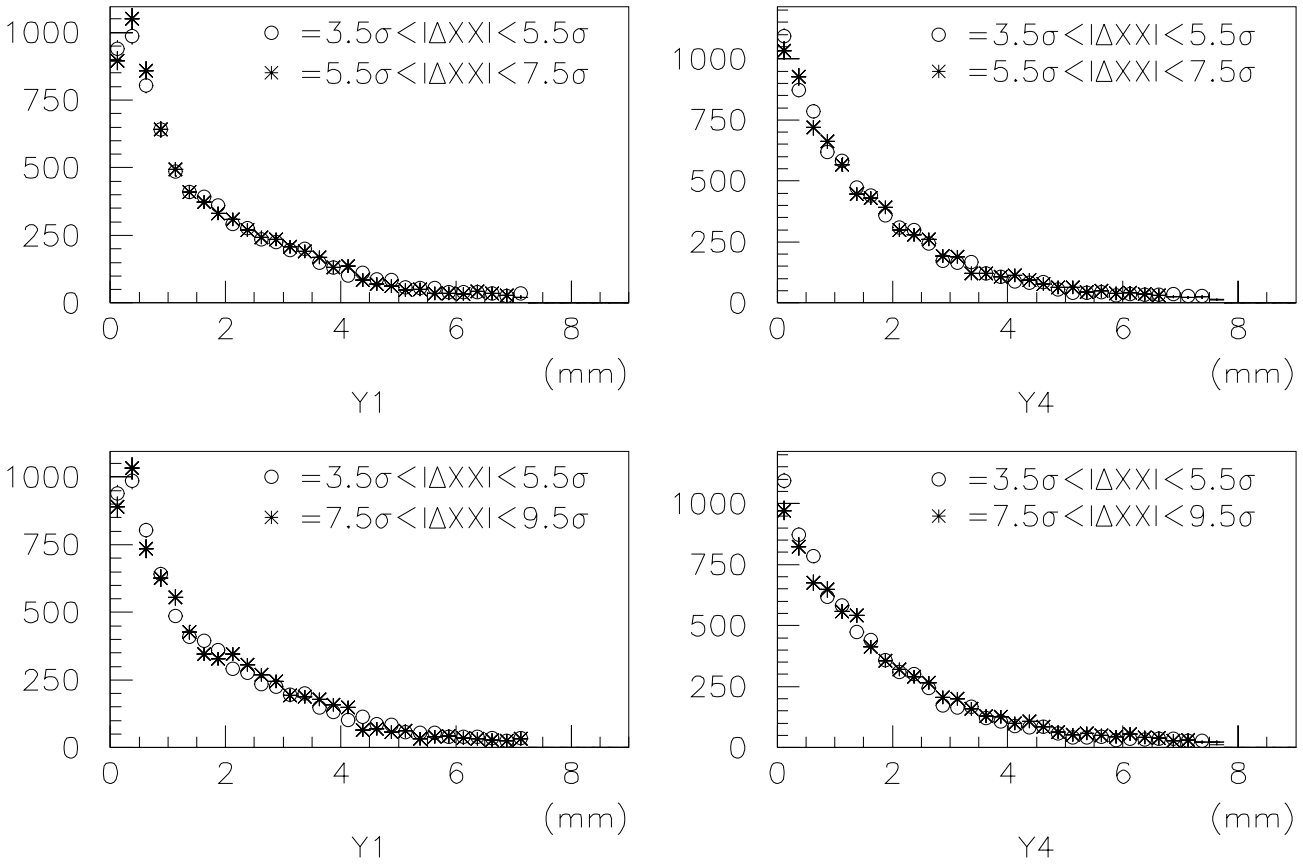

Figure 4.12: Y distributions for events in the windows $3.5\sigma < |\Delta XX| < 5.5\sigma$ and $7.5\sigma < |\Delta XX| < 9.5\sigma$.

Figure 4.13(a) shows the raw X(P)vsX($\overline{P}$) scatter plot with the $3*\sigma$ diagonal cut around the elastic events. Figure 4.13(c) corresponds to the raw Y(P)vsY($\overline{P}$) plot after the $3*\sigma$ X(P)vsX($\overline{P}$) diagonal cut has been applied. The off XX diagonal

events we use to estimate the background shape in Y are shown in Figure 4.13(b) and its corresponding YY plot is in Figure 4.13(d) which is the background shape for the YY plot in Figure 4.13(c). The two triangular regions in Figures 4.13(c) and 4.13(d) correspond to the normalization areas, which are chosen at least $0.5*\sigma$ further than the end of the diagonal cut to avoid any overlap with elastic events; Figure 4.13(d) is normalized to the ratio of events between the triangular areas from the two YY plots. After the normalization is done we apply the diagonal cut to the Y(P)vsY($\overline{P}$) scatter plot to select the elastics. The number of background events inside the YY diagonal cut can be subtracted using the normalized YY distribution in Figure 4.13(d).

Another test that we can perform to check that the off XX diagonal events give the correct shape for the background is to compare the off YY diagonal events that survive the $3*\sigma$ XX diagonal cut (triangular areas in Figure 4.13(c)) to the off YY diagonal events that are also off XX diagonal (triangular areas in Figure 4.13(d)). Figure 4.14 shows the comparison between these two kind of events, both distributions agree within statistics.

Finally, after taking the events that survive both XX and YY diagonal cuts as well as all the other cuts that we apply to clean up the elastic sample we can compare how many of them are expected to be background. This comparison is shown in Figure 4.15. This procedure predicts of the order of 80% of the elastic candidate events being background for Y-bins within 1.0 mm from the bottom of the detector. As we have emphasized before, we are excluding the first 3.0 mm from the bottom of the detector (except for the high $|t|$ runs, data set 1 and 10) for the measurement of the total cross section. In general the lowest Y-bin we use

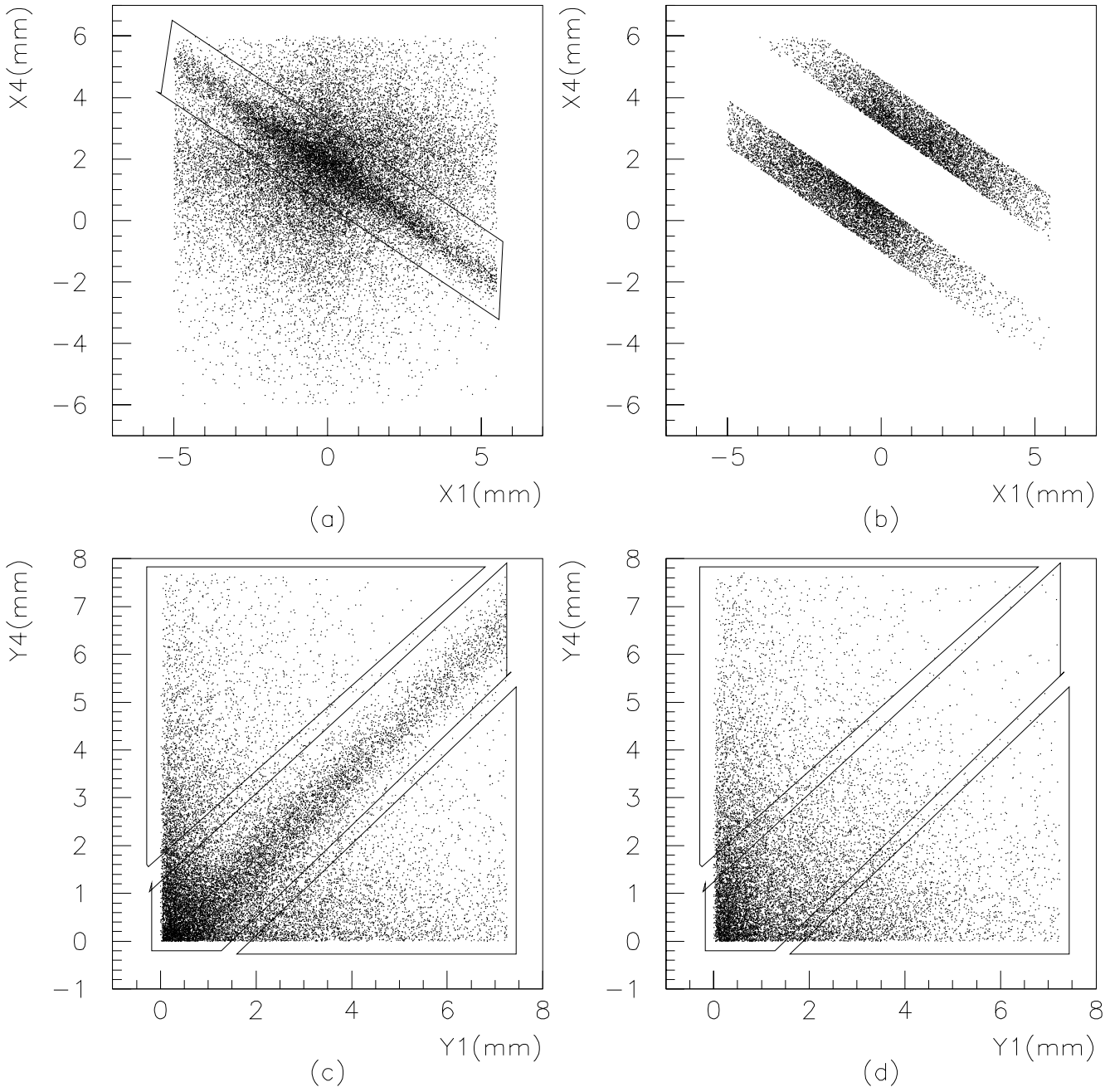

Figure 4.13: YY diagonal events from in ΔXX and off ΔXX events. a) cut to get on XX diagonal events. b) off diagonal XX cut. c) YY data from on XX diagonal events. d) YY data from off XX diagonal events. The triangular areas displayed on c) and d) correspond to the data used for normalization.

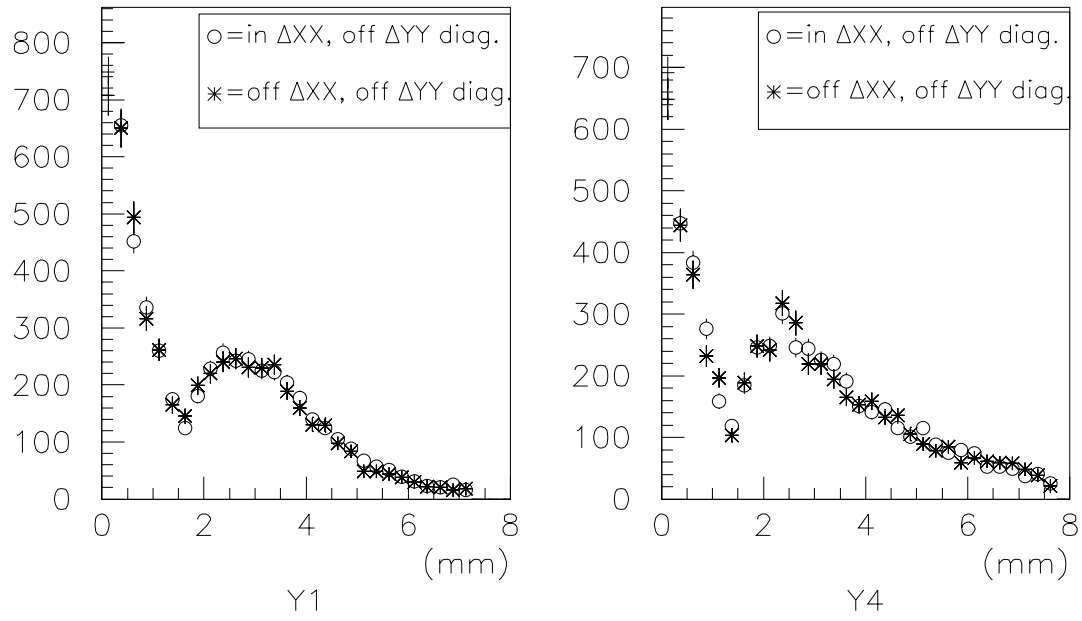

Figure 4.14: Comparison of off YY diagonal distributions for events that survive the ΔXX diagonal cut and events that were off ΔXX diagonal. These are the projections of events from the triangular areas displayed in figure 4.13 c) and d).

has about 20 % background and the bin with largest Y has about 1 % background.

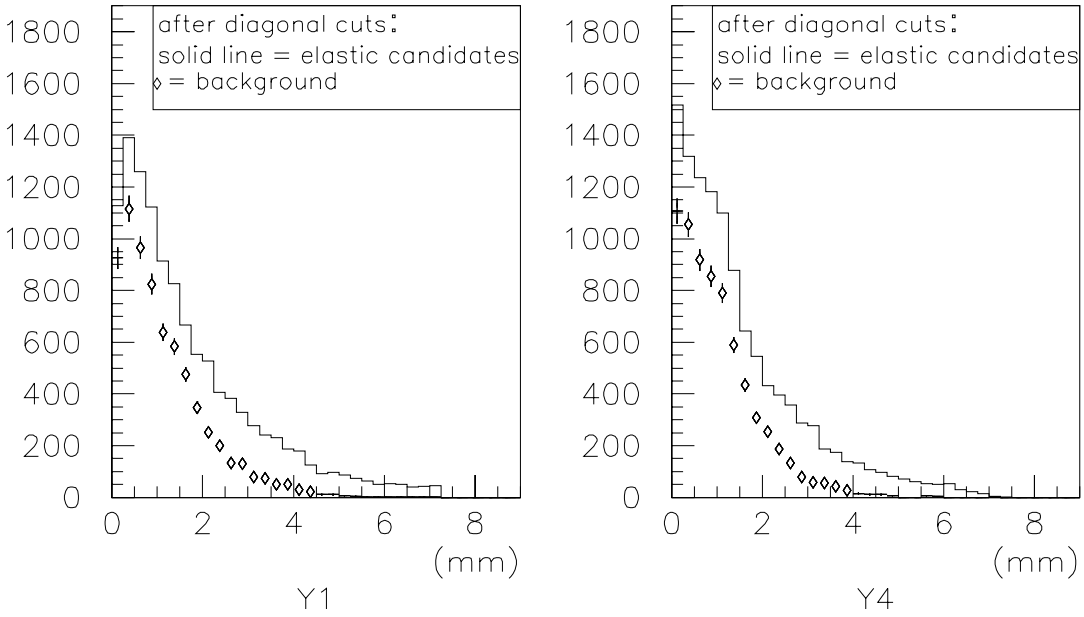

Figure 4.15: Background as a function of Y after integrating over X.

4.8.2 Upper-Upper and Lower-Lower Triggers

The OO trigger is composed of 4 possible coincidences between left and right detectors from the interaction point. Two of these coincidences correspond to elastic candidate events (1-4 or 2-3), there is a coincidence of the two detectors above the beam axis (1-3 or upper-upper) and a coincidence of the two detectors below the beam axis (2-4 or lower-lower) (see Fig 4.16). If we select in software the sample of events only satisfying the upper-upper or lower-lower coincidences, using the same ADC, TDC, cluster cuts required when searching for elastic events, we can use these to determine the background distributions in each detector.

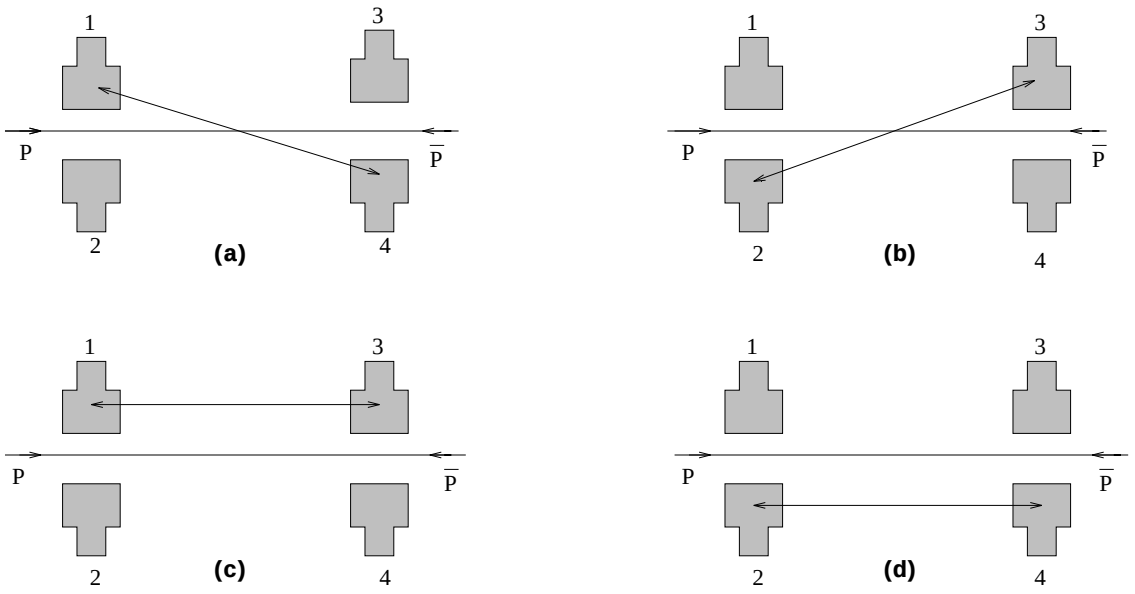

Figure 4.16: OO coincidences. a) and b) are the two elastic combinations. c) is the upper-upper trigger, d) is the lower-lower trigger.

A comparison of the Y background shape in detectors 1 and 4 obtained with the upper-upper and lower-lower triggers to the one obtained using off XX diagonal events from coincidence 1-4 is shown in Figure 4.17 where the distributions are normalized to the same number of events. As one can see both methods give the same background shapes. The method we use in the present analysis for background subtraction is the one that uses the off XX diagonal events.

4.8.3 Interpolation Method

We apply all cuts described before doing an extra step in between the diagonal cuts. We apply the XX diagonal cut first and before applying the YY diagonal cut, we fit to each Y-bin a function with the shape:

$$\begin{aligned} f(Y_i) &= background(Y_i) + elastics(Y_i) \\ &= \frac{K_1 * \exp\left(-c * (Y_i + \Delta)\right)}{(Y_i + \Delta)^n} + K_2 * \exp\left(-\frac{(Y_i + \Delta - Y')^2}{2 * \sigma^2}\right) \end{aligned} \quad (4.12)$$

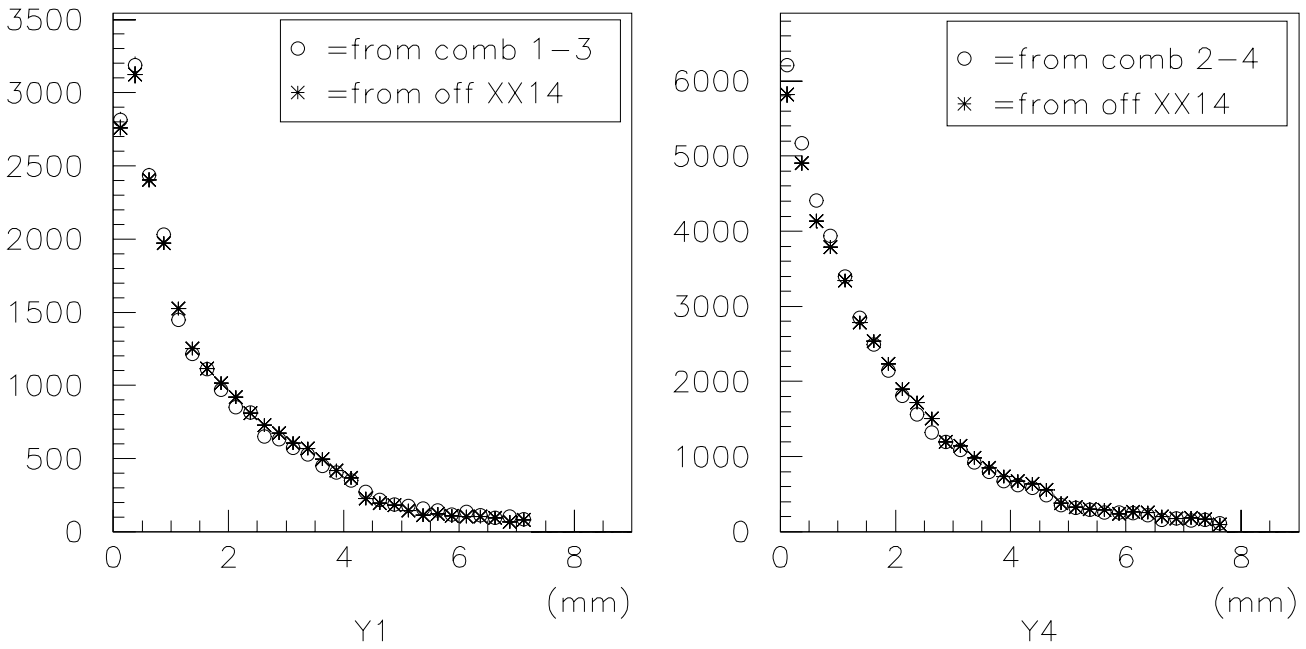

Figure 4.17: Comparison of off XX diagonal events to upper-upper and lower-lower triggers.

Where Y_i is the Y projection on the conjugate detector of events belonging to bin i in the defining detector (0.25 mm bins). Y_i is measured from the bottom of the conjugate detector. Δ is the distance from the bottom of the detector to the midpoint between upper and lower detector where we expect the beam axis to be.

The elastic events follow a gaussian distribution in the Y coordinate of the conjugate detector, the width of the gaussian was previously measured and it is shown in Tables 4.2 and 4.3. The background is fit to a function $\exp(-c*y)*y^{-n}$. This function was guessed by fitting different functions to the Y background shape obtained from upper-upper and lower-lower triggers and picking up the one that gives the best $\chi^2/d.f.$. The initial fit parameters were K_1, K_2, Y',c,n. However after fitting every Y-bin in the defining detector we found that the values of c,n were always consistent with the fit previously done to the upper-upper and lower-lower data to guess the background function to use. So we just fix the values of c and n and just allow three free parameters in the fit: K_1, K_2 and Y'. Figure 4.18 shows the fit obtained for 4 different bins in detector 1 for one of our high statistic runs where the detectors were located at about 3.0 mm from the beam. We observe an elastic peak with background tails on either side. For Y-bins very close to the bottom of the detector the fit becomes less reliable since we can fit only the the tail at larger Y. Then this method becomes an extrapolation rather than an interpolation. Once we obtain the fit parameters for the background shape we apply the YY diagonal cut and subtract the remaining background predicted by the function we fit, that background is represented by the dashed lines underneath the gaussian peak in Figure 4.18.

Figure 4.19 shows the comparison of the off XX diagonal method to the In-

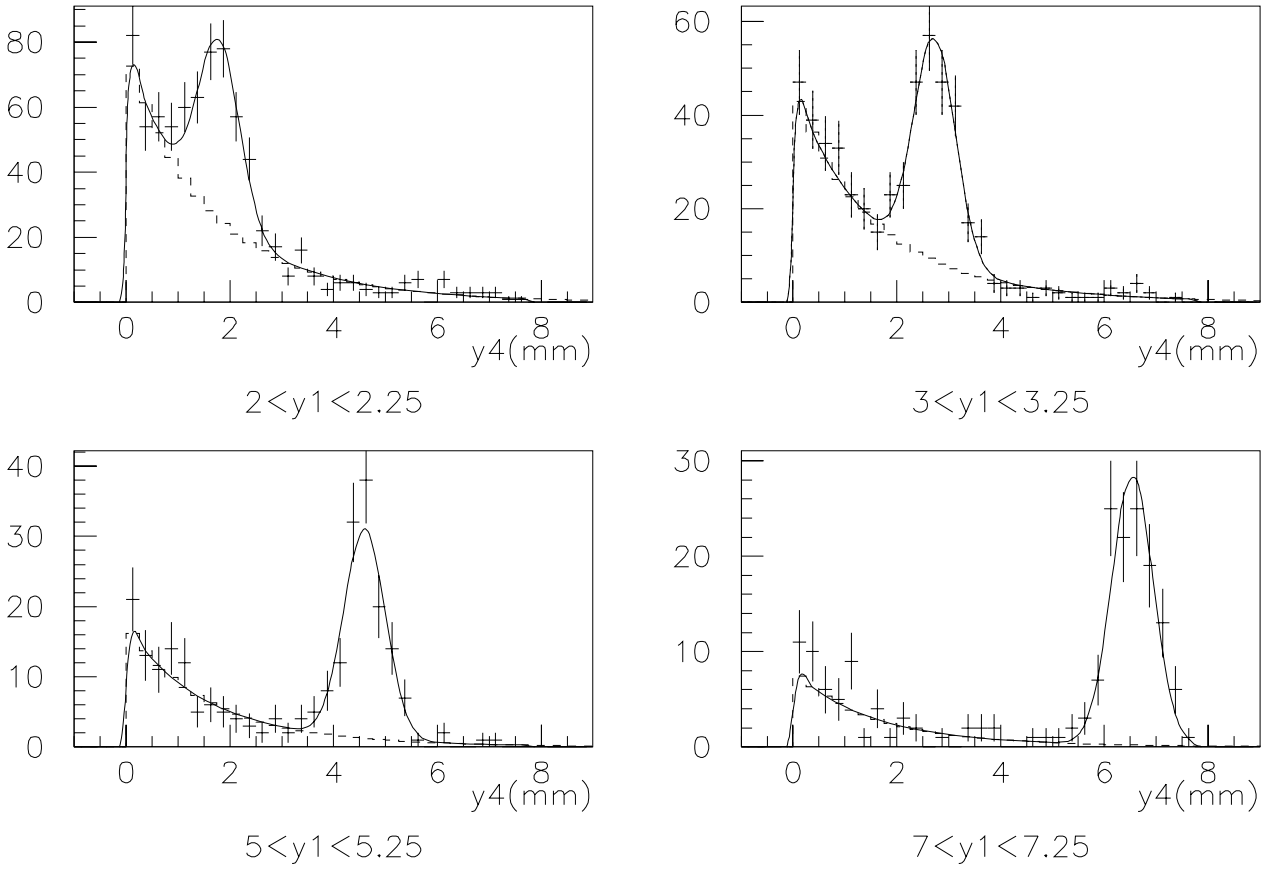

Figure 4.18: Background + Elastics in four different Y-bins of detector 1.

terpolation method. Both give the same background estimation within statistics. The background method we use in our analysis is the off XX diagonal method.

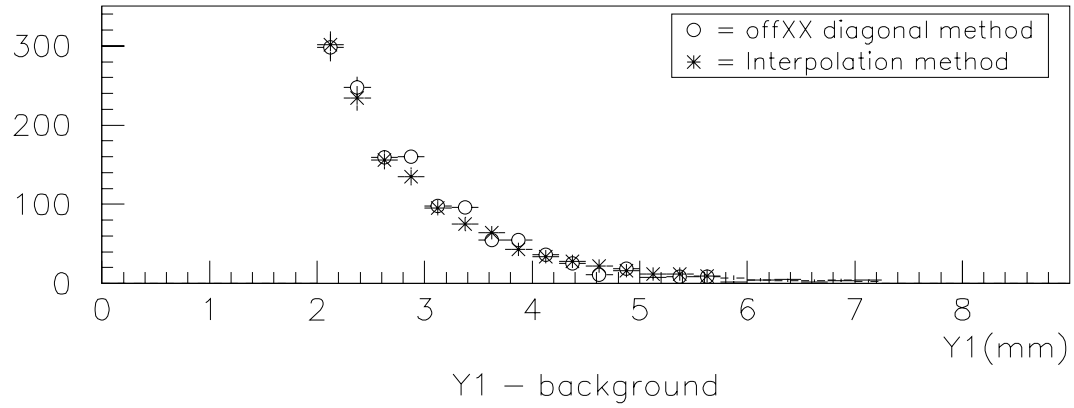

Figure 4.19: Comparison of background measured by the off XX diagonal method and the interpolation method.

4.9 Beam Position

The X, Y coordinates used for estimating the geometrical losses and background subtraction were measured using as origin the center point of the bottom edge of the toe counter. To obtain the hit coordinates with respect to the beam we need to measure the vertical distance between the bottom edge of the toe counter and the beam axis, as well as the distance in the horizontal plane of the beam axis and the center of the toe counter (see equation 4.4). In the two sections below we describe how we determine these distances.

4.9.1 Horizontal Beam Position

The horizontal beam position can be obtained by using events that pass all the requirements for an elastic candidate. This sample consists of elastics plus back-

ground events. The X distribution of elastic events in each detector is fairly flat because we only have coverage of ± 6.0 mm and since most of the elastics recorded are produced from nuclear scattering they follow a gaussian with $\sigma \approx 8.7$ mm for detectors 1 and 2 and $\sigma \approx 6.0$ mm for detectors 3 and 4. The X distribution for background events is much more steeper allowing a better determination of the X beam center. Even though we have observed that the X distribution for background events is not symmetric around the beam (see Figure 4.20) we can still fit a gaussian to the central part of the distribution to obtain the X beam position, as is shown in Figure 4.20.

Table 4.14 shows the values for horizontal beam positions as measured from the center of the toe counter in each detector. Table 4.15 shows the differences between the X beam positions for the two detectors at the same location (notice that there is a change in sign for the X coordinate between up and down detectors at the same location, see Section 4.3), one would have expected that the centers of the two toe counters, up and down, at the same location to be aligned to each other, however detector 1 has a rotation on the horizontal plane which produces an offset between the toe centers of detectors 1 and 2. The toe counter on detector 3 has a lateral shift that was produced during the process of glueing the toe counter to the bundle, that shift was measured to be about 0.7 mm which is consistent with the shift in the toe centers for detectors 3 and 4.

Once we obtain the X beam positions for each detector we can use equation 4.4 to find the X coordinates with respect to the beam. If we select a clean sample of elastic events ,by only accepting events at higher Y, and plot the distribution $\Delta X = X_{left} - \frac{Leffx_{left}}{Leffx_{right}} * X_{right}$, where X_{left}, X_{right} are the X hit coordinates for the left and right detectors from the interaction point that define the elastic pair,

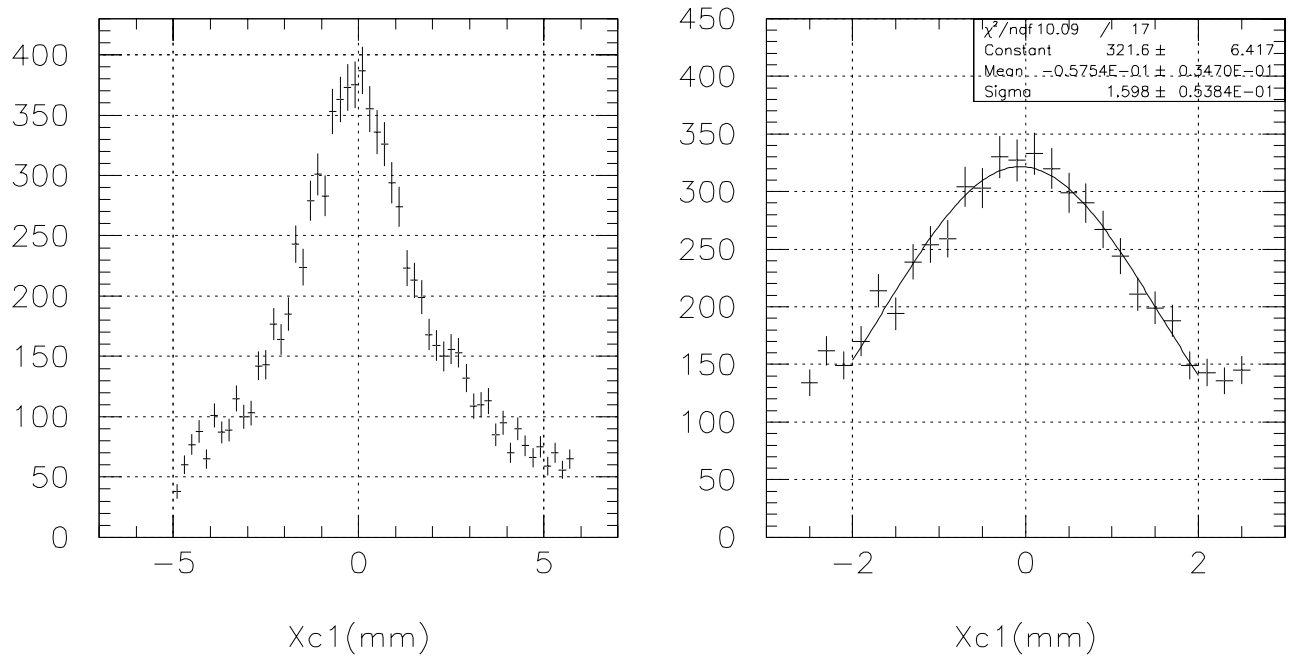

Figure 4.20: X distribution for halo+elastics in detector 1. The Central region of the distribution is fit to a gaussian.

Table 4.14: X beam offsets with respect to the center of the toe counter.

data set #	Xbeam offset det. 1 (mm)	Xbeam offset det. 2 (mm)	Xbeam offset det. 3 (mm)	Xbeam offset det. 4 (mm)
1	0.882±0.215	0.07±0.234	0.411±0.174	0.170±0.212
2	0.769±0.086	-0.040±0.080	0.472±0.079	0.195±0.125
3	0.724±0.061	0.023±0.042	0.460±0.125	0.196±0.088
4	0.788±0.060	-0.057±0.032	0.542±0.053	0.216±0.039
5	-0.057±0.035	0.653±0.072	-1.043±0.017	1.724±0.029
6	-0.009±0.070	0.635±0.054	-1.006±0.040	1.818±0.049
7	0.814±0.127	-0.016±0.090	0.230±0.089	0.304±0.106
8	0.817±0.053	0.064±0.083	0.238±0.054	0.345±0.050
9	0.860±0.108	0.056±0.067	0.140±0.053	0.386±0.096
10	0.265±0.191	0.022±0.186	0.150±0.152	0.847±0.168

Table 4.15: X offsets between the center of the two toe counters, up and down, at the same location.

data set #	ΔX12 (mm)	ΔX34 (mm)
1	0.889±0.318	0.581±0.274
2	0.729±0.117	0.667±0.148
3	0.747±0.074	0.656±0.153
4	0.731±0.068	0.758±0.066
5	0.596±0.080	0.681±0.034
6	0.626±0.088	0.812±0.063
7	0.798± 0.156	0.534±0.138
8	0.881± 0.098	0.583±0.074
9	0.916± 0.127	0.526±0.110
10	0.287± 0.267	0.997±0.227
average	0.724±0.032	0.690±0.024

we should see that ΔX distribution (which sometimes is called the X collinearity distribution, see Figure 4.21) should be centered around 0, some small offsets can be expected either from offset at the interaction point, uncertainties in the X beam position or uncertainty in the ratio of the effective lengths.

Also events from upper-upper and lower-lower triggers were used to verify the horizontal beam positions. However, we found that the X distribution of events from upper-upper trigger (events triggering detectors 1 and 3) in detector 3 had their X distribution peaking at a different position as found with the above procedure (the X distributions for the other 3 detectors were peaking at about the same place), if we use the X beam positions found with the upper-upper and lower-lower triggers we always endup with a collinearity distribution for detectors 2 and 3 centered at around 1.0 mm. The collinearity distribution for detectors 1 and 4 was still centered around 0. This helped us to conclude that detector 3 was being hit by some additional kind of events scattered off an accelerator scraper that did not

follow the normal beam pattern. This is the reason why we only used events satisfying all the elastic requirements for measuring the horizontal beam position. Also it is important to notice that since detectors 1 and 2 are the defining detectors we only need to know the beam position for these two detectors and the information of beam positions for detectors 3 and 4 never plays a role in the analysis.

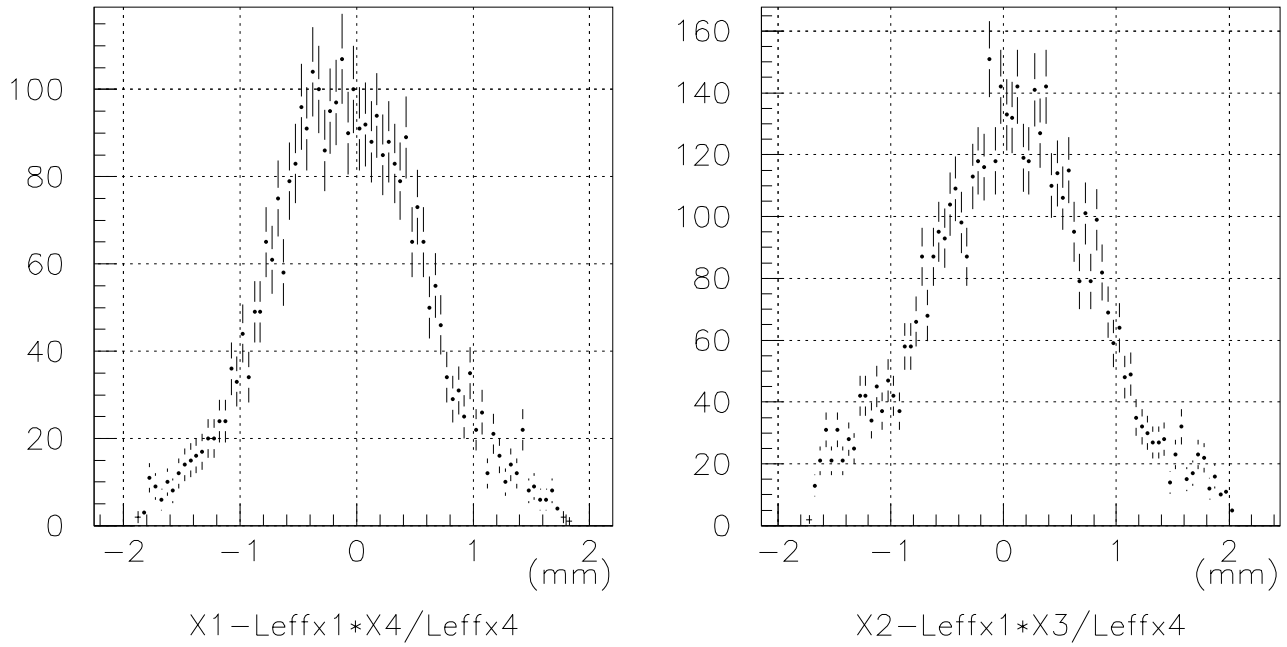

Figure 4.21: X collinearity distributions for detector combinations 1-4 and 2-3, data set 5.

4.9.2 Vertical Beam Position

At the time of the data taking we vertically positioned the upper and lower detectors so that the rates of their toe counters timed to the RF were about the same. Then we concluded that the beam axis in the vertical plane was located near the mid point between the two toe counters. We measured very accurately the dis-

tance between the "bottom" edges of the two toe counters (see section 2.3.4). In software we can determine the offset of the beam axis with respect to the mid point of the two toe counters. We use only background events to obtain this offset. The assumption we initially make is that the X and Y distributions for halo particles in both detectors, up and down from the beam at the same location, should have the same shapes. If our assumption is valid then we can just determine the beam position by fitting the Y background distribution of one detector to the Y background distribution of the other allowing two free parameters, one the beam offset with respect to the mid point (ΔY_{beam}) and second a normalization factor between the two distributions (K_{bck}). The normalization factor is needed to account for difference in acceptance between the upper-upper and lower-lower triggers.

$$N_{bck}(Y1_i) = K_{bck} * N_{bckg}(Y2_i + 2 * \Delta Y_{beam}) \tag{4.13}$$

where $N_{bck}(Y)$ is the shape function.

To prove that the Y background shapes in the two detectors at the same location are the same, we find a function that fits the Y background shape in one of the detectors and show that the same function with the same parameter values except normalization and offset can be used to fit the Y background shape in the other detector. We found that this is possible to do in detectors 1 and 2 but detectors 3 and 4 seem to have different Y background shapes which is the result of some events scattered off an accelerator scraper causing asymmetries between the Y distribution shapes of these two detectors. The X distribution of detector 3 showed evidence of scraping events not following the normal beam pattern (see Section 4.9.1). Figure 4.22 shows the comparison of the background shapes for detectors 1 and 2 where a function of the shape $N_{bck}(Y) = K_1 * \frac{\exp(p1*Y)}{Y^{p2}}$ was used to fit the Y distribution

in detector 2 obtained from lower-lower trigger (events triggering detectors 2 and 4), The values obtained from this fit were used to fit the same function (now with p1 and p2 fixed) to the Y distribution in detector 1 obtained from upper-upper trigger, allowing a normalization and y offset as free parameters for this second fit. The fact that we cannot get in this way the vertical beam position for detectors 3 and 4, is not a problem because we do not need to know the beam position for detectors 3 and 4 for any part of the analysis because our defining detectors are 1 and 2.

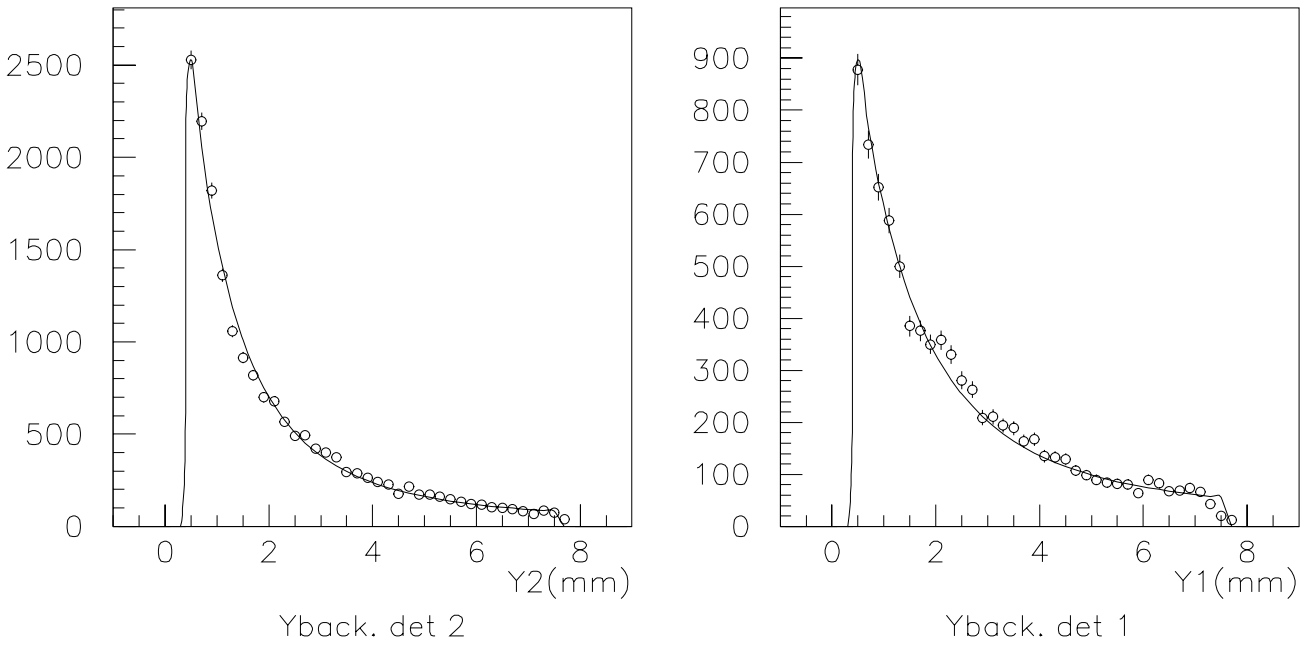

Figure 4.22: Comparison of background shapes in detectors 1 and 2.

Any error we make in determining the vertical beam position has almost no effect in our final measurement since we at the end average the number of elastic events determined from detector 1 with the ones determined from detector 2. The

average washes out, to first order, any error in finding the vertical beam position. The only relevant parameter to know with good accuracy is the distance between the bottom edges of the toe counters of detectors 1 and 2 at the time of our data taking (see Sections 2.3.4 and 2.8).

Table 4.16 shows the vertical beam offsets obtained for our 10 data sets when using equation 4.13 :

Table 4.16: Y beam offset with respect to the center point between detectors 1 and 2 ("+" indicates that the beam is further away from detector 1).

data set #	$\Delta Y12_{beam}$ (mm)
1	0.325±0.123
2	-0.002±0.105
3	0.315±0.102
4	0.378±0.112
5	-0.004±0.120
6	0.003±0.168
7	0.03±0.115
8	-0.03±0.102
9	0.24±0.121
10	0.48±0.101

4.10 Coulomb and Nuclear-Coulomb Interference Contributions

Since we want to extrapolate to $|t| = 0$ the $\frac{dN}{dt}$ distribution produced by nuclear scattering events we need to subtract the other two terms that contribute to $\frac{dN}{dt}$ which are the coulomb scattering and the nuclear-coulomb interference terms. We divide each defining detector in small cells of 100 μm x 100μm and since we can determine the X,Y coordinates from the beam, i.e. the $|t|$ value, for each cell then

we can calculate the contributions from each term, nuclear, nuclear-coulomb and coulomb, by using equation 1.18. Since we are integrating over X we just add the contributions from coulomb and nuclear-coulomb interference terms from each cell and find the percentage contribution in the Y-bin. There are three parameters in equation 1.18 that we do not know, σ_T, ρ and B. For B value we use the world average (see Section 4.11) which we also measure ourselves in this experiment although with a bigger error than the world average. For σ_T and ρ we use two extreme values based on previous measurements performed by other experiments at this energy and from lower energy data, [8], [13], [14], [17] (σ_T=60, ρ=0.19 and $\sigma_T = 90$, ρ=0.09), the amount we subtract is the mean between the two extreme values quoting as error the effect of distance of the mean to the extreme values. Once we obtain a measurement of the cross section we use that value of the cross section and reevaluate the amount of coulomb and nuclear-coulomb interference contributions by only using the extreme values for ρ. One reason we integrate over X and also cut the first 3.0 mm from the bottom of the detector is to guarantee that the amount of coulomb and interference to subtract is small. Table 4.17 shows the initial subtraction in each bin for one run where the bottom edge of the detectors was about 3.0 mm from the beam.

4.11 Extrapolation to $|t| = 0$

Table 4.17 shows the integration limits in X for each Y-bin. We used two different X limits because the toe counters have a "T" shape. To plot $\frac{dN}{dy}$ we just normalize one X region to the other.

Table 4.17: Interference + Coulomb contributions in each Y-bin when averaging two extreme values σ_T=60,ρ=0.19 and σ_T=90,ρ=0.09.

Y from beam	X_{min}	X_{max}	from toe bottom Y_{min}	from toe bottom Y_{max}	interference subtraction (%)	coulomb subtraction (%)
6.070	-5.800	5.800	3.000	3.250	2.6±1.3	1.2
6.320	-5.800	5.800	3.250	3.500	2.5±1.2	1.1
6.570	-5.800	5.800	3.500	3.750	2.4±1.2	0.9
6.820	-5.800	5.800	3.750	4.000	2.3±1.1	0.9
7.070	-5.800	5.800	4.000	4.250	2.2±1.1	0.8
7.320	-5.800	5.800	4.250	4.500	2.1±1.0	0.7
7.570	-3.500	3.500	4.500	4.750	2.3±1.1	0.9
7.820	-3.500	3.500	4.750	5.000	2.2±1.1	0.8
8.070	-3.500	3.500	5.000	5.250	2.1±1.0	0.7
8.320	-3.500	3.500	5.250	5.500	2.0±1.0	0.6
8.570	-3.500	3.500	5.500	5.750	1.9±0.9	0.6
8.820	-3.500	3.500	5.750	6.000	1.8±0.9	0.5
9.070	-3.500	3.500	6.000	6.250	1.7±0.9	0.5
9.320	-3.500	3.500	6.250	6.500	1.7±0.8	0.4
9.570	-3.500	3.500	6.500	6.750	1.6±0.8	0.4
9.820	-3.500	3.500	6.750	7.000	1.6±0.8	0.4
10.070	-3.500	3.500	7.000	7.250	1.5±0.7	0.3
10.320	-3.500	3.500	7.250	7.500	1.4±0.7	0.3

For elastic events produced by nuclear scattering we can write:

$$\begin{aligned} \frac{dN}{dt} &= \left(\frac{dN}{dt}\right)_{t=0} \exp(-B\,|t|) \\ \frac{dN}{dt} &= \left(\frac{dN}{dt}\right)_{t=0} \exp(-\frac{Bp^2X^2}{L^2_{effX}}) \exp(-\frac{Bp^2Y^2}{L^2_{effY}}) \end{aligned} \tag{4.14}$$

Also $\frac{dN}{dt}$ is related to the solid angle as

$$\begin{aligned} \frac{dN}{dt} &= \frac{1}{p^2}\frac{dN}{d\Omega} \\ &= \frac{\pi}{p^2}\frac{dN}{\frac{dX}{L_{effX}}\frac{dY}{L_{effY}}} \end{aligned} \tag{4.15}$$

Using equations 4.14 and 4.15 we can write $\frac{dN}{dy}$ as

$$\frac{dN}{dy} = \frac{p^2}{\pi L_{effX} L_{effY}} \left(\frac{dN}{dt}\right)_{t=0} \left\{ \int_{X_{min}}^{X_{max}} \exp(-\frac{Bp^2X^2}{L^2_{effX}})dX \right\} \exp(-\frac{Bp^2Y^2}{L^2_{effY}}) \tag{4.16}$$

If we plot $\log(\frac{dN}{dY})$ versus Y^2 we can fit a straight line to the data. The slope of the straight line is related to B and the intercept $(\left(\frac{dN}{dY}\right)_{y^2=0})$ is related to $\left(\frac{dN}{dt}\right)_{t=0}$ as

$$\left(\frac{dN}{dY}\right)_{y^2=0} = \frac{p^2}{\pi L_{effX} L_{effY}} \left(\frac{dN}{dt}\right)_{t=0} I(X, X_{min}, X_{max}) \tag{4.17}$$

where $I(X, X_{min}, X_{max}) = \int_{X_{min}}^{X_{max}} \exp(-\frac{Bp^2X^2}{L^2_{effX}})dX$

Figure 4.23 shows the $\frac{dN}{dY}$ versus Y^2 distributions for data set 10 (high $|t|$ data) and for data set 5 (low $|t|$ data) and their corresponding fits. We have put in the same plot the data from detector 1 (positive Y^2) and the data from detector 2 (negative Y^2) obtained in the same run; the intercepts from both detectors always agree within statistics. The reason why we have fewer points in the low $|t|$ data compared to the large $|t|$ data is because for all the runs with the detectors located at about 3.0 mm (low $|t|$ data) from the beam we cut the first 3.0 mm from the

bottom of the detector to only allow a small subtraction of coulomb and nuclear-coulomb interfence contribution to the number of elastics and also to use a region with low background levels. The intercept we use for obtaining $\left(\frac{dN}{dt}\right)_{t=0}$ is the average of the two intercepts in each run. When we fit simultaneously the 10 data sets we have, allowing a normalization per run and with the same slope for all the 10 data sets, we obtain a measurement of the B value:

$$\begin{aligned} B &= 17.31 \pm 1.47\ (GeV/c)^{-2} \\ \chi^2/d.f. &= 0.84 \end{aligned} \tag{4.18}$$

The B value we obtain agrees with previous measurements at the same energy (CDF measured B = 16.98 $\pm$ 0.25 $(GeV/c)^{-2}$, [9]. E710 measured B = 16.99 $\pm$ 0.47 $(GeV/c)^{-2}$ [14]) but our error is much larger than previous measurements because of the limited $|t|$ ranges of the measurement of this experiment. We fix B to the world average (B = 16.99 $\pm$ 0.22 $(GeV/c)^{-2}$) to obtain the intercept that we use for the measurement of the total cross section.

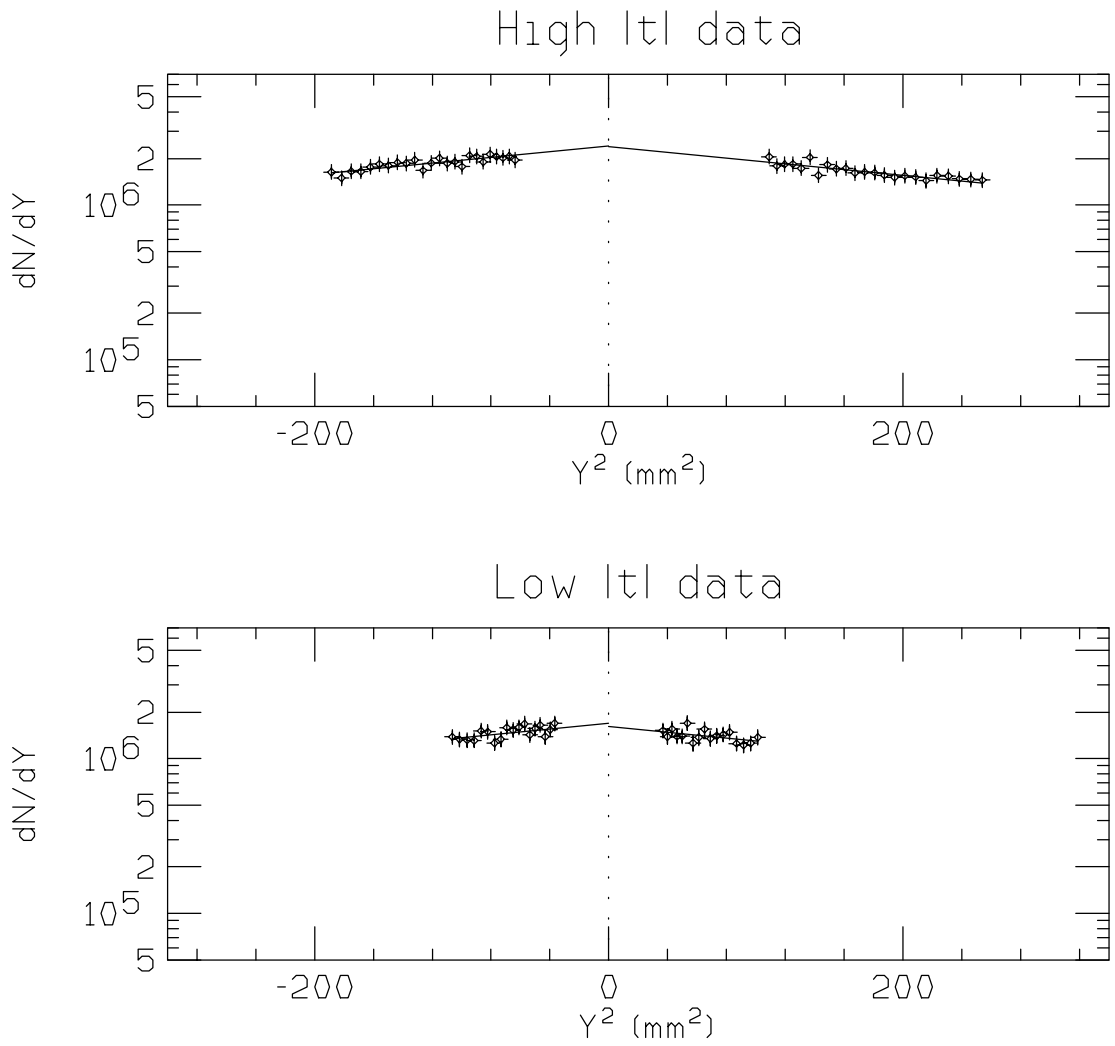

Figure 4.23: $\frac{dN}{dY}$ vs Y^2 distributions for data set 10 (high $|t|$ data) and data set 5 (low $|t|$ data). Data from detector 1 is plotted with Y^2 positive, data from detector 2 is plotted with Y^2 negative.

CHAPTER 5

Inelastic Data Analysis

We determine here the number of double arm events from which we determine N_{in}. This along with the measurement of $\frac{dN_{el}}{dt}\Big|_{t=0}$ leads to the determination of the total cross section as is explained in section 3.5.

The hardware trigger used to record the double arm events is

$$LR = (L_3 + L_4 + L_5) * (R_3 + R_4 + R_5) \tag{5.1}$$

The pseudorapidity coverage for our ring counters is given in Section 5.3. We apply cuts on the ADC and TDC of each inelastic counter (see Section 5.1) to identify a real particle striking the counter. When we check the number of counters being hit by real particles for one LR trigger, we find that the number is usually very large (see Figure 5.2). Because of this high counter multiplicity the final count of number of good double arm events would not be affected even if some of the counters were not fully efficient, however all our counters are near 100 % efficient as can be estimated from the ADC distributions since we can determine the lower tail of the minimum ionizing peak (see Figure 5.1). Since the η coverage by the ring counters forming the LR trigger is limited we need to determine the fraction of events that actually get recorded with the LR trigger, this is done in section 5.7.

There are two extra corrections that we have to apply to the number of LRs; one is a veto produced in our hardware logic which we call the early veto correction (Section 5.4), the second has to do with the amount of background remaining in the LR events after the event selection criteria has been applied. The background remaining is mostly beam-gas beam-gas accidentals in the inelastic counters at each side of the interaction point (Section 5.5).

5.1 Double Arm Event Selection

An event is classified as a double arm if the LR prescaler increments by 1, which indicates that the event was recorded through the LR hardware trigger, and if there is at least one counter L_3, L_4 or L_5 with a hit and one counter R_3, R_4 or R_5 with a hit, where the hit has to be consistent with a minimum ionizing particle in both counters (i.e. above ADC cuts) and inside the TDC window for the late peak in both counters. Even though the LR hardware trigger has a veto for early hits (see Section 5.4) we still can get hits from the satellite bunches, specially the late satellite (see Figure 5.1), and we reject these in our analysis.

Figure 5.1 shows typical TDC and ADC distributions for events triggered by LR, the cuts we apply are also shown. The number of LR events is not that sensitive to the inefficiencies that we could have in some counters, this is why we do not talk about efficiencies of the ring counters because we do not need to measure them, however from the ADC distribution of each counter we can estimate that every counter is near 100% efficient. To prove that the number of LRs does not get affected by one counter being inefficient we can just move the ADC cut displayed in Figure 5.1 to a higher ADC channel, for example channel 500, If we

recount the number of LRs with the new ADC cut for that counter(which makes the counter very inefficient) we find that the LR count drops by 0.2%. We can even turn off completely that counter by requiring an ADC cut higher than the overflow channel and we find that in this case the number of LR events drops by 0.4%. Since we can see the lower tail of the minimum ionizing peak in the ADC distribution of every counter that makes the LR trigger and because our higher statistics run has a statistical error of 0.55% in the number of LR events, we can conclude that some low inefficiencies in the ring counters produce an error smaller that the statistical error.

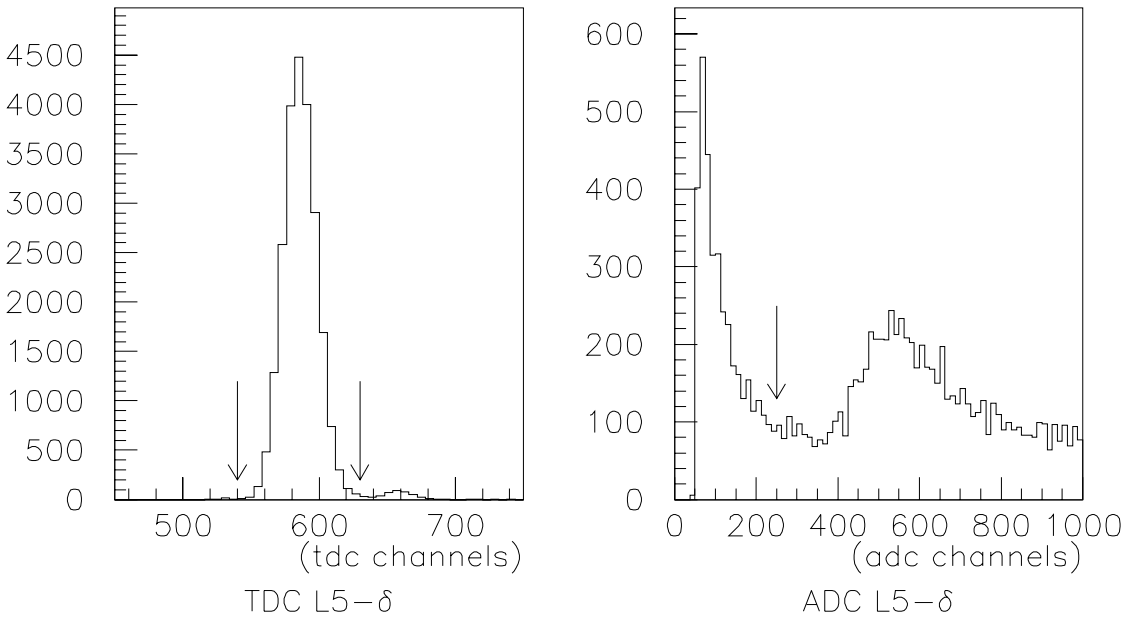

Figure 5.1: TDC and ADC distributions for LR events in ring counter $L_{5\delta}$ (1 TDC channel is ≈ 0.25 ns) .

The reason why the number of LR events is insensitive to some counter ineffi-

ciencies is because the ring counter multiplicity for LR events is very high. There is only a small fraction of LR events which have only one counter hit at each side of the interaction point. Figure 5.2 shows the distribution of total number of ring counters hit for LR events.

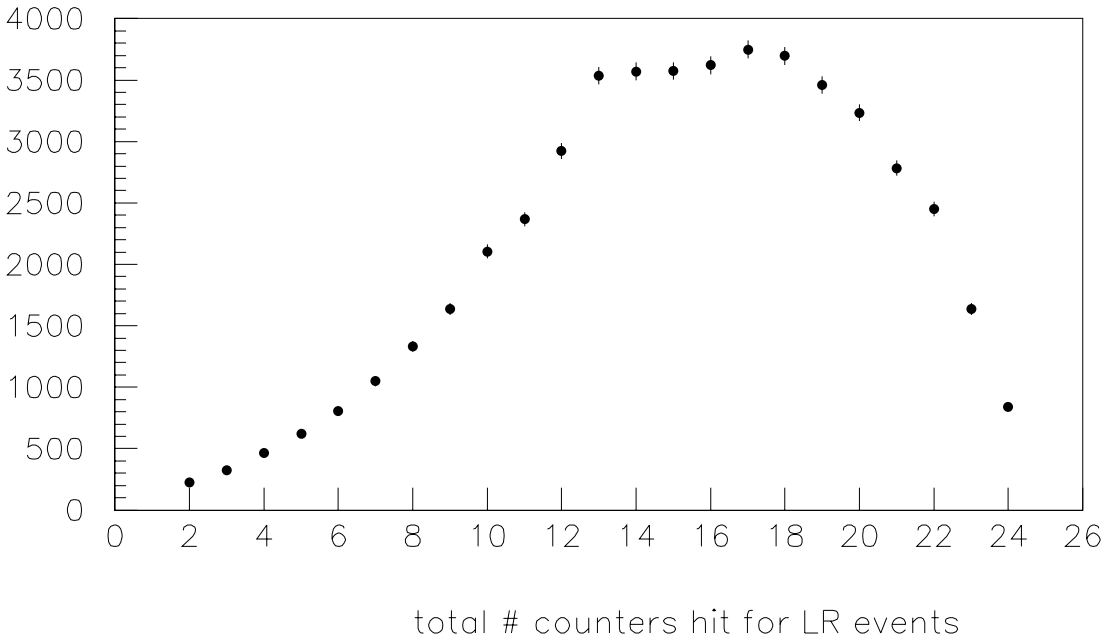

Figure 5.2: # ring counters hit for LR events.

5.2 Position of Interaction Point

The distance of each ring counter from the interaction point can be determined from the difference in timing between the early and late peaks in its TDC distribution (see Figure 5.3). The TDC distribution is obtained from events recorded with the OO trigger. In data set 10 we had as part of the master trigger a trigger for single arm events which improved statistics. The LR trigger has a hardware

veto for events with early timing (see Section 5.4) and therefore cannot be used for this particular measurement.

If d_i is the distance to the interaction point of counter i and if we denote the speed of light as c, then:

$$d_i = \frac{c}{2} * (|TDC_i^P - TDC_i^{\overline{P}}|) \tag{5.2}$$

TDC_i^P and $TDC_i^{\overline{P}}$ are the mean values obtained after fitting each peak (proton and antiproton peaks) in the TDC distribution to a gaussian. Since the TDC's readout is obtained as TDC channels we have to previously calibrate each TDC to know the conversion of $channels/ns$ (in average we obtain that 1 TDC channel $\approx$ 0.25 ns).

Table 5.1 shows the distances for each location with respect to the interaction point for data set 10. Also in this table is the measurement we did by ruler using the surveying mark where the Accelerator staff predicted the position of the E0 interaction point.

If we average the differences between TDC information and ruler (by weighting to the distances obtained by TDCs) from Table 5.1 we obtain that the L counters are predicting the interaction point to be shifted by 14.4$\pm$3.8 cm towards the L side from the surveying point and that the R counters are predicting a shift in the same direction of 39.3$\pm$3.8 cm. If we average these two numbers we conclude that the interaction point is shifted by 26.9$\pm$12.0 cm towards the L side from the the E0 surveying point in the Tevatron for data set 10. The statistical error to find the distance of each independent counter was about 0.5 cm, we added to the average of the 4 counters at the same place a systematic error of 2.0 cm due to the fact that the counters at the same place could be shifted one from the other. The error

in the ruler measurement was estimated to be about 3.0 cm. Table 5.2 shows the shifts found for the interaction point with respect to the E0 surveying mark for each of our data sets.

Notice that the shift in the interaction point causes a change in the value of the effective lengths since they were calculated assuming the interaction point to be at the surveying mark. The change of the effective lengths because this shift can be obtained by using equation A.11 with the values given in equations A.13 and A.14 (see appendix A). Table 5.2 shows the changes in the effective distances as a consequence of the shift of the interaction point. The change for detectors 1 and 2 is always smaller than 0.5%, this error is still consistent with the 1.2% error we are quoting for the values of the effective lengths.

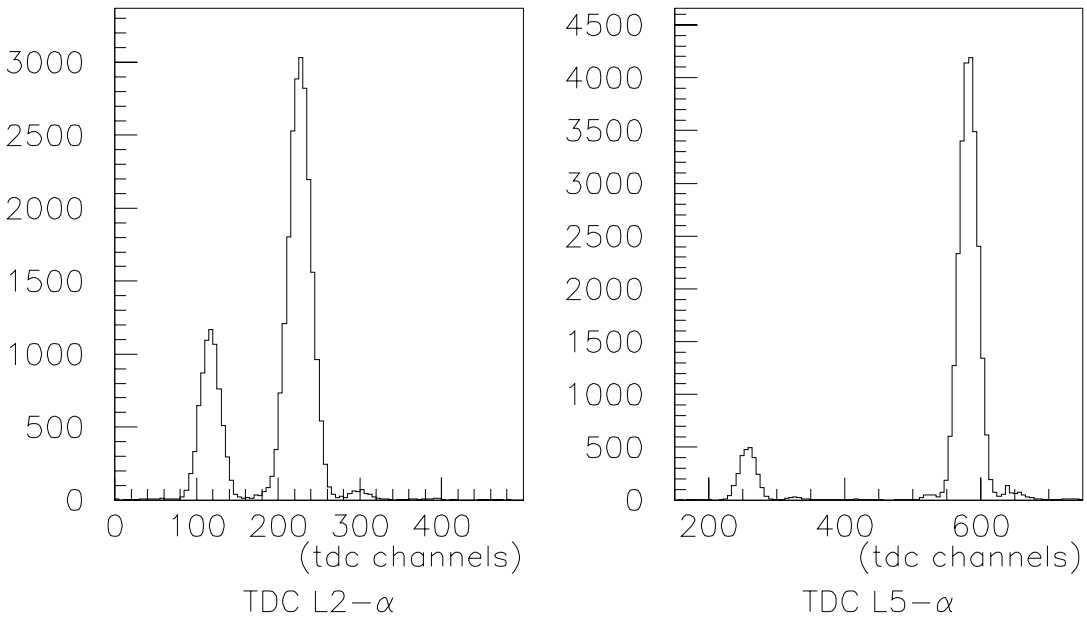

Figure 5.3: TDC early and late peaks for L_2 and L_5 counters.

Table 5.1: Distance of each counter location from the interaction point as measured by TDC information and compared to a ruler measurement that uses the E0 surveying point as reference.

counter	distance(cm) using TDCs	distance(cm) using ruler	Δ distance(cm) (TDC-ruler)
L_0	192.4±2.4	195.7±3.0	-3.3±3.8
L_1	270.4±2.3	289.7±3.0	-19.3±3.8
L_2	415.1±2.3	437.2±3.0	-22.1±3.8
L_3	722.2±2.4	734.5±3.0	-12.3±3.8
L_4	981.4±2.2	998.5±3.0	-17.1±3.7
L_5	1231.3±2.2	1242.9±3.0	-11.6±3.7
R_1	339.1±2.3	307.5±3.0	31.6±3.8
R_2	480.3±2.4	457.5±3.0	22.8±3.8
R_3	682.8±2.4	653.2±3.0	29.6±3.8
R_4	1028.3±2.2	988.7±3.0	39.6±3.7
R_5	1297.7±2.2	1245.4±3.0	52.3±3.7

Table 5.2: Shift of the interaction point from the ideal point for each of our data sets (positive shift is towards the L counters) and change in the effective lengths due to this shift. Negative % means the value gets reduced.

store	data set	E0 point shift(cm)	$\frac{\delta Leff_{Y1}}{Leff_{Y1}}(\%)$	$\frac{\delta Leff_{X1}}{Leff_{X1}}(\%)$	$\frac{\delta Leff_{Y4}}{Leff_{Y4}}(\%)$	$\frac{\delta Leff_{X4}}{Leff_{X4}}(\%)$
1	1,2,3,4	50.4±12.0	-0.45±0.11	0.52±0.12	0.01±0.00	-1.15±0.27
2	5,6	16.4±12.0	-0.15±0.11	0.17±0.12	0.00±0.00	-0.38±0.27
3	7,8,9	49.7±12.0	-0.44±0.11	0.52±0.12	0.01±0.00	-1.14±0.27
4	10	26.9±12.0	-0.24±0.11	0.28±0.12	0.01±0.00	-0.62±0.27

5.3 Pseudorapidity Coverage

Using the distances obtained from the TDC information and knowing that all the counters have a height of 2.54 cm and that the inner diameter of all the counters is 10.16 cm, except counters L_5 and R_5 which have an inner diameter of 7.62 cm (see Section 2.6), we can determine the pseudorapidity range ($\eta = -\ln(\tan(\frac{\theta}{2}))$) covered by each ring counter. Table 5.3 shows the values of η_{min} and η_{max} covered by the ring counters.

Table 5.3: Pseudorapidity coverage of our inelastic counters.

counter	θ_{min}(rad)	θ_{max}(rad)	η_{min}	η_{max}
L0	0.02648	0.03971	3.92	4.32
L1	0.01874	0.02810	4.27	4.67
L2	0.01221	0.01831	4.69	5.10
L3	0.00704	0.01057	5.24	5.65
L4	0.00518	0.00777	5.55	5.96
L5	0.00310	0.00517	5.96	6.47
R1	0.01498	0.02247	4.49	4.89
R2	0.01057	0.01585	4.84	5.24
R3	0.00744	0.01116	5.19	5.59
R4	0.00494	0.00741	5.60	6.00
R5	0.00294	0.00489	6.01	6.52

5.4 Early Veto Correction

The Logic diagram in Figure 2.15 shows that before making the coincidence of the R_{3-5} signal to the RF ($R_{3-5} = R_3 + R_4 + R_5$) the signal is made 200 ns wide and then clipped into a pulse 32 ns wide. The consequence of this is to produce a 200 ns dead time after R_{3-5} fires. The difference in timing between the early and late peaks for the farthest ring counter from the interaction point (R_5) is about 88 ns,

then in cases where there is a pulse with early timing, i.e. a particle associated with the $\overline{P}$ beam, in one of the R_3 or R_4 or R_5 counters and there is on the same beam crossing a pulse within the late peak in another counter of the same set, i.e. a particle whose timing is consistent with coming from an interaction at E0, the pulse with the late timing would be vetoed. So even if there is a noisy counter that produces an early pulse and all other counters get hit with a good event, that event would not be counted. Identical logic was made for the L_{3-5} signal. The reason to make the logic in this way was to reduce the accidental background in the LR trigger; any antiproton-gas scattering that produces a pulse with early timing in the R_{3-5} counters has a good probability of producing a pulse with the late timing in the L_{3-5} counters. The same happens with proton-gas scattering, it can produce an early pulse in the L_{3-5} counters and a late pulse in the R_{3-5} counters. Since both of these contributions to the LR trigger could be much larger than having a counter hit with an early timing and a counter at the same side hit with a late timing in the same interaction, it is better to veto the early hits in the ring counters at both sides of the interaction point and correct in software for the good events that got vetoed because one counter had a hit with the early timing.

Any hit recorded in one ring counter with earlier timing than the late TDC peak should be uncorrelated to a hit in another ring counter at the same side from the interaction point that has its timing consistent with the TDC late peak. Then the probability of having both of these types of events happening in the same interaction is the product of the probabilities of each one happening. If we can measure the probability for an early hit to occur, then the correction factor to apply to the number of LRs we count in software would be $\frac{1}{1-Probability(early)}$. The

probability for an early hit to occur in the ring counters that make the LR trigger can be measured by using elastic triggers; since the OO triggers are uncorrelated to the early hit events happening in the ring counters, we look at every OO trigger in each run and count the number of times there is an early hit in ring counters 3,4 or 5 at both sides of the interaction point. These probabilities are listed in Table 5.4. Data set #10 does not have an entry in this table because we are not measuring the number of LR events in this set due to some camac readout problems that occurred during the data taking for that set of runs. Typical corrections are about 1.5%.

Table 5.4: Early veto correction for LR events.

data set #	$\frac{\#(L_{3-5}+R_{3-5})_{early}}{\#OOs}(\%)$
1	1.702±0.057
2	1.154±0.028
3	1.240±0.029
4	2.082±0.024
5	1.429±0.018
6	1.295±0.022
7	1.982±0.064
8	1.362±0.014
9	1.611±0.029

5.5 LR Accidentals

Even after the hardware early veto is applied, there is a probability of getting an LR trigger from two uncorrelated events that were produced most likely by pbar-gas scattering on the L (left) side and proton-gas scattering on the R (right) side. Pbar-gas scattering on the L side can only produce hits on the R side with timing much greater than the TDC window we apply for good E0 interactions, so that

it will overflow the TDC on the R_{3-5} counters, these hits are expected to be of low probability because it involves backward production of particles in a 900 GeV fixed target collision; similarly, proton-gas scattering on the R side can produce a hit on the TDC late peak for the R counters but can only produce a hit with timing much greater than the TDC window that we apply on the L counters for the late peak and also overflows the TDCs for the L_{3-5} counters.

We call L events all events that have at least one ring counter L_{3-5} hit within the late TDC peak, and consistent with a minimum ionizing particle, and have no ring counters R_{3-5} hit on the late or early TDC peaks. Similarly, we can define an R event as one having at least one ring counter R_{3-5} hit within the late TDC peak, which survives ADC cuts, and has no ring counter L_{3-5} hit on the late or early TDC peaks. The probability of getting an LR accidental event from beam-gas scattering products at both sides of the interaction point would be the product of the probability for an L event times the probability for getting an R event. Since OO triggers are very much uncorrelated to L, R or LR events (see Section 5.6) we can look at events when the experiment was triggered by an OO trigger and determine the ratios of $\frac{L}{LR}$ and $\frac{R}{LR}$ events. With these ratios and with the condition that L and R events are uncorrelated, we can determine the fraction of accidental LRs to the number of LRs we determine with the event selection described in Section 5.1. Because the probability of having an L,R or LR event with an OO is very low, to improve statistics we add all the runs within the same store and find an average percentage of LR accidentals during the store. Table 5.5 shows the percentage of LR accidentals for each store.

Table 5.5: % of LR accidentals in each store.

Store	data sets on the store	%LR accidentals
1	1,2,3,4	1.6±0.3
2	5,6	1.9±0.4
3	7,8,9	2.4±0.5

5.6 Inelastic Event Contamination on the Elastic Sample

Because our elastic detectors cover the pseudorapidity range of $9.2 < \eta < 11$ (i.e. scattering angles from 33 μrad to 200 μrad) and because of the presence of dipole magnets between our elastic detectors and the interaction point we would expect a very low probability of having a hit on our elastic detectors caused by an inelastic event. Because of the η coverage a negligible amount of inelastics produced in this range is expected and the dipole magnets sweep out any products of secondaries produced by interaction of particles with the beam pipe or any other material near the E0 interaction point. The other possibility is to have an elastic event and an inelastic event produced in the same bunch crossing, and the question is if we tag the event as an inelastic or an elastic. However, because the heavy scraping done to be able to get our detectors as close as possible to the beam we ended up with such low luminosities that the probability to have two different interactions in the same crossing is negligible. We can verify this from our data. We can determine the fraction of elastic candidate events that also have an inelastic candidate event in the ring counters. We look at OO triggers and make all the requirements for an elastic event, including XX and YY diagonal cuts and then look at the ring counters and count how many times we can also tag an LR or an L or R event. We have found that the probability of finding an elastic candidate event with an

L or an R event is 0.11±0.02% and the probability of finding an elastic event with an LR event is 0.0±0.3%.

5.7 LR Acceptance

We only use counters L_3, L_4, L_5 and R_3, R_4, R_5 to identify double arm events. The η coverage of these counters is shown in table 5.3. Because of the limited range of pseudorapidity covered by the LR trigger ($5.2< \eta <6.5$) we expect to be inefficient in identifying every double arm event produced at our interaction point and therefore we need to determine what is the acceptance for the LR trigger. References [5] and [56] have studied the secondary charged particle distribution for non diffractive events for η <3.5 at this energy. It was observed that this distribution was fairly flat with a value of $\frac{dN_{ch}}{d\eta} \approx 4.0$. At $\sqrt{s}$=1.8 TeV it is expected that $\frac{dN_{ch}}{d\eta}$ starts falling linearly from $\eta \approx 4.0$ to $\eta \approx 8.0$ where it becomes 0 (see [6], [7]). Figure 5.4 shows the measurements from [5] and a montecarlo simulation obtained by [52] at this energy, however we need also to consider the interactions of the secondaries produced at E0 with the Tevatron beam pipe material. The effect expected on the $\frac{dN_{ch}}{d\eta}$ distribution observed by our inelastic counters is to have a less steep slope in the region of η where $\frac{dN_{ch}}{d\eta}$ decreases linearly. This is because, for counters at higher η values, the probability of interaction of a particle produced at E0 with the beam pipe is higher because its scattering angle is smaller and it has to go through more Tevatron beam pipe material before reaching the counter. The ring counters that make the LR trigger are placed in the η region where $\frac{dN_{ch}}{d\eta}$ is linearly decreasing (Figure 5.4) . If we include more ring counters located at lower η in the LR definition and if we assume that the hits in the ring counters are poisson distributed we can approximate the contribution of every counter to

the inefficiency of the LR trigger to be $\exp(-\lambda_i * \Delta\eta)$, where $\lambda_i * \Delta\eta$ is just the extra number of secondary charged particles caught with the new counter i ; λ_i is related to $\frac{dN_{ch}}{d\eta}$ for each particular counter. We expect λ_i to increase with each extra counter we add to the LR trigger at low η, i.e. $\lambda_0 > \lambda_1 > \lambda_2$ since L_0 is at a denser η region than L_1 and L_2.

One way to determine the efficiency of arm L_{3-5} of the LR trigger is by counting the number of hits observed by L_{3-5} and comparing that to the number of hits observed by $L_{0-5} = L_0 + ... + L_5$, that is if we added counters L_0, L_1 and L_2 to the LR trigger. If L_{0-5} was 100 % efficient (i.e. had 100then the ratio $\frac{L_{3-5}}{L_{0-5}}$ would give the acceptance for the arm L_{3-5}, but we do not know if L_{0-5} is 100% efficient. If L_{0-5} has an inefficiency of ξ_0 and if N_0 is the number of LR events observed by L_{0-5} then the total number of LR events would be $N_t = \frac{N_0}{1-\xi_0}$ and the efficiency of any set of counters forming the left arm would be $eff_i = \frac{N_i*(1-\xi_0)}{N_0}$ where N_i is the number of LRs detected by that set of counters. We used data from runs where we had the single arm triggers as part of the master trigger and counted the number of LR events by each consecutive set of counters forming the left arm when the single arm R trigger prescaler fired. The distribution of counters hit for the Left arm events did not change by changing the requirements of the right arm (like for example requiring R_1 always to be hit or requiring R_5 always to be hit) which shows that left and right arms are independent. Table 5.6 shows the number of hits obtained by each set of counters defining the left arm. To estimate the inefficiency of L_{0-5} we do a semilog plot of $ineff_i$ vs η for different values of ξ_0(ξ_0 is the inefficiency of L_{0-5}), see Figure 5.5, even though we cannot determine precisely the value of ξ_0 we can give limits to it with the argument that the slope

of the inefficiency when going from L_{3-5} to L_{2-5} has to get steeper and the same with the slope when going from L_{2-5} to L_{1-5} and L_{1-5} to L_{0-5} because we are adding counters in a denser region of η. From Figure 5.5 we see that an inefficiency of L_{0-5} of $\xi_0 = 2\%$ produces a continuous drop in the inefficiency as a function of η and the inefficiency slopes are about the same when adding counters L_2 and L_1 and L_0, the slopes get much steeper in the case of $\xi_0 = 0.1\%$ Therefore we claim that the inefficiency of L_{0-5} has to be within these two limits and we quote

$$L_{0-5} inefficiency(\xi_0) = 1.0 \pm 1.0\% \tag{5.3}$$

The reason for not locating counters at lower η values than L_0 counter is because the TDC peaks for early and late particles overlap, since these counters would have ended up very close to the interaction point. The overlap makes it hard to identify whether or not a hit was produced by a particle produced at the interaction point or by a background source. From table 5.6 we know that $\frac{L_{3-5}}{L_{0-5}} = 94.98 \pm 0.18\%$ and with our estimate for the inefficiency of L_{0-5} we obtain that

$$L_{3-5} efficiency = \frac{L_{3-5}}{1.01 * L_{0-5}} = 94.04 \pm 1.0\% \tag{5.4}$$

Since left and right arms are independent we have that LR efficiency is the square of the efficiency of L_{3-5}

$$LR efficiency(f) = 88.4 \pm 2.0\% \tag{5.5}$$

The value of the efficiency of LR we have estimated with the above reasoning agrees with the value of 88.3 $\pm$2.44 % measured by E710 who used the same geometry for the inelastic counters ([2]).

Table 5.6: #LR events observed in the left arm counters.

counters forming the left side	#LR events observed	η range covered
L_{0-5}	15371	$3.92 < \eta < 6.47$
L_{1-5}	15170	$4.27 < \eta < 6.47$
L_{2-5}	14911	$4.69 < \eta < 6.47$
L_{3-5}	14600	$5.24 < \eta < 6.47$
L_{4-5}	13829	$5.55 < \eta < 6.47$
L_5	12317	$5.96 < \eta < 6.47$

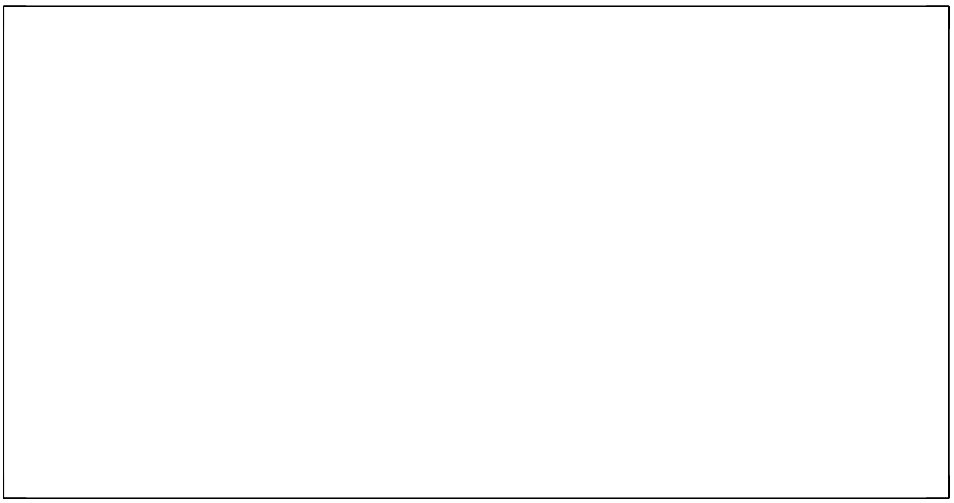

Figure 5.4: Pseudorapidity distribution for non diffractive events at $\sqrt{s} = 1800$ GeV from reference [52].

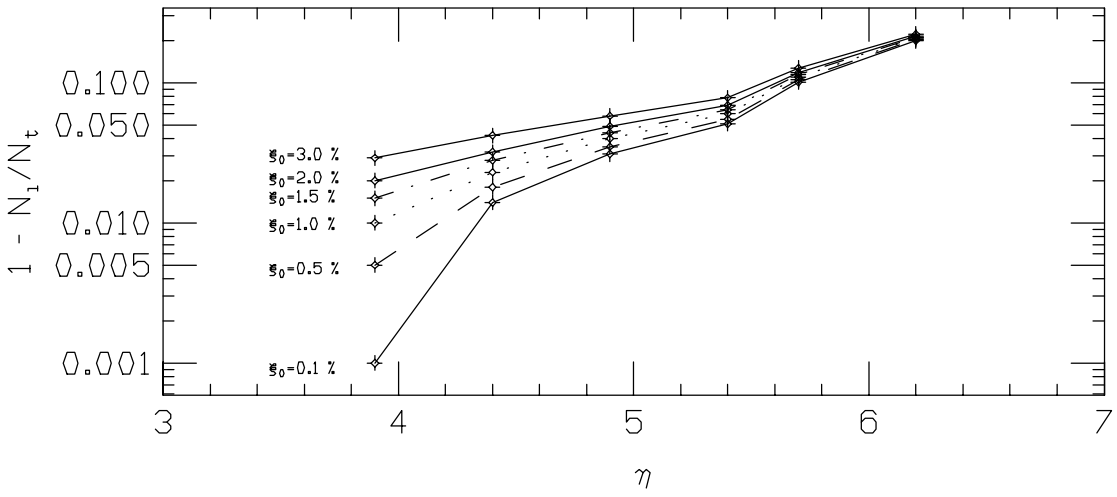

Figure 5.5: Plot of left arm inefficiencies vs η for different values of ξ_0(ξ_0=inefficiency of L_{0-5}).

CHAPTER 6

Results and Discussion

Table 6.1 shows the values of $\left(\frac{dN}{dt}\right)_{t=0}$, the number of LR events, $\frac{LR}{\left(\frac{dN}{dt}\right)_{t=0}}$ and the ratio of number of elastics between detector combination 2-3 and detector combination 1-4 for each of our data sets (see also Figure 6.1). Data set 10 does not have entries for LR events because we did not measure them for that run, however that run was still very useful for diagnostic purposes. Because the inelastic triggers have different live time that the elastic triggers (see Section 2.7.5), the value of LR events given in table 6.1 have been multiplied to the ratio of live times of elastic to inelastic triggers (values of live times for each trigger are found in Table 2.5).

We expect that after all corrections have been applied the number of elastics from detector combination 1-4 to be the same as for combination 2-3. The weighted average over the 10 data sets gave:

$$\begin{aligned} \frac{N_{el23}}{N_{el14}} &= 1.011 \pm 0.014 \\ \chi^2/d.f. &= 0.968 \end{aligned} \tag{6.1}$$

The weighted average of the first 9 data sets for the ratio $\frac{LR}{\left(\frac{dN}{dt}\right)_{t=0}}$ is

$$\begin{aligned} \frac{LR}{\left(\frac{dN}{dt}\right)_{t=0}} &= 0.1596 \pm 0.0014 \\ \chi^2/d.f. &= 0.936 \end{aligned} \tag{6.2}$$

Table 6.1: #LR events, $\left(\frac{dN}{dt}\right)_{t=0}$, $\frac{LR}{\left(\frac{dN}{dt}\right)_{t=0}}$ and ratio of elastics from detector combination 2-3 to detector combination 1-4.

data set #	LR	$\left(\frac{dN}{dt}\right)_{t=0}$	$\frac{LR}{\left(\frac{dN}{dt}\right)_{t=0}}$	$\frac{N_{el23}}{N_{el14}}$
1	87050.8	559173.6	0.156±0.004	0.99±0.05
2	66431.6	427505.2	0.155±0.005	0.98±0.05
3	56764.8	362260.3	0.157±0.005	0.98±0.06
4	177413.3	1140380.8	0.156±0.003	1.05±0.04
5	272180.7	1661018.6	0.164±0.003	1.06±0.04
6	116031.6	719107.8	0.161±0.005	1.06±0.06
7	17050.8	105482.1	0.162±0.010	1.01±0.12
8	134689.2	817060.7	0.165±0.004	1.06±0.05
9	50306.0	316496.9	0.159±0.006	1.09±0.09
10		2396926.3		0.99±0.02

Fitting simultaneously all 10 data sets we obtained the following B value, as in equation 4.19:

$$\begin{aligned} B &= 17.31 \pm 1.47\ (GeV/c)^{-2} \\ \chi^2/d.f. &= 0.84 \end{aligned} \tag{6.3}$$

Table 6.2 shows the values of σ_T, σ_{el} and σ_{in} with their statistical errors for the first 9 data sets after the set of equations 3.16, 3.17, 3.18 and 3.19 is solved simultaneously as explained in Section 3.5. The same data are also plotted in Figures 6.2 and 6.3.

The weighted averages for σ_T, σ_{el} and σ_{in} are shown below

$$\begin{aligned} \sigma_T &= 69.82 \pm 0.56\ mb \\ \chi^2/d.f. &= 0.853 \end{aligned} \tag{6.4}$$

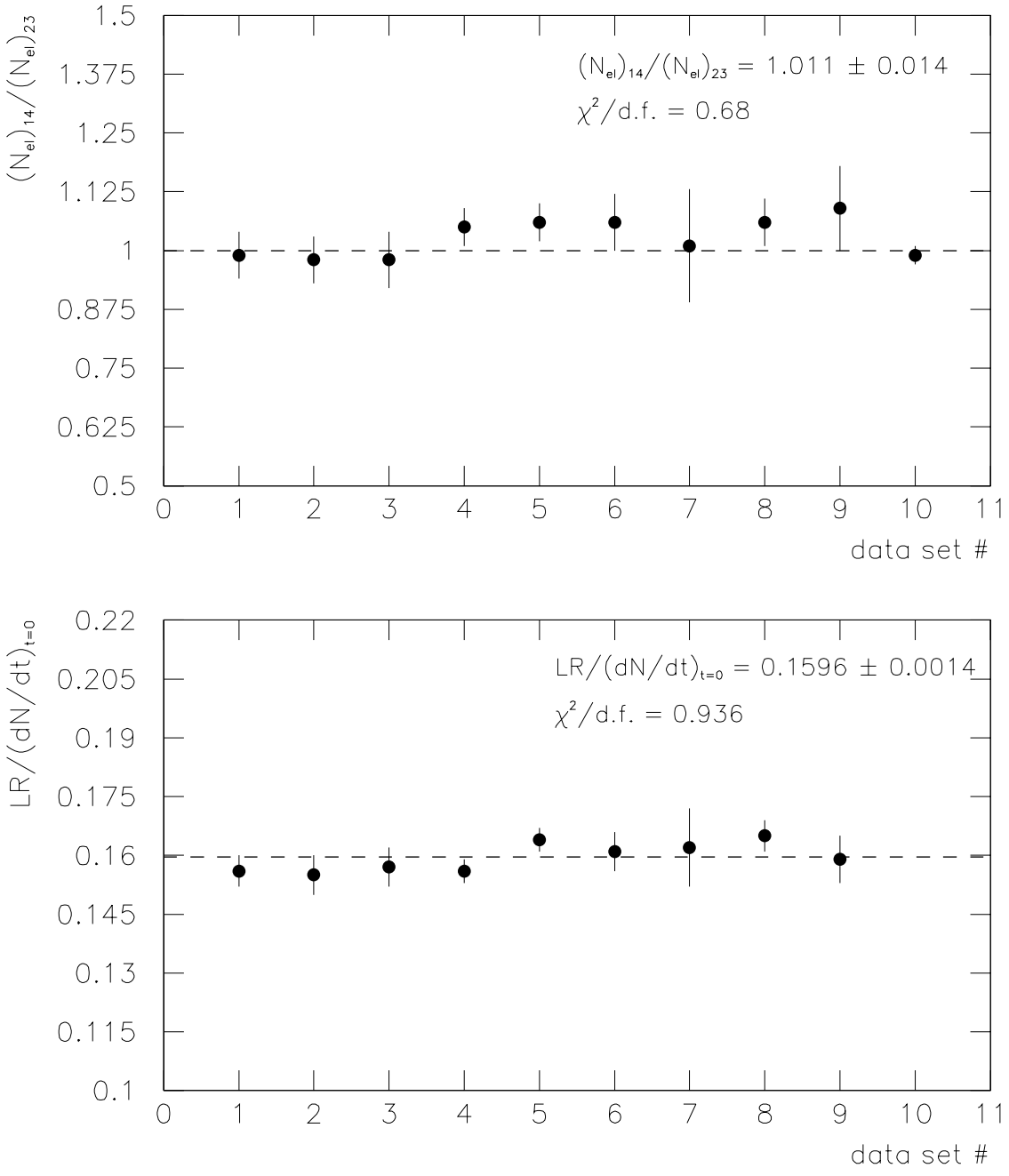

Figure 6.1: Ratio of elastics from detector combination 2-3 to detector combination 1-4 and $\frac{LR}{\left(\frac{dN}{dt}\right)_{t=0}}$.

Table 6.2: σ_T, σ_{el} and σ_{in} for each data set (statistical errors only).

data set #	σ_T (mb)	σ_{el} (mb)	σ_{in} (mb)
1	71.41± 1.78	15.65± 0.78	55.76± 1.00
2	71.52± 1.88	15.70± 0.83	55.82± 1.06
3	71.00± 2.16	15.47± 0.94	55.53± 1.22
4	71.45± 1.30	15.66± 0.57	55.78± 0.73
5	68.25± 1.06	14.29± 0.44	53.95± 0.62
6	69.19± 1.78	14.69± 0.76	54.50± 1.02
7	69.46± 3.85	14.80± 1.65	54.65± 2.21
8	68.25± 1.57	14.30± 0.66	53.96± 0.91
9	70.12± 2.49	15.09± 1.07	55.03± 1.41

$$\sigma_{el} = 14.93 \pm 0.24\ mb \tag{6.5}$$
$$\chi^2/d.f. = 0.855$$

$$\sigma_{in} = 54.88 \pm 0.32\ mb \tag{6.6}$$
$$\chi^2/d.f. = 0.850$$

The systematic errors are evaluated in Table 6.3. The main two sources for systematics are the uncertainty in the effective lengths and the uncertainty in the LR acceptance. Other systematics were evaluated considering extreme cases like considering the background subtraction to be off by 5% (which we evaluated by three different methods always agreeing within statistics) or ΔH_{12} (the vertical separation between toe counters 1 and 2) to be off by 300 μm which is expected to be known with a precision of 30 μm.

Adding statistical and systematic errors in quadrature the final results are:

$$\sigma_T = 69.82 \pm 2.44\ mb \tag{6.7}$$

$$\sigma_{el} = 14.93 \pm 1.03\ mb \tag{6.8}$$

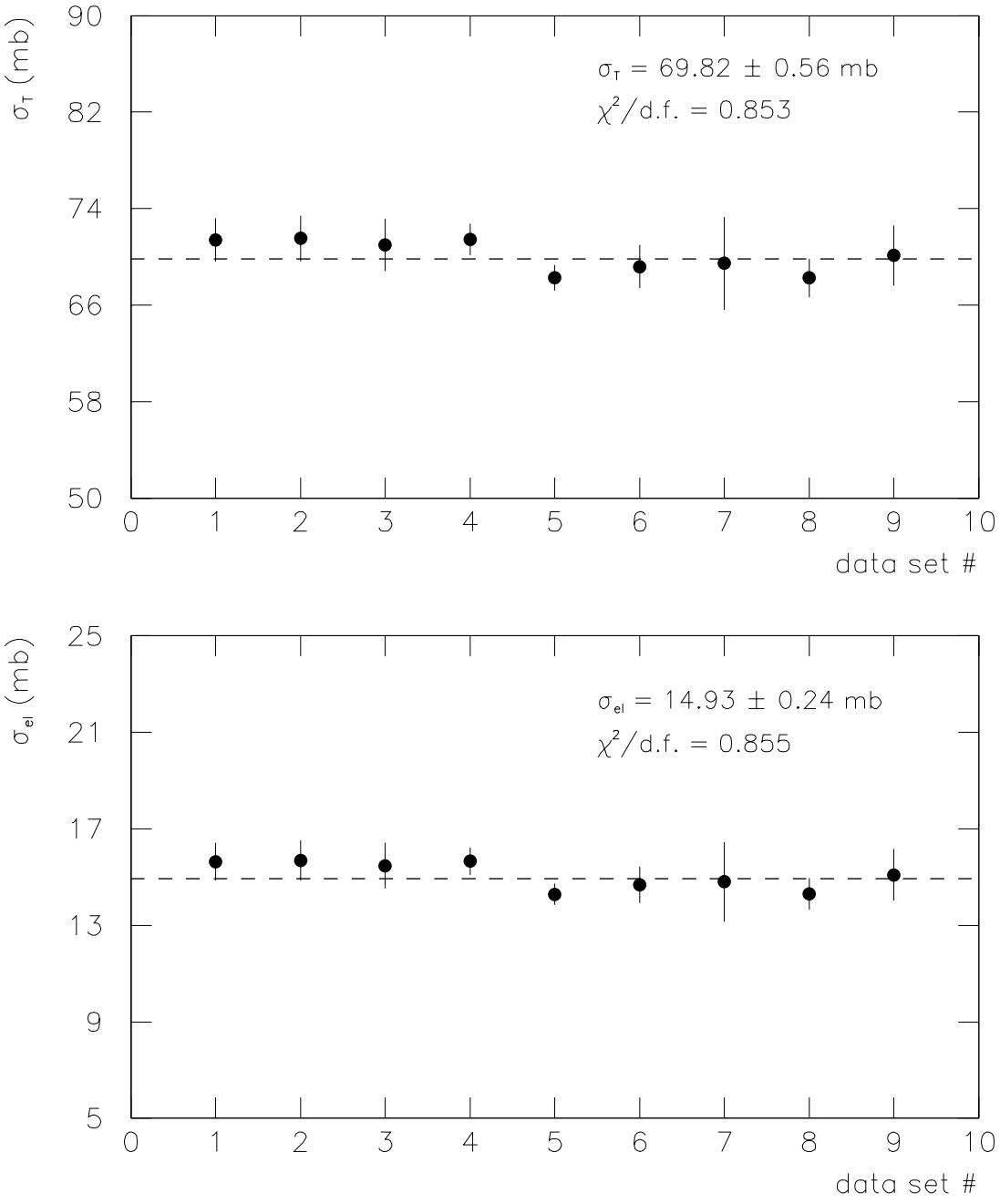

Figure 6.2: σ_T, σ_{el} for each data set.

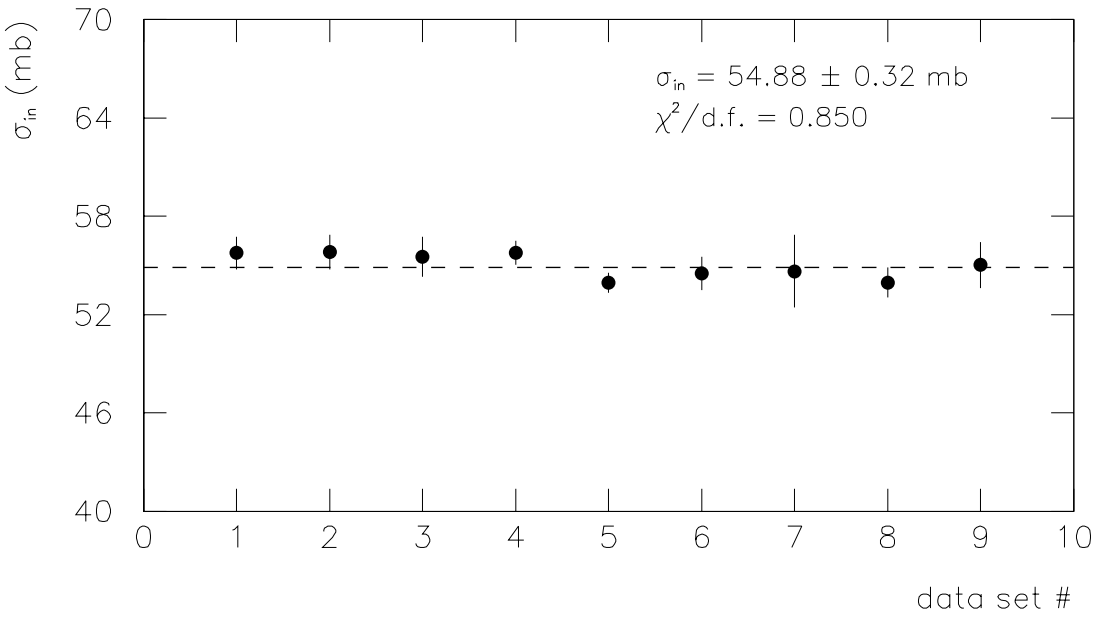

Figure 6.3: σ_{in} for each data set.

Table 6.3: Systematic errors.

error source	$\Delta\sigma_T(mb)$	$\Delta\sigma_{el}$ (mb)	$\Delta\sigma_{in}$ (mb)
error in LR accept. (LR_{acc}=88.4±2.0 %)	1.38	0.59	0.78
error in σ_{sd} ($\langle\sigma_{sd}\rangle$ = 9.452±0.419 mb)	0.53	0.23	0.30
error in B ($\langle B\rangle$ = 16.99±0.22$(GeV/c)^{-2}$)	0.39	0.03	0.41
error in L_{effX1} (45.757±0.915 m)	1.12	0.48	0.64
error in L_{effY1} (80.195±1.604 m)	1.12	0.48	0.64
vertical beam position (off by 200 μm)	0.02	0.01	0.01
horizontal beam position (off by 200 μm)	0.14	0.06	0.08
error in X coordinate calibration (0.5 %)	0.24	0.10	0.14
error in Y coordinate calibration (0.5 %)	0.29	0.13	0.18
error in ΔH_{12} (off by 300 μm)	0.40	0.15	0.20
error in LR accidentals (0.5 %)	0.34	0.15	0.19
error in early veto correction (0.5 %)	0.34	0.15	0.19
error in Background subtraction(5.0 %)	0.46	0.20	0.26
total systematic error	2.37	1.0	1.39

$$\sigma_{in} \quad = \quad 54.88 \pm 1.43 \; mb \tag{6.9}$$

Figures 6.4 and 6.5 show our measurements compared to the world data. (Figure 6.4 was obtained from references [13] - [26]; Figure 6.5 was obtained from references [13] - [21]). Our measurement of the total cross section agrees with the E710 value within 1 standard deviation but disagrees with the CDF measurement by more than 3 standard deviations. Even though in our analysis we are fixing σ_{sd} cross section to a value (σ_{sd}=9.452±0.419) which is very close to the CDF measurement (σ_{sd}=9.46±0.44) we measured an inelastic cross section which is 5.4 mb lower than what CDF has measured (σ_{in}=60.33±1.40 mb) which is about 2.7 standard deviations difference. Our value of σ_{in} agrees better with the E710 measurement (σ_{in}=55.5 ± 2.2 mb). Our elastic cross section measurement is lower than the E710 value (σ_{el}=16.6±1.6) by 1.7 mb (but still within 1 standard deviation) and lower than the CDF measurement (σ_{el}=19.7±0.85 mb) by 4.8 mb which

is more than 3 standard deviations away.

One of the main sources of systematics might be reduced by further analysis of E811 data. Analyzing the missing bunch data that e811 took and has not been fully analyzed yet will reduce the error in the LR acceptance (and might provide a new measurement of σ_{sd}). Analysis of the data in the nuclear-coulomb interference region might give as a result a new measurement of ρ at $\sqrt{s}$=1800 GeV with smaller uncertainty than the measurement done by E710 experiment.

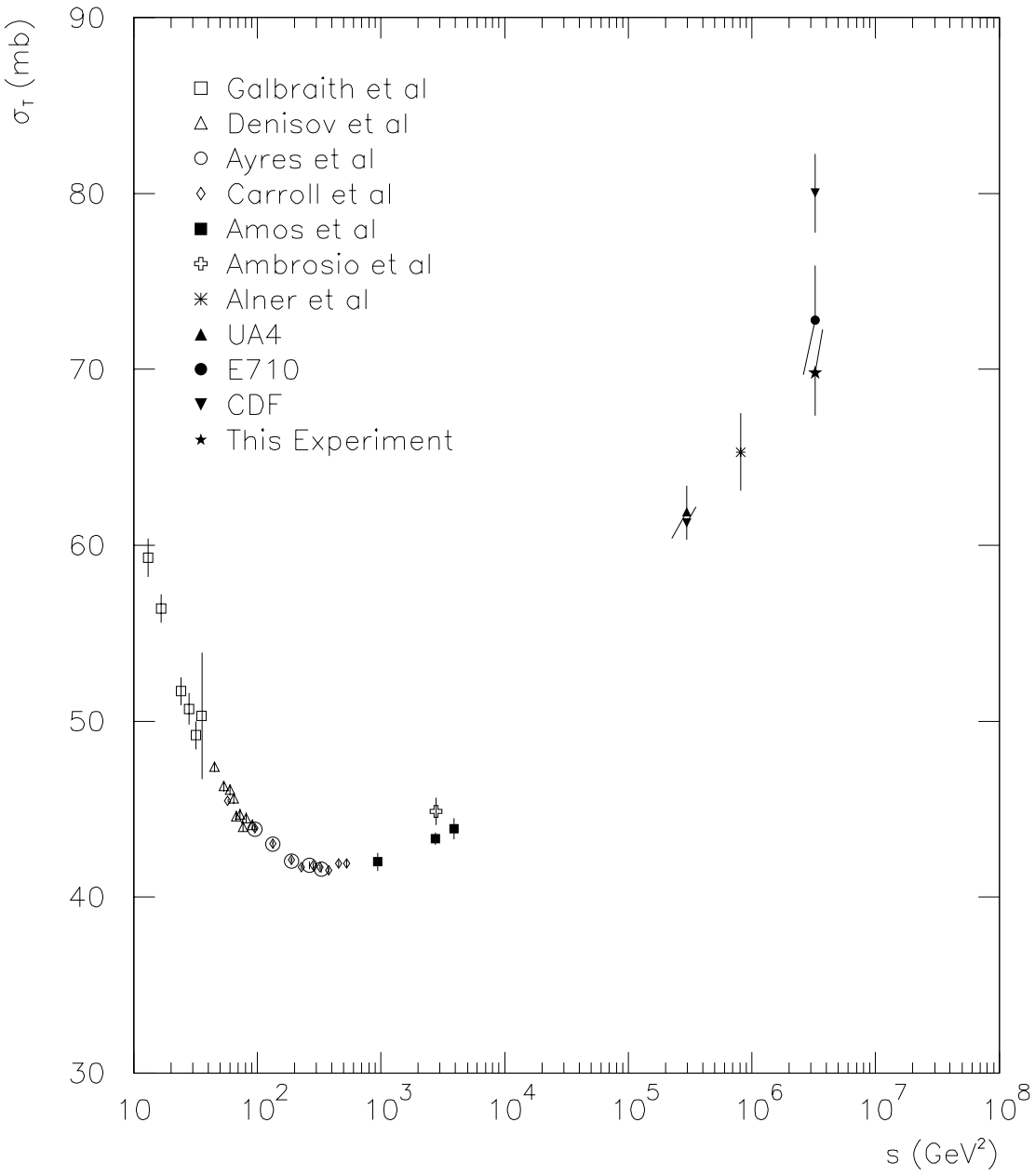

Figure 6.4: Our measurement of $P\overline{P}$ σ_T compared to the world data.

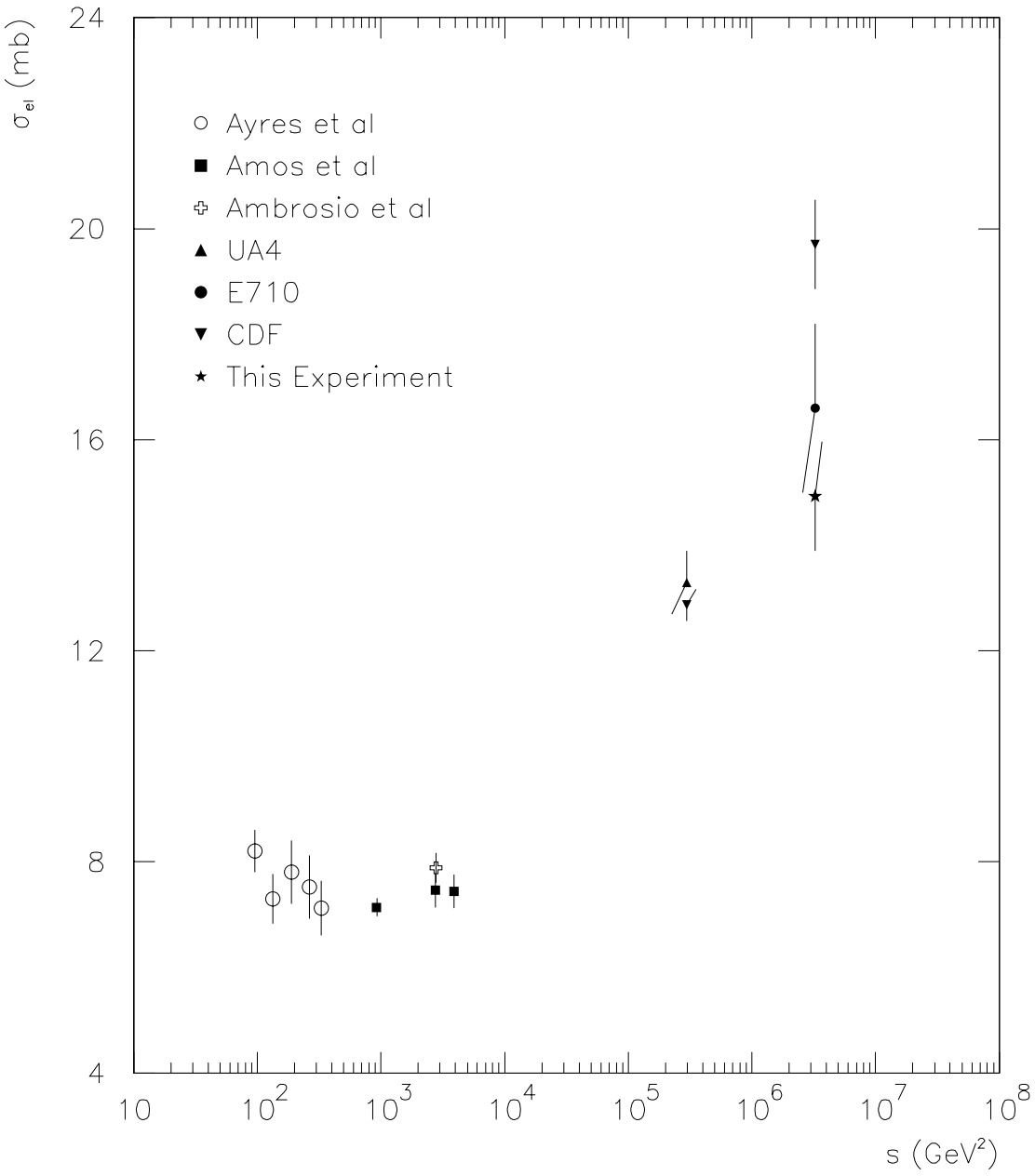

Figure 6.5: Our measurement of $P\overline{P}$ σ_{el} compared to the world data.

APPENDIX A

The Beam Optics

The equation of motion of a particle trapped in the accelerator orbit by the alternate magnetic gradient can be written as:

$$\frac{d^2y}{dz^2}+k(z)y=0 \tag{A.1}$$

Where y is the vertical displacement relative to the reference orbit, and z is the longitudinal displacement. k(z) is related to the gradient of the magnetic field and is also periodic (k(z) = k(z+L) where L is the circumference of the accelerator). The general solution to equation A.1 is

$$y(z) = A\sqrt{\beta(z)}cos\left(\psi(z) - \psi_0\right) \tag{A.2}$$

where A and ψ_0 are constants of integration. $\psi(z)$ is not a single valued function $\psi(z) \neq \psi(z + L)$. $\psi(z)$ is related to β as:

$$\frac{d\psi}{dz} = \frac{1}{\beta} \tag{A.3}$$

There is a conserved quantity in equation A.1:

$$\frac{y^2 + \left(\beta y' + \alpha y\right)^2}{\beta} = A^2 \tag{A.4}$$

where $y' = \frac{dy}{dz}$ and

$$\frac{d\beta}{dz} = -2\alpha \tag{A.5}$$

α, β and ψ are called the accelerator lattice functions whose values are related to the magnets located along the accelerator circumference. By using equation A.2 one can write the position and angle of a particle at any place in the Tevatron lattice with respect to the position and angle at another location in the lattice:

$$\begin{pmatrix} y_1 \\ y_1' \end{pmatrix} = M_{01} * \begin{pmatrix} y_0 \\ y_0' \end{pmatrix} \tag{A.6}$$

$$M_{01} = \begin{bmatrix} (\beta_1/\beta_0)^{1/2}(cos\Delta\psi + \alpha_1 sin\Delta\psi) & (\beta_0\beta_1)^{1/2} sin\Delta\psi \\ -(1 + \alpha_0\alpha_1 sin\Delta\psi + \alpha_0\alpha_1 cos\Delta\psi)/(\beta_0\beta_1) & (\beta_0\beta_1)^{1/2}(cos\Delta\psi - \alpha_1 sin\Delta\psi) \end{bmatrix} \tag{A.7}$$

where $\Delta\psi = \psi_1 - \psi_0$ is the phase advance between locations z_0 and z_1. Matrix M_{01} is usually written as a 4 x 4 matrix to include also x and x'. The coupling between x and y coordinates in the above analysis is assumed to be 0. In reality it is not 0 but still very small. From equation A.7 we can write:

$$y_1 = m_{01} * y_0 + L_{yeff01} * \theta_y \tag{A.8}$$

$$m_{01} = (\beta_1/\beta_0)^{1/2}(cos(\Delta\psi) - \alpha_1 sin(\Delta\psi)) \tag{A.9}$$

$$L_{yeff01} = (\beta_0\beta_1)^{1/2} sin(\Delta\psi) \tag{A.10}$$

L_{eff01} is the effective distance between points z_0 and z_1. Taking the derivative with respect to z and by using equations A.5 and A.3, then a change in z distance from z_0 and z_1 by Δz will produce a change in L_{eff01} as

$$\Delta L_{eff01} = m_{01}\Delta z \tag{A.11}$$

If there are no magnetic fields in the region between these two points , then:

$$y_2 = y_1 + (z_2 - z1) * \theta_y \tag{A.12}$$

If z_0 is taken to be the E0 interaction point ($z_0 = 0$), and z_1 is taken to be the location of our elastic detectors and since the Tevatron lattice is known for our two locations, we can evaluate the matrix elements for the two different locations where we have our elastic detectors:

$$\begin{pmatrix} x_1 \\ \theta_{x1} \\ y_1 \\ \theta_{y1} \end{pmatrix} = \begin{pmatrix} 0.474 & 45.717 & 4.922x10^{-4} & 8.139x10^{-2} \\ -2.764x10^{-2} & -0.556 & -1.666x10^{-6} & 3.349x10^{-3} \\ 3.769x10^{-3} & 0.1574 & -0.714 & 80.278 \\ 1.143x10^{-4} & 5.249x10^{-3} & -2.505x10^{-2} & 1.417 \end{pmatrix} \begin{pmatrix} x_0 \\ \theta_{x0} \\ y_0 \\ \theta_{y0} \end{pmatrix} \tag{A.13}$$

$$\begin{pmatrix} x_4 \\ \theta_{x4} \\ y_4 \\ \theta_{y4} \end{pmatrix} = \begin{pmatrix} -0.717 & 31.346 & 2.216x10^{-3} & 4.855x10^{-2} \\ -2.094x10^{-2} & -0.479 & 4.537x10^{-5} & -1.293x10^{-3} \\ 9.926x10^{-4} & 0.184 & 1.657x10^{-2} & 73.871 \\ 2.402x10^{-6} & -4.662x10^{-3} & -1.394x10^{-2} & -1.780 \end{pmatrix} \begin{pmatrix} x_0 \\ \theta_{x0} \\ y_0 \\ \theta_{y0} \end{pmatrix} \tag{A.14}$$

Equations A.13 and A.14 show the matrix elements for detectors 1 and 4 (2 and 3) respectively .

APPENDIX B

The Luminosity

The luminosity can be determined from the following equation:

$$\mathcal{L} = \frac{f * N_{_P} * N_{\overline{P}} * nbnch * G}{4\pi\sigma_H\sigma_V} \tag{B.1}$$

where:

- f is the frequency of revolution of the beam (53.215 MHz).
- $N_{_P}$ is the number of protons/bunch.
- $N_{\overline{P}}$ is the number of antiprotons/bunch.
- nbnch is the number of bunches per beam.
- G is a correction factor due to the longitudinal spread of the beam, not relevant at E0 since there is not focusing system at that point.
- σ_H and σ_V are the horizontal and vertical sizes of the beam at the interaction point.

The uncertainty in the luminosity by using equation B.1 is about $\approx$ 15 % due to uncertainties in the determination by the accelerator staff of the various quantities in equation B.1.

REFERENCES

[1] N. Amos et al. Phys. Rev. Lett. 63 (1989) 2784.

[2] N. Amos et al. "A Luminosity-independent measurement of the $P\overline{P}$ total cross section at $sqrts$=1.8 TeV" Phys. Lett. B 243 (1990) 158.

[3] N. Amos et al. Phys. Lett. B 301 (1993) 313.

[4] F. Abe et al. Phys. Rev. D 50 (1994) 5535.

[5] F. Abe et al. Phys. Rev. D 41 (1990) 2330.

[6] K Goulianos. Nuclear Physics B (proc. Suppl.) 12 (1990) 110.

[7] K. Goulianos. Phys. Reports 101 (1983) 169.

[8] C. Augier et al. Phys. Lett. B 316 (1993) 448.

[9] F. Abe et al. Phys. Rev. D 50 (1994) 5519

[10] N. Amos et al. Phys. Lett. B 247 (1990) 127.

[11] U. Amaldi et al. Phys. Lett. B 36 (1971) 504.

[12] U. Amaldi et al. Phys. Lett. B 66 (1977) 390.

[13] F. Abe et al. Phys. Rev. D 50 (1994) 5550

[14] N. Amos et al. "Measurement of ρ, the ratio of the real to the Imaginary part pf the $P\overline{P}$ Forward Elastic-Scattering Amplitude, at $\sqrt{s}$=1.8 TeV" Phys. Rev. Lett. 68 (1992) 2433.

[15] C. Augier et al. Phys. Lett. B 344 (1995) 451.

[16] M. Bozzo et al. Phys. Lett. B 147 (1984) 385.

[17] M. Bozzo et al. Phys. Lett. B 147 (1984) 392.

[18] D. S. Ayres et al. Phys. Rev. D 15 (1977) 3105.

[19] M. Ambrosio et al. Phys. Lett. B 115 (1982) 495.

[20] N. Amos et al. Phys. Lett. B 128 (1983) 343.

[21] N. Amos et al. Nucl. Phys. B 262 (1985) 689.

[22] W. Galbraith et al. Phys. Rev. B 138 (1965) 913.

[23] S. P. Denisov et al. Phys. Lett. B 36 (1971) 528.

[24] A. S. Carroll et al. Phys. Lett. B 61 (1976) 303.

[25] A. S. Carroll et al. Phys. Lett. B 80 (1979) 423.

[26] G. J. Alner et al. Z. Phys. C 32 (1986) 153.

[27] G. B. West and D. R. Yennie. Phys. Rev. 172 (1968) 1413.

[28] R. Cahn. Z. Phys. C 15 (1982) 253.

[29] S. M. Roy Phys. Rep. 5 (1972) 125.

[30] G. Giacomelli Phys. Rep. 23 (1976) 123.

[31] M. Froissart Phys. Rev. D 123 (1961) 1053.

[32] I. Y. Pomeranchuk. Sov. Phys. JETP 7 (1958) 499.

[33] R. J. Eden. Phys. Rev. Lett. 16 (1966) 39

[34] H. Cornille and A. Martin. Phys. Lett. 40 B (1972) 671

[35] M. Block and R. Cahn Rev. Mod. Phys. 57 (1985) 563

[36] G. Alberi and G. Goggi. Phys. Rep. 74 (1981) 1

[37] J. Fisher Phys. Rep. 76 (1981) 157

[38] M. Kamram Phys. Rep. 108 (1984) 275

[39] J. Fisher et al. Phys. Rev. D 18 (1978) 4271.

[40] B. Baumbaugh et al. Nucl. Instr. Meth. A 345 (1994) 271

[41] M. Bocciolini et al. Nucl. Instr. Meth. A 240 (1985) 36.

[42] G. S. Damerell. Nucl. Instr. Meth. A 342 (1994) 78.

[43] D. Sigg. Nucl. Instr. Meth. A 345 (1994) 107.

[44] T. Roy, S. J. Watts and D. Wright. Nucl. Instr. Meth. A 275 (1989) 545.

[45] I. Yoshii. Nucl. Instr. Meth. A 342 (1994) 156.

[46] M. R. Mondardini. Nucl. Phys. B 25 (1992) 294.

[47] C. Avila et al. Nucl. Instr. Meth. A 360 (1995) 80.

[48] A. Baumbaugh et al. preprint Fermilab FN 439, 1986.

[49] J. Thompson preprint Fermilab TM 1909, 1994.

[50] V. Bharadwaj et al. preprint Fermilab TM 1970, 1995.

[51] G. Giacomelli. "Hadron-Hadron Elastic Scattering and Total cross sections at High Energies" preprint DFUB-9-94.

[52] Dimitrios Dimitroyannis. *Measurement of the proton-antiproton total cross section at the Tevatron* Thesis, University of Maryland, 1990.

[53] Cedric Guss. *Measurement of σ_{tot} and B from $P\overline{P}$ Elastic Scattering at the Fermilab Tevatron* Thesis, Northwestern University, 1989.

[54] Sasan Sadr. *E710, $P\overline{P}$ Elastic Scattering at Tevatron Energies* Thesis, Northwestern University, 1993.

[55] Shekhar Shukla. *Determination of Leff at D47 and E14* E710 Internal Report, Nov 6 1989.

[56] Charles Cameron Allen. *Multiplicity and pseudorapidity distributions from proton-antiproton collisions at $\sqrt{s}$=1.8 TeV* Thesis, Purdue University, 1991.

[57] Noel M. Morris. *Semiconductor devices* Macmillan press ltd. 1976 London.

[58] Kuraray co. Ltd. Methacrylic resin division shiwa higashi - yaesu building 9-1 hatchobori 2 - chrome chuo-ku tokyo 104, Japan